

VERITAS OBSERVATIONS OF GALACTIC GAMMA-RAY SOURCES

by

Kazuma Tsurusaki

An Abstract

Of a thesis submitted in partial fulfillment of the
requirements for the Doctor of Philosophy
degree in Physics in the
Graduate College of The
University of Iowa

July 2012

Thesis Supervisor: Professor Philip Kaaret

ABSTRACT

The main topic of this thesis is analysis of an unidentified Galactic TeV gamma-ray source, MGRO J1908+06, discovered by Milagro instrument in 2007. We analyzed 54 hours of observational data from the Very Energetic Radiation Imaging Telescope Array System (VERITAS), a ground-based gamma-ray observatory in southern Arizona comprised of an array of four Cherenkov Telescopes that reconstructs the energy and direction of astrophysical gamma-rays by imaging Cherenkov light emitted by energetic particles in air showers produced by the primary gamma-rays. MGRO J1908+06 is located between a supernova remnant SNR G40.5-0.5 and a young, energetic pulsar PSR J1907+0602. We studied the energy dependent morphology of the TeV emission from the source and measured the source extent and spectrum. The source extends well past the boundary of the SNR which likely excludes an origin for the emission as solely due to the SNR. While emission in the 0.5-1.25 TeV band was centered around the pulsar, higher energy emission was observed near the supernova remnant. This morphology is opposite that observed in other pulsar wind nebula. We proposed two models for the high energy emission located well away from the pulsar: (1) shock acceleration at the shock front created by an interaction between the pulsar wind and the dense gas at the edge of the SNR or (2) motion of the pulsar combined with the pulsar spin-down resulting in a relic population of high energy particles near the SNR. These models can be tested by looking for molecular emission lines that trace shocks and by measuring the pulsar velocity.

In addition, we investigated the gamma-ray emission from the nova explosion of V407 Cygni that occurred in March 2010. The Fermi-LAT observed this event in the energy range of $E > 100$ MeV. The origins of the gamma-ray emission that the

Fermi-LAT team proposed are either protons (hadronic model) or electrons (leptonic model), both of which were accelerated at the nova shock via the Fermi acceleration mechanism. We did not consider their leptonic model because no TeV gamma-ray emission is predicted. Their hadronic model can generate TeV gamma-rays with the modeled parameters. We found no evidence for TeV emission. We showed that with the flux upper limit calculated using the VERITAS data imposes constraints on the extension of the proton spectrum at high energies.

Abstract Approved: _____
Thesis Supervisor

Title and Department

Date

VERITAS OBSERVATIONS OF GALACTIC GAMMA-RAY SOURCES

by

Kazuma Tsurusaki

A thesis submitted in partial fulfillment of the
requirements for the Doctor of Philosophy
degree in Physics in the
Graduate College of The
University of Iowa

July 2012

Thesis Supervisor: Professor Philip Kaaret

Copyright by
KAZUMA TSURUSAKI
2012
All Rights Reserved

Graduate College
The University of Iowa
Iowa City, Iowa

CERTIFICATE OF APPROVAL

PH.D. THESIS

This is to certify that the Ph.D. thesis of

Kazuma Tsurusaki

has been approved by the Examining Committee
for the thesis requirement for the Doctor of
Philosophy degree in Physics at the July 2012
graduation.

Thesis Committee: _____
Philip Kaaret, Thesis Supervisor

Robert Mutel

Kenneth Gayley

Randall McEntaffer

Amanda Weinstein

To my parents

ACKNOWLEDGMENTS

First and foremost, I would like to express my deepest gratitude to my academic advisor, Philip Kaaret, who gave me an opportunity to join VERITAS and guided me patiently through my entire research path in the University of Iowa.

I would also like to express my very sincere gratitude to Daniel Gall. Without him, I would not have acquired analytical skills of VEGAS and made advances in the research. And not just in the research field, he gave so many concerns and kindnesses to me.

I also would like to thank the members of VERITAS in other institutions, such as Brian Humensky, who gave me very useful advices when I was stuck at the VEGAS analysis. Without these people's help, I would not have stepped further.

In addition, I would like to thank those who proofread my English draft, Ryan Allured, Thomas Brantseg, Casey DeRoo and Scott Griffiths.

Lastly, I would like to express my special thanks to my family in Japan for their never ending encouragement and support.

ABSTRACT

The main topic of this thesis is analysis of an unidentified Galactic TeV gamma-ray source, MGRO J1908+06, discovered by Milagro instrument in 2007. We analyzed 54 hours of observational data from the Very Energetic Radiation Imaging Telescope Array System (VERITAS), a ground-based gamma-ray observatory in southern Arizona comprised of an array of four Cherenkov Telescopes that reconstructs the energy and direction of astrophysical gamma-rays by imaging Cherenkov light emitted by energetic particles in air showers produced by the primary gamma-rays. MGRO J1908+06 is located between a supernova remnant SNR G40.5-0.5 and a young, energetic pulsar PSR J1907+0602. We studied the energy dependent morphology of the TeV emission from the source and measured the source extent and spectrum. The source extends well past the boundary of the SNR which likely excludes an origin for the emission as solely due to the SNR. While emission in the 0.5-1.25 TeV band was centered around the pulsar, higher energy emission was observed near the supernova remnant. This morphology is opposite that observed in other pulsar wind nebula. We proposed two models for the high energy emission located well away from the pulsar: (1) shock acceleration at the shock front created by an interaction between the pulsar wind and the dense gas at the edge of the SNR or (2) motion of the pulsar combined with the pulsar spin-down resulting in a relic population of high energy particles near the SNR. These models can be tested by looking for molecular emission lines that trace shocks and by measuring the pulsar velocity.

In addition, we investigated the gamma-ray emission from the nova explosion of V407 Cygni that occurred in March 2010. The Fermi-LAT observed this event in the energy range of $E > 100$ MeV. The origins of the gamma-ray emission that the

Fermi-LAT team proposed are either protons (hadronic model) or electrons (leptonic model), both of which were accelerated at the nova shock via the Fermi acceleration mechanism. We did not consider their leptonic model because no TeV gamma-ray emission is predicted. Their hadronic model can generate TeV gamma-rays with the modeled parameters. We found no evidence for TeV emission. We showed that with the flux upper limit calculated using the VERITAS data imposes constraints on the extension of the proton spectrum at high energies.

TABLE OF CONTENTS

LIST OF TABLES	vii
LIST OF FIGURES	ix
CHAPTER	
1 INTRODUCTION	1
1.1 Gamma-Ray Astronomy	1
1.2 Plan of this thesis	2
2 INSTRUMENT FOR THE RESEARCH: VERITAS	3
2.1 Air Showers	3
2.2 Event Reconstruction	6
2.3 Overview of VERITAS Hardware	7
2.4 The Positioner and Optical Support Structure of VERITAS Telescopes	8
2.5 Camera in the VERITAS Telescope	9
2.6 Trigger	10
2.7 FADC	12
3 DATA ANALYSIS	13
3.1 Stage1: Calibration Calculation	13
3.1.1 Pedestal Removal	13
3.1.2 FADC Timing Calibration	14
3.1.3 Relative Gain Calculation	14
3.1.4 Pixel Status Assessment	15
3.2 Stage2: Application of Calibration and Data Parametrization	15
3.2.1 Image Cleaning	15
3.2.2 Image Parameterization	16
3.3 Stage4.2: Event Quality Selection	17
3.3.1 Quality Selection	17
3.3.2 Shower Direction Reconstruction	18
3.3.3 Shower Core Reconstruction	20
3.3.4 Gamma-Ray and Cosmic-Ray Discrimination	22
3.3.5 Energy Reconstruction	22
3.4 Stage5: Shower Level Cuts	23
3.5 Stage6: Results Extraction	23
3.6 Ring Background Model	24
3.7 Reflected Region (Wobble) Model	25
3.8 Spectrum Reconstruction	26

4	FERMI ACCELERATION MECHANISM	30
4.1	Shock Waves	30
4.2	Fermi Acceleration of the First Order	35
5	V407 CYGNI	42
5.1	Fermi-LAT and V407 Cygni	43
5.2	Two Physical Models for Gamma-Ray Creation	45
5.3	VERITAS Analysis on V407 Cygni	47
5.4	Results	48
5.5	Discussion	48
5.6	Physical profile of the nova	53
5.6.1	Time Evolution of the Nova	53
5.6.2	Magnetic Fields in the Binary	59
5.6.3	Particle Acceleration	62
6	MGRO J1908+06	66
6.1	Observational history and features	66
6.2	Supernova Remnants, Pulsars, and Pulsar Wind Nebulae	68
6.2.1	Supernovae and Supernova Remnants	68
6.2.2	Pulsars	69
6.2.3	Pulsar Wind Nebula	70
6.3	Objects near the source	77
6.4	SNR G40.5-0.5	78
6.5	PSR J1907+0602	83
6.6	VERITAS analysis on the target	87
6.6.1	Data used for the analysis	87
6.6.2	Significance and Excess calculation	88
6.6.3	Energy Spectra of J1908 and Pulsar	98
6.7	Energy dependent analysis	104
6.7.1	2D-Gaussian fitting of the two maps	107
6.8	Discussion	111
6.8.1	Energy dependent morphology	111
6.8.2	Shock acceleration by SNR G40.5-0.5	113
6.8.3	Pulsar wind nebula	113
6.9	Conclusion	119
7	CONCLUSION	120
	REFERENCE	123

LIST OF TABLES

3.1	Examples of the Hillas parameters	17
5.2	Analysis results. The disp method gives higher significance for both the Crab and J2102+4542 (V407 Cygni). Also, the flux upper limit is tighter using the disp method.	49
5.3	Parameter set Orlando & Drake (2011) used for the simulations. . .	57
6.4	Parameters of the shocked gas, taken from Yang et al. (2006). The information of the position angle was directly given by the author. .	81
6.5	Parameters of PSR J1907+0602, taken from Abdo et al. (2010b). .	84
6.6	VERITAS observations used for our analysis of MGRO J1908+06. .	87
6.7	Zenith angle distribution of the observing runs used for this analysis.	88
6.8	Examples of cuts on the Hillas parameters, optimized for different types of the source. See Sec. 3.2.2 for the Hillas parameters, and see Sec. 3.3.4 for the Mean Scaled Parameters (MSPs). We chose “Hard” for the analysis of MGRO J1908+06.	89
6.9	The results of the 2D-Gaussian fittings of the excess map of analysis 1. The fitting regions are the squares with different sizes centered on the Milagro source position.	91
6.10	The RBM analysis results for analysis 1 on MGRO J1908+063. The source position is set on the Milagro source position, and radius of the search window is set to $= 0.5^\circ$ as HESS to compare their Excess map with ours.	92
6.11	The RBM analysis results for analysis 2 on MGRO J1908+063. The source position is set on the Milagro source position, and radius of the search window is set to $= 0.5^\circ$ following HESS in order to be able to compare their Excess map with ours.	95
6.12	Results of 2D-Gaussian fitting of the excess map of analysis 2. . . .	95
6.13	Effective area lookup tables we used for the different epochs of observational data.	99

6.14	The files used for the Significance and the Excess analysis sorted by the seasons and the type of the telescope array. Some of these were removed from the run lists for the spectral analyses in stage 6, because they did not have proper background regions in the field of view for the wobble model.	100
6.15	The numbers of the different files of the different types, used for the spectral analysis of MGRO J1908+06. All of these had background region inside the field of view for the wobble model. Energy Threshold is the energy of lowest energy bin where we have counts. The threshold of the combined spectrum for this analysis is the lowest one of these values, 0.473 TeV.	100
6.16	The numbers of the different files of the different types, used for the spectral analysis of PSR J1907+0602. All of these had background region inside the field of view for the wobble model. Energy Threshold is the energy of lowest energy bin where we have counts. The threshold of the combined spectrum for this analysis is the lowest one of these values, 0.473 TeV.	101
6.17	The maximum Significance in the energy dependent Significance maps taken with 0.2° integral window radius. The Max. Significance is above 5σ at all of these maps.	104
6.18	The results of the 2D-Gaussian fittings the excess map of 0.2° window radius for the full energy range. The fitting regions are the squares with different sizes centered on the source position we had at analysis 2.	108
6.19	The results of the 2D-Gaussian fittings the excess map of 0.2° window radius for 0.5-1.25 TeV. The fitting regions are the squares with different sizes centered on the source position we had at analysis 2.	109

LIST OF FIGURES

2.1	Overview of the VERITAS telescope array system. Credit: The VERITAS collaboration	3
2.2	Schematic image of an air shower. Taken from Celik (2008).	4
2.3	When a charged particle moves faster than the local speed of light (Left), the envelope of the radiation adds up to Cherenkov radiation (Right). Credit: C. N. Booth/The University of Sheffield	5
2.4	The cone of Cherenkov radiation generated by the air shower, making a light pool of radius \sim 130 m on the ground. Credit: The H.E.S.S. Collaboration	6
2.5	The air shower looks different at the different telescopes, but its source position should be the same place on the camera plane. Credit: The CANGAROO Collaboration.	7
2.6	Lateral views of a 100GeV photon initiated air-shower (Left) and a 100 GeV cosmic ray initiated air-shower (Right) (Monte Carlo simulation). Taken from Cogan (2006).	8
2.7	Backside of a VERITAS telescope while under construction. The frame is the OSS. Credit: The VERITAS Collaboration.	9
2.8	A VERITAS telescope. The red circle shows the box in which the camera is installed. Credit: Martin Schroedter/The VERITAS Collaboration.	10
2.9	Schematic structure of one PMT. Credit: Hamamatsu Corporation	10
2.10	(Left) Frontal image of the camera without the light cones. (Right) Frontal image of the camera when the light cones are attached. Both taken from Cogan (2006).	11
3.11	An image of a gammay-ray induced shower on a camera before (Left) and after (Right) the cleaning. Taken from Cogan (2006).	16
3.12	Image of a shower ellipse and the Hillas parameters. Taken from Gall (2010).	17
3.13	Shower direction reconstruction using the standard method. Taken from Cogan (2006).	18

3.14	Direction reconstruction using the disp method. Each image has two direction candidates (Left); the one which is closer to the candidates from the other images is likely to be the correct one (Right). Taken from Morang (2008).	20
3.15	A histogram which shows the <i>Width/Length vs. Displacement</i> (noted as “Separation” in this image) relation for different image sizes, used for the disp method. Taken from Morang (2008).	21
3.16	Shower core reconstruction. Taken from Cogan (2006).	21
3.17	An example of energy lookup table. The horizontal axis is the logarithms of <i>Size</i> and the vertical axis is the impact distance. The color scale is the estimated $\log(\text{Energy}(\text{GeV}))$. Taken from Celik (2008).	23
3.18	The locations of the ON region and the OFF region for the reflected background region model (Left), and for the Ring Background model (Right). Taken from Celik (2008).	25
3.19	Example of a spectrum reconstructed by VEGAS, which obeys the power law derived earlier.	28
3.20	The counts (ON&OFF) per logarithmic energy bin for the Crab. Created by VEGAS with the disp method.	29
4.21	(Left) A shock wave propagating in a stationary medium with velocity U . (Right) A shock wave seen in the frame where the shock front is stationary.	31
4.22	(Left) The shock propagating in a stationary interstellar medium with the velocity U . (Right) The shock in a frame where the shock front is stationary.	37
4.23	(Left) The shock in a frame where the downstream gas is stationary. (Right) The shock in a frame where the upstream gas is stationary.	37
5.24	An image of Nova of V407 Cygni taken at 19:08 UT on March 10 (Right), and an image taken on March 7 (Left). Credit: K. Nishiyama and F. Kabashima/H. Maehara, Kyoto Univ.	42
5.25	Fermi-LAT’s gamma-ray images of V407 Cygni before (Left) and after (Right) the nova. Credit: NASA/DOE/Fermi LAT Collaboration.	43

5.26	The light curves of V407 Cygni, taken from Abdo et al. (2010a). The top column is the gamma-ray taken from the Fermi-LAT. The middle column is the optical, and the bottom is X-ray from Swift. Vertical bars are 1σ statistical error. For the gamma-ray, the gray arrows indicate 2σ upper limits. The blue horizontal arrow indicates the VERITAS observational period of Crab nebula (March 12-16), and the red horizontal arrow indicates the VERITAS observational period of the V407 Cygni (March 19-26) (see Sec. 5.3).	44
5.27	SED of V407 Cygni taken from Abdo et al. (2010a). Vertical bars indicate 1σ statistical error, arrows indicate 2σ upper limits, and horizontal bars shows energy ranges. The black solid line is the spectrum modeled with the hadronic model, the blue dashed line is the one modeled with the leptonic model.	46
5.28	Significance maps of FGL J2102+4542 reconstructed by the two methods: (Left) standard method, (Right) disp method. The white circle at the center indicates the source position and the size of the source region used for the analysis.	50
5.29	Significance maps of the Crab Nebula reconstructed by the two methods: (Left) standard method, (Right) disp method. The white circle at the center indicates the putative Crab nebula position and the size of the source region used for the analysis.	50
5.30	Modeled spectrum of V407 Cygni (FGL J2102+4542), modification of the spectral plot of Abdo et al. (2010a). The black dots with error bars are the Fermi-LAT's data points. Vertical bars indicate 1σ statistical error, and arrows indicate 2σ upper limit. The two rightmost arrows show the VERITAS flux upper limits calculated using the displacement method (lower left) and the standard method (upper right) for event reconstruction. The fitting curve was constructed with the method of Kamae, Karlsson, Mizuno, Abe, & Koi (2006) with the parameters $(s_p, \log(E_{cp}))=(2.15, 1.5)$. See Sec. 5.2.	51
5.31	The confidence region map including the upper limit constraints from both Fermi-LAT and VERITAS (solid lines), and the one constraint from Fermi-LAT only for a 99% confidence level (broken line, taken from the Supporting Online Material of Abdo et al. (2010a)). The x-axis is the spectral slope (s_p), and the y-axis is the logarithm of the cutoff energy (E_{cp} in GeV). The maximum value of y-axis was extended from 4 to 6.5. The percentile values correspond to the confidence levels of the fit of the Fermi-LAT data (see Sec. 5.4.) The contour data from the Fermi results was provided by Pierre Jean of the Fermi-LAT collaboration.	52
5.32	Artist's image of the nova of RS Ophiuchi in 1985. Credit: David Hardy/PPARC	54

5.33	Temporal profile of the $H\alpha$ spectra of V407 Cygni that the ANS collaboration obtained. The upper three plots in the left column are those in the quiescent phase (in the year 1999, 2008 and 2009), and the rest shows the profile after the nova explosion (20100313= $+2.3d$ and thereafter). Taken from Munari et al. (2010).	55
5.34	Velocity profile of the nova shell. For the period between $+0d$ and $+2.3d$, the solid line is the “free expansion model,” and the broken line is the “extrapolation model.”	58
5.35	Position of the nova shell on the line between the WD center and the RG center by time. The solid line is the “free expansion model,” and the broken line is the “extrapolation model.” The lower red line corresponds to the front face of the RG (15.5 AU from the WD surface), and the upper red line is the rear end of the RG (19.9 AU from the WD surface). The blue horizontal line indicates the period in which VERITAS observed V407 Cygni (Mar. 19-26: $+9d \sim +16d$).	59
5.36	The time evolution of the magnetic field strength (in G) at the shock front in time. The solid line is the “free expansion model,” and the broken line is the “extrapolation model.” The upper limit of the vertical axis corresponds to the magnetic field strength at the front face of the RG; the shock reaches the RG at the time when the curve touches the upper edge for both models.	61
5.37	The profile of the maximum energy a particle can obtain in the nova shell. The solid line is the “free expansion model,” and the broken line is the “extrapolation model.” The blue line indicates the period of the VERITAS observation of V407 Cygni. For the “free expansion model,” the nova reaches the RG at $\sim +21d$. For the “extrapolation model,” the nova reaches the RG at $\sim +16d$	63
5.38	The photon energy spectra for the best fitting proton spectra parameters, with the protons’ cutoff energies set at the maximum obtainable energies for the two velocity models: the solid line is the case for the “extrapolation model,” ($s_p, \log(E_{cp}) \sim (2.7, 3.5)$), and the dotted line is the case for the “free expansion model,” ($s_p, \log(E_{cp}) \sim (2.7, 3.2)$).	64
6.39	The Significance map taken from the Milagro paper (Abdo et al., 2007). Boxes and crosses are the locations of the GeV sources in the third EGRET catalog (3EG). J1908+06 is located at the Galactic Longitude of $\sim 40^\circ$ with a significance of 8.3σ	67

6.40	The Excess map taken from the HESS paper (Aharonian et al., 2009). The three colored contours correspond to the pre-trial significance level 9σ , 10σ and 11σ . The source extent found with Milagro is shown by the dotted white lines; 8σ contour (inner) and 5σ contour (outer). The crosses are the best HESS and Milagro fitted positions, of which the error bars are the summation of the statistical and systematic errors.	67
6.41	Hubble telescope image of the Crab nebula, known as the most representative supernova remnants. The supernova explosion at this was observed in 1054 AD by Japanese and Chinese observers. Credit: NASA, ESA and Allison Loll/Jeff Hester	71
6.42	The current modeled spectrum of the Crab Nebula Taken from Tanaka & Takahara (2010). The total spectrum (Total) is the summation of the synchrotron radiation (SYN), Inverse Compton/Cosmic Background (CMB) and synchrotron self-Compton (SSC). The error points are the observed data, and those data match the simulated model (Total) very well.	72
6.43	The spectral evolution of the Crab Nebula Tanaka & Takahara (2010) simulated. The thick solid line (the spectrum of the Crab at 1kyr old) is the current one. Taken from Tanaka & Takahara (2010).	73
6.44	The relation between $\log(L_\gamma/L_X)$ and $\log(\text{Age})$ [yrs] of PWNe. A positive correlation between the two parameters can be observed. The data are from Kargaltsev & Pavlov (2010).	75
6.45	The relation between spectrum index and $\log(\text{Age})$ [yrs] of PWNe. The data are from Kargaltsev & Pavlov (2010).	76
6.46	Very Large Array Galactic Plane Survey (VGPS) (Stil et al., 2006) map of the continuum radio emission near 1420 MHz, but excluding the H I line around the J1908+063 region. The small light blue line is the Milagro significance contour of the significance level $\sigma = 8$, and the large white line that encloses the entire region is the Milagro significance contour of $\sigma = 5$. The dashed ellipse shows SNR G40.5-0.5, following Yang et al. (2006). Its center is positioned at (RA, Dec)=(19:07:08.6, +06:29:53.0) (Abdo et al., 2010b), its size is $28' \times 24'$ (=25 pc) (Yang et al., 2006), and the angle of major axis in galactic coordinates is 31° . The light blue arrow inside a circle on the lower left corner indicates North for RA/Dec.	77

6.47	The 1720 MHz contour map of SNR G40.5-0.5, the contour interval of which is 120 mJy/beam (Left), and the 2700 MHz contour map of SNR G40.5-0.5, the contour interval of which is 40 mJy/beam (Right). Both are taken from Downes et al. (1980). The contours with anticlockwise arrows are around the peaks, and those with clockwise arrows are around the minima. The broken lines indicate the local zero level for SNR G40.5-0.5. The vectors represent the direction and the intensity of the linearly polarized component of the electric vectors.	79
6.48	The spectrum of G40.5-0.5, fitted for the flux density data of Downes et al. (1980) and Pauliny-Toth & Kellermann (1966). Taken from Downes et al. (1980).	80
6.49	CO intensity map of the G40.5-0.5 region taken from Yang et al. (2006). The contours correspond to the intensity levels of the velocity component, $V_{LSR} = 45-65 \text{ km s}^{-1}$. This is the same ellipse plotted in Fig. 6.46. The ellipse is the shocked shell of the SNR ($28' \times 24'$), and the cross is its center.	81
6.50	HI map of the Galactic plane around G40.5-0.5 in the velocity interval 45-65 km/s from the VGPS (Stil et al., 2006). Some structures can be seen along the rim of G40.5-0.5 area.	82
6.51	The folded light curves of PSR J1907+0602 taken from Abdo et al. (2010b). The top five are those made with the LAT data for different energy band, and the rest (bottom one) is the light curve of the Arecibo (radio) data.	85
6.52	The Fermi-LAT counts map around PSR J1907+0602 taken from Abdo et al. (2010b). Left is the image at the “on” phase of PSR, and right is that at the “off” phase.	86
6.53	The RBM Excess map of MGRO J1908+06 of the search window radius of 0.5° , given as the result of analysis 1 (Sec. 6.6.2.1). The large black cross mark shows the Milagro source position and its error (simple summation of the statistical error and the systematic error.). The blue smaller cross is the HESS source position with the statistical error. The red cross is the centroid of the best fitting 2D-Gaussian function for the VERITAS Excess map given with the window size of $3.0^\circ \times 3.0^\circ$ (See Table 6.9). The white ellipse is SNR G40.5-0.5, and the green X is PSR J1907+0602. The contours near the center are the Milagro Significance contours of 8σ (inner, light-blue) and 5σ (outer, white). The black circle notes the region to be used as the “exclusion region” in analysis 2. It is centered on the best fitting 2D-Gaussian centroid (red cross) and has a radius of 0.7°	93

6.54	The RBM Excess map of MGRO J1908+06 using a search window radius of 0.5° , given as the result of analysis 2 (Sec. 6.6.2.2). The large black cross mark shows the Milagro source position and its error (simple summation of the statistical error and the systematic error.). The blue smaller cross is the HESS source position with the statistical error. The tiny red square behind the HESS cross (blue) is the centroid of the best fitting 2D-Gaussian function for this Excess map given at this analysis with the fitting window size of $3.0^\circ \times 3.0^\circ$ (See Table 6.12). The white ellipse is SNR G40.5-0.5, and the green X is PSR J1907+0602. The contours near the center are the Milagro Significance contours of 8σ (inner, light-blue) and 5σ (outer, white). The black circle is the source exclusion region.	96
6.55	The RBM Significance map of MGRO J1908+06 corresponding to Fig. 6.54.	97
6.56	The spectrum of the “Region A,” the region around MGRO J1908+06 with 0.5° radius centered on the 2D-Gaussian centroid obtained at analysis 2 (RA= 286.97° and Dec= 6.20° ; See Sec. 6.6.2.2).	102
6.57	The spectrum of the “Region B,” region centered on PSR J1907+0602 (RA= 286.97° and Dec= 6.04°) with the window radius of 0.4° . . .	102
6.58	MGRO J1908+06 spectra from HESS (blue) and VERITAS (black). Our spectrum of J1908 is (Norm, Index)= $((4.4 \pm 0.6) \times 10^{-8} \text{ TeV}^{-1} \text{ m}^{-2} \text{ s}^{-1}, -1.79 \pm 0.11)$, and the HESS spectrum is (Norm, Index)= $((4.1 \pm 0.32_{stat} \pm 0.83_{sys}) \times 10^{-8} \text{ TeV}^{-1} \text{ m}^{-2} \text{ s}^{-1}, -2.1 \pm 0.07_{stat} \pm 0.2_{sys})$, so the two fitting lines match in the error range, and the Milagro data point (red: $(8.8 \pm 2.4) \times 10^{-11} \text{ TeV}^{-1} \text{ m}^{-2} \text{ s}^{-1}$) at 20 TeV is covered in the VERITAS error range $((1.86 \pm 0.87) \times 10^{-10} \text{ TeV}^{-1} \text{ m}^{-2} \text{ s}^{-1})$ at that energy.	103
6.59	Excess (Left) and Significance (Right) maps of MGRO J1908+06 for the energy range of 0.5-1.25 TeV (first row), 1.25-3 TeV (second row) and > 3 TeV (third row). The search window size is 0.2° . The blue X mark specifies our source position we had at analysis 2, the green cross is the position of PSR J1907+0602, and the ellipsis of the light blue line is SNR G40.5-0.5, respectively in each maps. The scale of Excess maps is -70 to 165, in common with Fig 6.60, and the scale of Significance maps is -4 to 9, also in common with Fig 6.60.	105

6.60	Excess (Left) and Significance (Right) maps of MGRO J1908+06 for the energy range of > 1.25 TeV (combination of 1.25-3 TeV and > 3 TeV: upper row) and the full energy range (lower row). The search window size is 0.2° . The blue X mark specifies our source position we had at analysis 2, the green cross is the position of PSR J1907+0602, and the ellipsis of the light blue line is SNR G40.5-0.5, respectively in each maps. The scale of Excess maps is -70 to 165, in common with Fig 6.59, and the scale of Significance maps is -4 to 9, also in common with Fig 6.59.	106
6.61	(Left) Excess map of MGRO J1908+06 for the full energy range. The blue X mark specifies our source position given at analysis 2, and the green cross is the position of PSR J1907+0602. The light blue circle is centered on the centroid of the best fitting 2D-Gaussian for this map, and its radius is equivalent to the σ value, 0.43° (the size of the fitting region is $3.0^\circ \times 3.0^\circ$). (Right) Excess map of MGRO J1908+06 for the energy range of 0-1.25 TeV. The blue X mark specifies our source position given at analysis 2, and the green cross is the position of PSR J1907+0602. The light blue circle is centered on the centroid of the best fitting 2D-Gaussian for this map, and its radius is equivalent to the σ value, 0.40° (the size of the fitting region is $3.0^\circ \times 3.0^\circ$). . .	110
6.62	Three color VERITAS Excess map for the energy ranges of 0.5-1.25TeV (red), 1.25-3TeV (green), and > 3 TeV (blue). The search window radius is 0.2° . The red cross near the center is the J1908 source position we found in analysis 2, and the green cross is the PSR.	112
6.63	The relation between the sizes and the ages of some 40 TeV PWNe, using the data of Kargaltsev & Pavlov (2010). There is some correlation between these two parameters. The dotted line is the age of PSR J1907+0602 (Log age is 4.28). The red error bar specifies the size (σ) of the 2D-Gaussian functions fitted to the full energy map allowing for the systematic errors discussed in the text. The blue error bar is that for 0.5-1.25 TeV map.	115
6.64	The energy spectra of the PWN HESS J1825-137 for different regions. The wedges in the upper left image are the radial regions with different distances in steps of 0.1° from the pulsar PSR J1826-1334. The broken lines are parallel (equal power law index) with the uppermost spectrum, that of the innermost (closest to the PSR) region. The softening of the spectrum occurs for regions more distant from the PSR. Taken from Aharonian et al. (2006a).	116

CHAPTER 1 INTRODUCTION

1.1 Gamma-Ray Astronomy

Gamma-rays are the last unexplored electromagnetic window of our universe. It is one of the most exciting regions of astronomical research today and helps to reveal the innermost appearance of the universe. Not only is it interesting in its own astronomical context, but it also is useful for investigating the unsolved problems of physics, especially in the high energy region. Physical processes that cannot be reproduced in the laboratory on Earth can occur in some exotic objects of the universe, and thanks to space-based detectors and ground-based gamma-ray detectors, we can observe them.

The energy flux of gamma-rays from astronomical objects generally obeys a power law with a negative index ($\sim 2 - 2.5$). Space-based detectors with small collection areas ($\sim 500 \text{ cm}^2$) are ineffective in the TeV energy range due to the rapidly falling flux of gamma-ray photons from cosmic sources in this energy regime, i.e., there aren't enough counts. The Imaging Atmospheric Cherenkov Technique (IACT) is a method whereby very high energy gamma-ray photons can be detected indirectly by ground based telescopes. It works by imaging the Cherenkov radiation generated by the cascade of relativistic charged particles produced when a very high energy gamma-ray strikes the atmosphere. The purpose of my research is to study the very high energy gamma-rays emitted from a few selected astronomical objects, mainly using data taken with the Very Energetic Radiation Imaging Telescope Array System (VERITAS). VERITAS is one of the four major ground-based gamma-ray observatories, and is located at the Fred Lawrence Whipple observatory in southern Arizona. It consists of an array of four 12m optical reflectors and is sensitive over an energy range of 100 GeV-50 TeV.

1.2 Plan of this thesis

In Chapter 2 of this document, the VERITAS instrument which is the hardware associated with my research is described. Chapter 3 is concerned with VEGAS, the analysis suite of VERITAS. The techniques used to analyze VERITAS data with VEGAS are described here. Chapter 4 is devoted to a theoretical treatment of the mechanism of a shock wave, as well as the derivation of the Fermi Acceleration of the first order. In Chapter 5, one of our analytical targets, V407 Cygni, is discussed, and our current work on it is presented. In Chapter 6, we discuss our analysis on MGRO J1908+06. In Chapter 7, we summarize all the works done for this thesis.

CHAPTER 2

INSTRUMENT FOR THE RESEARCH: VERITAS

VERITAS is a major ground-based gamma-ray observatory located at the Fred Lawrence Whipple Observatory in southern Arizona. It is an array of four 12m optical reflectors for gamma-ray astronomy in the very high energy (100 GeV-50 TeV) range. It is one of the four IACT (Imaging Atmospheric Cherenkov Technique) telescope arrays currently working in the world. In Sec. 2.1 through Sec. 2.2, a general description about the IACT and its event reconstruction scheme will be given. In Sec. 2.3 through Sec. 2.6, the VERITAS hardware and data acquisition system will be explained.



Figure 2.1: Overview of the VERITAS telescope array system. Credit: The VERITAS collaboration

2.1 Air Showers

IACTs work by imaging the Cherenkov radiation generated by the cascade of relativistic charged particles produced when a very high energy gamma-ray strikes the atmosphere. The atmosphere is opaque to high energy photons, and gamma-rays do not reach the ground; the incoming gamma-ray photon undergoes pair

production in the atmosphere. The produced electron-positron pairs are of extremely high energy and immediately undergo Bremsstrahlung. This radiation is itself extremely energetic, and many of these secondary photons produce additional electron-positron pairs. This cascade of particles is called an “air shower,” initiated at 10 – 20 km above the ground (Fig. 2.2). Many of the particles in the air shower

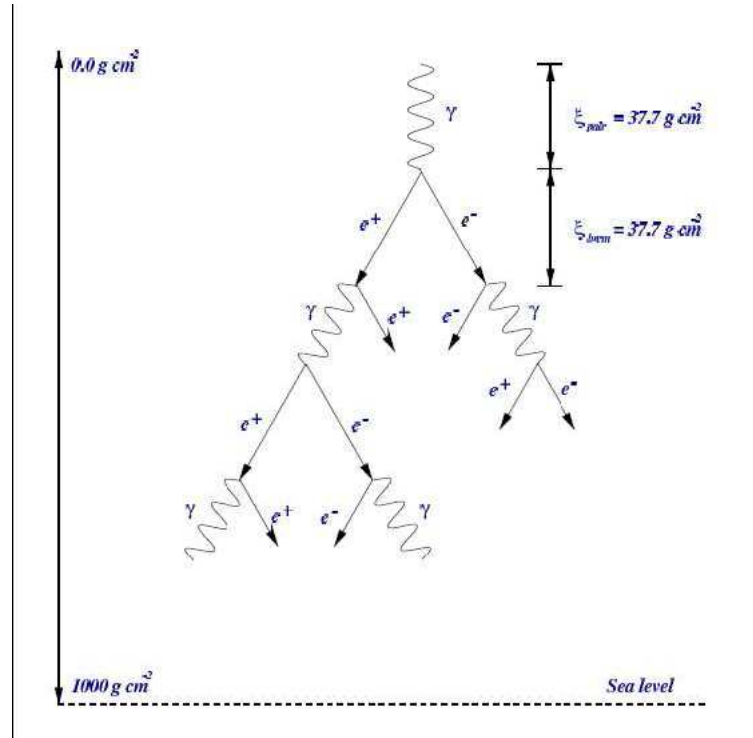


Figure 2.2: Schematic image of an air shower. Taken from Celik (2008).

are so energetic that they travel faster than the speed of light in air. When such energetic particles go through the air, the local electromagnetic field is disturbed by their charge, and the atoms of the air molecules are polarized accordingly. When the polarized molecules go back to equilibrium, they radiate photons isotropically like a ripple. As the source of the radiation travels faster than the local speed of light, the ripples bunch up to an envelope which becomes a wavefront, analogous to the sonic boom produced by an object traveling faster than the speed of sound in

air (see Fig. 2.3). This phenomenon is called Cherenkov radiation. The angle θ_c in Fig. 2.3 (right) is called the Cherenkov angle:

$$\cos \theta_c = \frac{c/n}{\beta c} = \frac{1}{\beta n} \quad (2.1)$$

Then

$$\theta_c = \cos^{-1} \frac{1}{\beta n} \quad (2.2)$$

Using the relation $\beta = \sqrt{1 - (E_0/E)^2}$ (E is the energy and E_0 is the rest energy

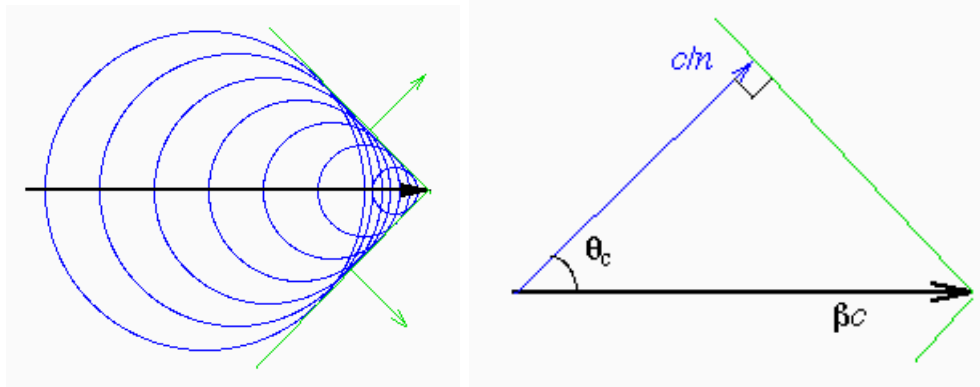


Figure 2.3: When a charged particle moves faster than the local speed of light (**Left**), the envelope of the radiation adds up to Cherenkov radiation (**Right**). Credit: C. N. Booth/The University of Sheffield

of a particle, respectively), we have

$$\theta_c = \cos^{-1} \frac{1}{n\sqrt{1 - (E_0/E)^2}} \quad (2.2)$$

The Cherenkov radiation from all the charged particles forms a filled cone centered around an axis which is set by the momentum vector of the original photon. The maximum emission occurs when the number of particles in the cascade is largest, at an altitude of ~ 10 km for primary energies of 1 TeV (Weekes, 2003). The Cherenkov

radiation makes a light pool on the ground with a radius of ~ 120 m citepWeekes03. The wavelength of Cherenkov light peaks at 300-350 nm at ground level, which corresponds to the ultraviolet-blue part of the EM spectrum. The duration of the shower for one incoming gamma-ray photon is 3-5 nanoseconds (Eichler & Beskin, 2001).

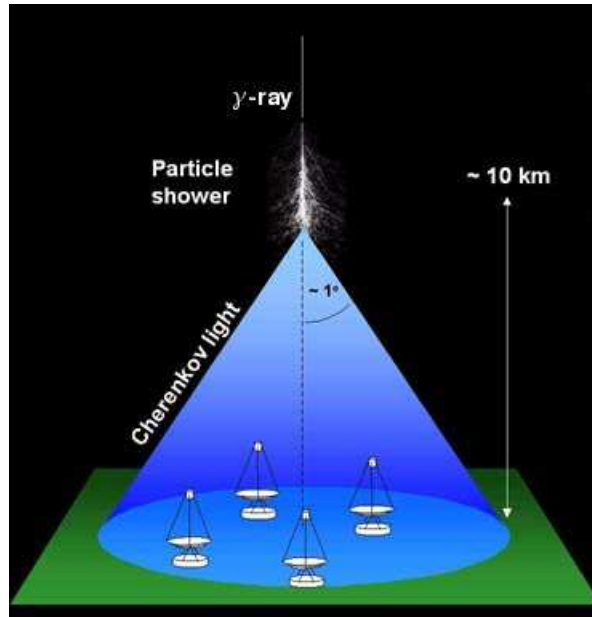


Figure 2.4: The cone of Cherenkov radiation generated by the air shower, making a light pool of radius ~ 130 m on the ground. Credit: The H.E.S.S. Collaboration

2.2 Event Reconstruction

With multiple telescopes, the same shower can be imaged from different points of view. The position of the primary particle (gamma-ray or cosmic ray) on the sky map, and the direction it came from, can be reconstructed by overlapping the images from the multiple telescopes and intersecting the extensions of the longer axis of the images (see Sec. 3.3.2). Images from gamma-rays are narrow ellipses whose major axis is the vertical extension of the shower (see Fig. 2.6, left). Images from cosmic-rays are wider and have no preferred orientation (see Fig. 2.6, right),

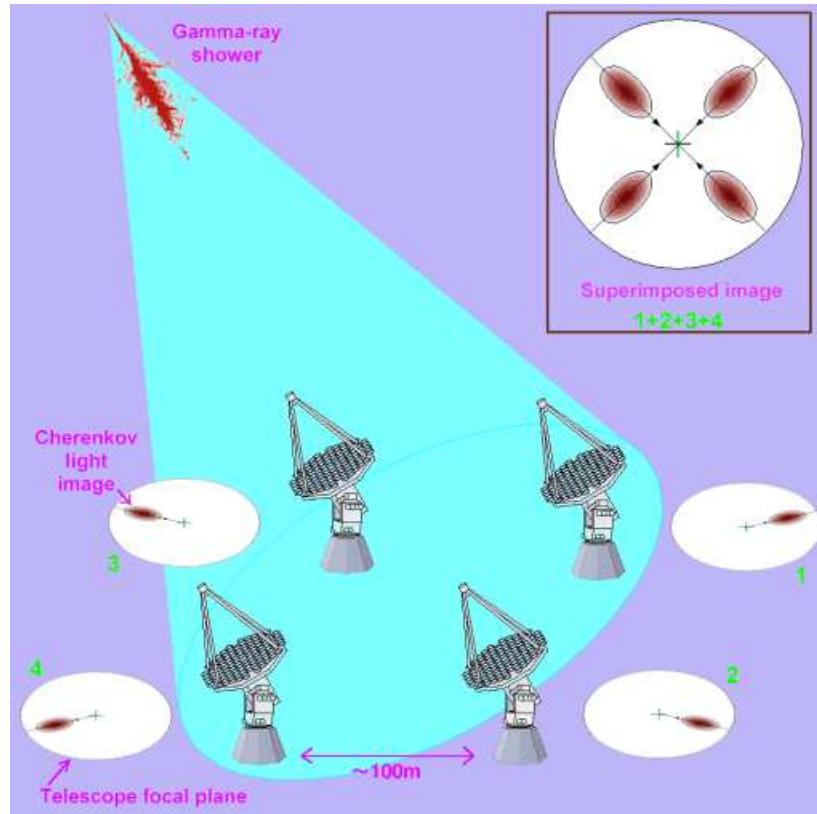


Figure 2.5: The air shower looks different at the different telescopes, but its source position should be the same place on the camera plane. Credit: The CANGAROO Collaboration.

due to the Lorentz force they experience when passing magnetic fields on their way. We use these differences to distinguish the signals from gamma-rays from the cosmic ray background.

2.3 Overview of VERITAS Hardware

The Very Energetic Radiation Imaging Telescope Array System (VERITAS) is a telescope array composed of four Cherenkov telescopes stationed at the Fred Lawrence Whipple Observatory in Amado, Arizona, south of Tucson. It is sensitive in an energy range from 100 GeV to 50 TeV, and the effective area for the incoming gamma-rays is $\sim 10^5 \text{ m}^2$ (Holder et al., 2006). Its angular resolution is $\sim 0.05^\circ - 0.15^\circ$, depending on energy, while its energy resolution is $\sim 15\%$ (Holder et al.,

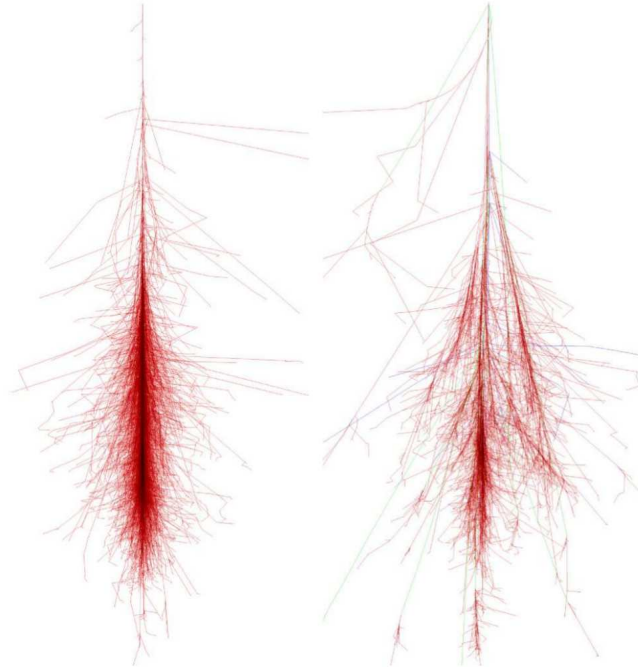


Figure 2.6: Lateral views of a 100GeV photon initiated air-shower (**Left**) and a 100 GeV cosmic ray initiated air-shower (**Right**) (Monte Carlo simulation). Taken from Cogan (2006).

2008). The field of view of the telescope array is 3.5° (Holder et al., 2006).

2.4 The Positioner and Optical Support Structure of VERITAS Telescopes

Each telescope has a steel space-frame optical support structure (OSS) mounted on an altitude-azimuth positioner (see Fig. 2.7). The 12m diameter reflectors are formed by 350 identical hexagonal spherical mirrors attached onto the OSS, giving a total reflective area of 110 m^2 (Holder et al., 2006). The camera is located at a focal distance of 12 m, supported by the quadruped arms of the OSS (Holder et al., 2006).



Figure 2.7: Backside of a VERITAS telescope while under construction. The frame is the OSS. Credit: The VERITAS Collaboration.

2.5 Camera in the VERITAS Telescope

A camera is positioned at the focal point of each telescope, 12m from the mirrors in a “focus box” (see Fig. 2.8). The $1.8\text{m} \times 1.8\text{m}$ camera consists of 499 closely-packed circular photo multiplier tubes (PMTs) (see Fig. 2.9), giving a total field of view (FOV) of 3.5° (Holder et al., 2006). The motivation for the PMT usage is its relative low-cost, fast response, large detection area, and sensitivity in the UV/blue region, which corresponds to the spectral emission region of Cherenkov light. The PMTs are 29mm in diameter and arranged in a hexagonal pattern to maximize the light collection efficiency (Holder et al., 2006). To remove the dead-space between pixels, a light concentrator plate made of 499 individually molded plastic “light cones” is attached to the front of the camera (see Fig. 2.10: Nagai et al., 2007). Each of the PMTs responds with an electric current which is a function of the applied high voltage and is proportional to the light falling on its photocathode

surface.



Figure 2.8: A VERITAS telescope. The red circle shows the box in which the camera is installed. Credit: Martin Schroedter/The VERITAS Collaboration.

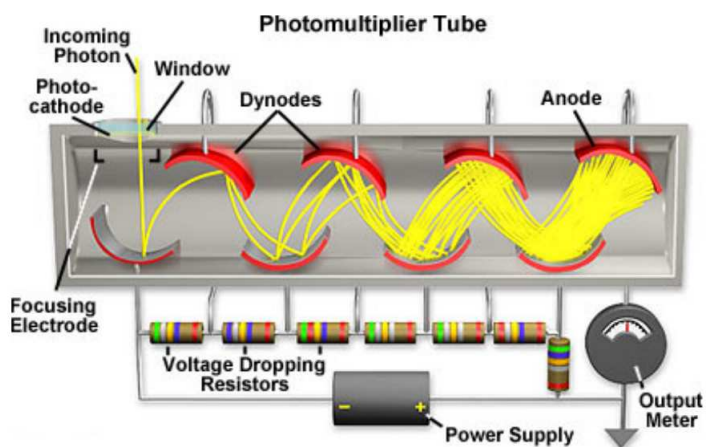


Figure 2.9: Schematic structure of one PMT. Credit: Hamamatsu Corporation

2.6 Trigger

We have to set the trigger for the data taking so that the system would be sensitive to as low an energy as possible, and while still ignoring the noise from the night sky background (NSB). For this purpose, VERITAS has a three level trigger



Figure 2.10: **(Left)** Frontal image of the camera without the light cones. **(Right)** Frontal image of the camera when the light cones are attached. Both taken from Cogan (2006).

scheme.

The first level trigger (L1) is a trigger that works at a single PMT, one pixel of a camera. The PMT converts photons into an electric current. This signal is converted to a voltage, amplified, and transmitted to a Constant Fraction Discriminator (CFD), for which the threshold is programmable. When the voltage of the input signal surpasses the programmed threshold, the trigger signal is generated. The output width of the triggered logic pulse can be set to between 4ns and 25ns.

The second level trigger (L2) is a telescope level trigger, which uses the L1 triggers as inputs, and fires only when three nearest neighbor pixels are triggered within a certain coincidence time. The gamma-ray and cosmic-ray initiated showers trigger a group of pixels, so with the L2 we can discard noise from the NSB, which triggers random pixels.

Finally, the third level trigger (L3) is an array level trigger. The VERITAS array trigger accepts L2 signals sent from each of the telescopes as its inputs, and emits an L3 signal when they lie within a preprogrammed coincidence window of between 10 and 250 ns. A large amount of the noise signals from the NSB can be

removed by the L2, but signals from local muons cannot be removed with a single telescope. The Cherenkov radiation from muons leaves an image similar to those from gamma-rays, but usually muons only trigger one telescope in an event. Thus the array level trigger removes these muon events. By employing this last trigger, the CFD threshold level can be reduced, which increases the sensitivity of the array.

2.7 FADC

The data acquisition (DAQ) chain of VERITAS begins with the FADC (Flash Analog-to-Digital Converter) boards, which we custom designed for VERITAS. For each telescope, 50 FADC boards are housed in 4 VME crates, and one FADC board has 10 channels, each of which processes one pixel signal of a camera. During data acquisition, each PMT signal is split into two: one is sent to the L1 trigger system, and the other one is fed to an FADC channel. FADC digitizes the signal in 2 ns and stores the digitized signal in a 32 μ s long memory buffer. The FADC stops recording when an L3 trigger signal is received, and then reads out the signal information of the event that triggered the L3 signal. In order to correctly read out the specific records related to the L3 signal, we need to know the correct “look-back time,” which depends on the process time for digitization, and the time between a PMT’s detection of Cherenkov light and the generation of a L3 trigger. This look-back time is determined with an appropriate flasher run (see Sec. 3.1.2) for each of the FADC boards independently. The digitized signals are used to see the time profile of the pulse and the total charge it has.

CHAPTER 3 DATA ANALYSIS

In this chapter, the techniques with which we analyze VERITAS data and obtain useful information from it are described. The VERITAS collaboration developed an off-line analysis package called VERITAS Gamma-ray Analysis Suite (VEGAS). The version used in this thesis is VEGAS 2.3.0, released on Apr 25, 2011. VEGAS has the following steps with each acting on the output of the previous steps:

Stage1 Calibration Calculation

Stage2 Application of Calibration and Data Parametrization

Stage4.2 Quality Selection and Event Reconstruction

Stage5 Shower Level Cuts

Stage6 Results Extraction

3.1 Stage1: Calibration Calculation

The data VERITAS collects has some dependencies on the character of the hardware. These dependencies include the pedestal of charge in each pixel of the cameras, the time delay that the hardware adds to the signals from the pixels, and the gain of each channel for converting photons to charge. Stage1 calculates these calibrations. Also, malfunctioning channels are removed at this stage.

3.1.1 Pedestal Removal

The night sky background (NSB) is the biggest factor of the noise that the PMTs have, and when they are not observing the Cherenkov light, the current from the PMT can have significant negative or positive fluctuations due to the NSB. So it is necessary to distinguish if the signal is from an actual event or the

NSB fluctuations. The output of the PMTs is AC-coupled, and the subsequent electronics records only negative signals, which means that only one polarity of the NSB fluctuation is recorded. To see NSB fluctuation of both polarities, a constant negative offset corresponding to about 16 digital counts, called a *pedestal*, is added to the signal. The offset for each channel is called *mean pedestal*, and the magnitude of its fluctuations due to the NSB is called *pedvar*. To measure these quantities, when there is no Cherenkov signal, the telescopes are artificially triggered at a rate of 1-3 Hz. These artificially triggered events are distinguished from actual Cherenkov-triggered events. and used for calculating the mean pedestal and the pedvar at the off-line analysis.

3.1.2 FADC Timing Calibration

The current from the camera pixels is sent to the Flash Analog-to-Digital Converter (FADC: see Sec. 2.7). The time it takes for the signals to be transmitted from the PMTs to the FADC varies from channel to channel and depends on the length of the cable, HV, and electronics. These time delays are calculated using the *flasher runs*, which are performed every night before the data-taking runs, for which all the pixels of the cameras are uniformly and synchronously illuminated.

3.1.3 Relative Gain Calculation

Ideally, each channel of the camera should return the same number of digital counts for a given number of photons. But in reality, the response can be different for each channel due to the PMT voltages, PMT aging, dust on the faces of PMTs and so on. The relative gain differences for each channel are also calculated with the flasher run of each night.

3.1.4 Pixel Status Assessment

In any given run, some channels of the cameras' malfunction because of problems with the PMTs themselves or with the high voltage system. These malfunctioning pixels are usually noisy, and their pedvar is much larger than those of the normal pixels. To find the malfunctioning pixels, we use the following quantity:

$$Relative\ pedvar = \frac{pedvar - \langle pedvar \rangle}{\sigma_{pedvar}} \quad (3.1)$$

Pixels with relative pedvar either less than -1.5 or larger than 4 are removed from the analysis.

3.2 Stage2: Application of Calibration and Data Parametrization

At this stage, the correction factors calculated in Stage 1 have already been applied to the data.

3.2.1 Image Cleaning

Normally functioning pixels of the cameras usually have a small noise signal, even when they are not observing Cherenkov radiations from an air shower. Thus we need to decide which pixels among them represent an image of an air shower. This is equivalent to removing pixels representing the noise while keeping those representing an image from the Cherenkov light. To do this, the pixels with a charge greater than $5 \times pedvar$ are sorted as the “picture pixels,” and pixels adjacent to the picture pixels and with charge greater than $2.5 \times pedvar$ are sorted as the “boundary pixels”. All the other pixels are discarded from the image.

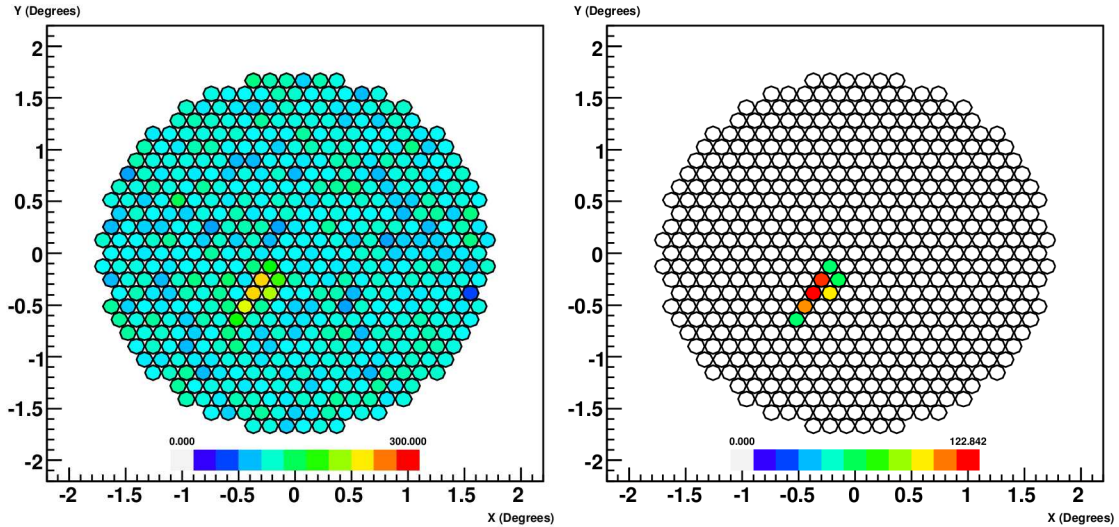


Figure 3.1: An image of a gamma-ray induced shower on a camera before (**Left**) and after (**Right**) the cleaning. Taken from Cogan (2006).

3.2.2 Image Parameterization

Cherenkov light forms an ellipse on the cameras. The information the images provide are then used to calculate quantities called the “Hillas parameters” (see Fig. 3.2 and Table 3.1), originally suggested by Hillas (1985). The Hillas parameters are used to characterize the images and distinguish the gamma-ray events from the cosmic-ray events, and to determine the location of the air shower. *Length* and *Width* (the spatial spreads of an ellipsis along the major axis and along the minor axis, respectively) are calculated with the first order and second order moments of the light distribution of the image. The 2-D (x and y) angular position of the image centroid in the camera’s coordinate system is determined by the first order moment, and the *Distance* (the distance between the centroid and the FoV) is determined with it. For a more detailed discussion of the calculation of the Hillas parameters, see Reynolds et al. (2005).

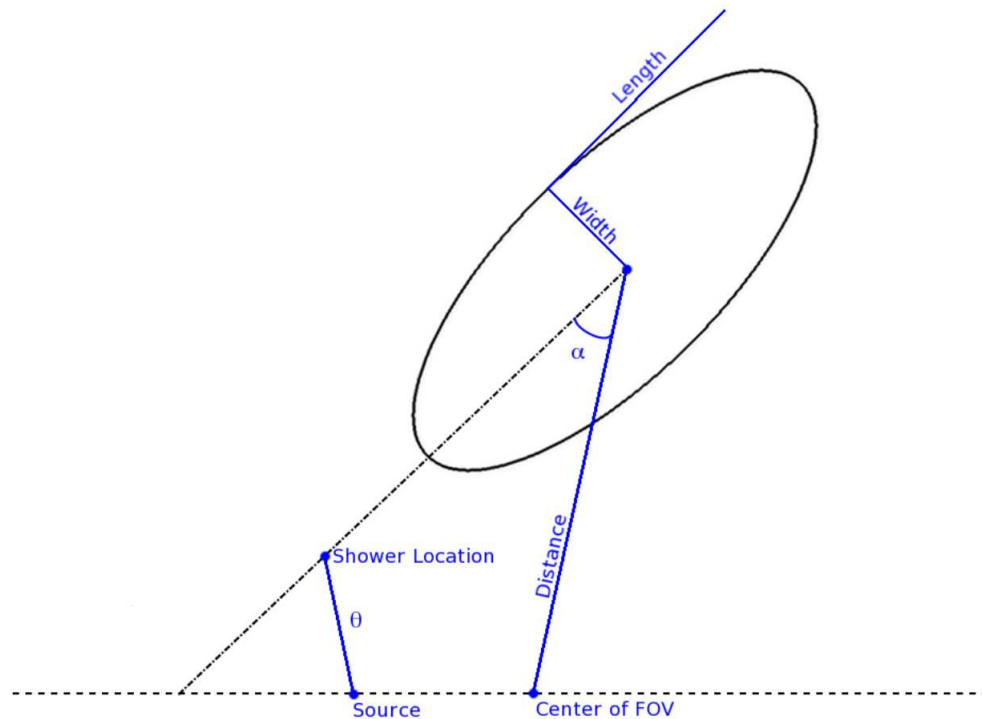


Figure 3.2: Image of a shower ellipse and the Hillas parameters. Taken from Gall (2010).

Length	RMS spread of the light along the major axis
Width	RMS spread of the light along the minor axis
Size	total charge in all the pixels in the image, corresponding to the total light content
N_{tubes}	Number of the pixel in the image
Distance	Distance between the FoV and the centroid of the ellipse
θ	Angular distance between the reconstructed source position and the center of the putative source position

Table 3.1: Examples of the Hillas parameters

3.3 Stage4.2: Event Quality Selection

3.3.1 Quality Selection

More than 99% of the recorded events are triggered by cosmic rays. A large fraction of those events can be removed while still retaining many gamma-rays by

applying cuts on the Hillas parameters that were calculated in the previous stage. It is difficult to specify the shape of images with N_{tubes} less than 5, so these are removed. Those that are too faint (small *Size*) are removed too. Lastly, ellipsoidal images should be fully contained in the camera for the correct reconstruction of the events, so those with the *Distance* greater than 1.43° are removed.

3.3.2 Shower Direction Reconstruction

One of our primary motivations is to know a spatial distribution (position information) of gamma-ray sources, and to create a gamma-ray sky map. Because a photon has no charge, it proceeds straight from the source to us, and the primary axis of the air shower is an extension of its incident trajectory. By reconstructing the incoming direction for many air showers, we can make a sky map. For this study, we used two different methods for the shower direction reconstruction. One is called the standard method, and the other one is called the “displacement method”.

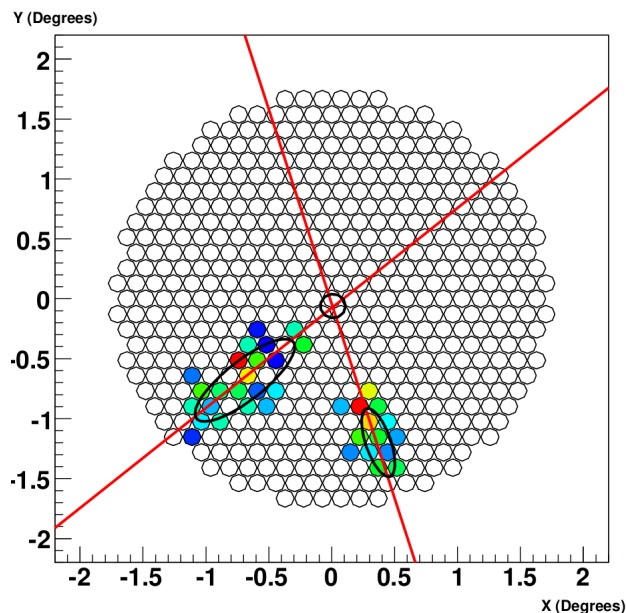


Figure 3.3: Shower direction reconstruction using the standard method. Taken from Cogan (2006).

3.3.2.1 Standard Method

In the camera plane, the arrival direction (source) of the primary particle should be on the intersecting point of the major axes of the image ellipses. From each telescope’s camera, the source position is calculated so that the weighted perpendicular distance between that point and the major axes of the ellipses are minimized. This method is called the “standard method”. The parameter *Size* is used as the weighting factor.

3.3.2.2 Displacement Method (disp method)

At a large zenith angle (LZA), the major axes of Cherenkov images of a certain event become almost parallel, and accordingly the position of the intersecting point tends to be more uncertain. So, when an observation is done at LZA, the standard method, which depends on axes-intersection, is not preferable. The “displacement (disp) method” is a method suitable for such situations. With this method, the gamma-ray arrival direction is determined by the parameter called *Displacement*, which is the distance between the centroid of an image and the putative source location. Just as in the standard method, we assume that the angular position of a source is on the extension of the major axis of an image. The parameter *Displacement* is calculated with the shape of the image ellipse and the brightness of it; the shape of the ellipse is specified by the ratio of *Width* and *Length*, and the image brightness is specified by *Size* (see Fig. 3.2 and Table 3.1). Using Monte-Carlo simulation, we calculate the relations between the displacement and the *Width/Length* ratio for various values of *Size*, and plot these in a histogram (see Fig. 3.5).

Making use of this histogram, the displacement (it is called “Separation” in Fig. 3.5) around the centroid of the image is determined from the *Width/Length*

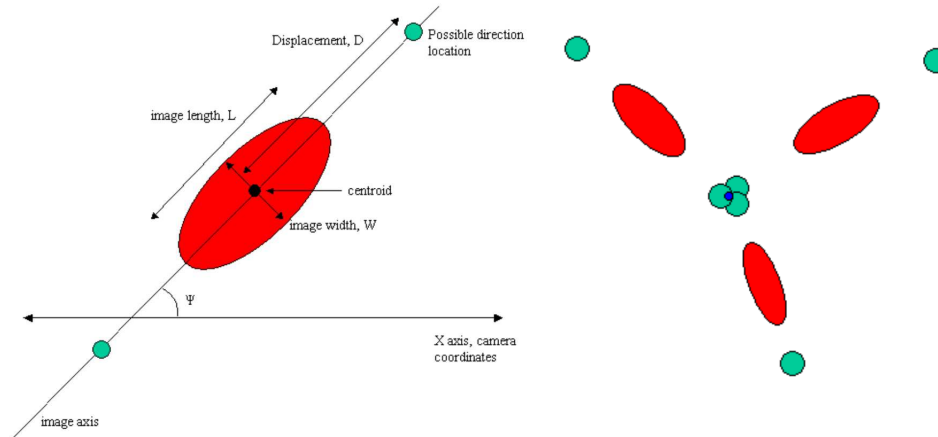


Figure 3.4: Direction reconstruction using the disp method. Each image has two direction candidates (**Left**); the one which is closer to the candidates from the other images is likely to be the correct one (**Right**). Taken from Morang (2008).

ratio and the *Size*. There is a candidate for the direction point on each side of the major axis (see left panel of Fig. 3.4); but the correct candidates from each image should all fall on the same point. The point set with the smallest RMS error is the most likely shower position (see right panel of Fig. 3.4). This method does not depend on the intersection of the axes of multiple images, so it is expected to be more reliable for targets observed at LZA. Later we compare these two method for LZA targets.

3.3.3 Shower Core Reconstruction

The Shower Core position is the location on the mirror plane (the plane perpendicular to the reconstructed shower direction) onto which the primary particle would be incident if it were to reach the ground (see Fig. 3.6). It is estimated so that the perpendicular distance to the extended major axes is minimized, using the *Size* parameter for weighting. The estimated shower energy depends on the distance between the telescopes and the shower core position, so this quantity is vitally important for the energy reconstruction.

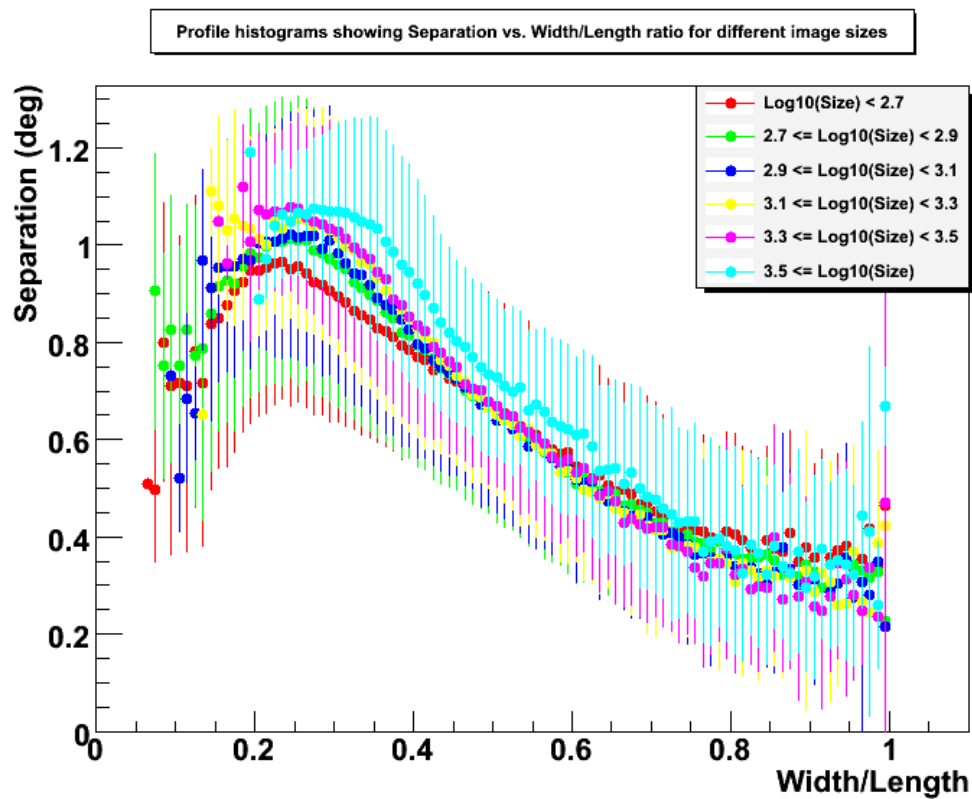


Figure 3.5: A histogram which shows the *Width/Length* vs. *Displacement* (noted as “Separation” in this image) relation for different image sizes, used for the disp method. Taken from Morang (2008).

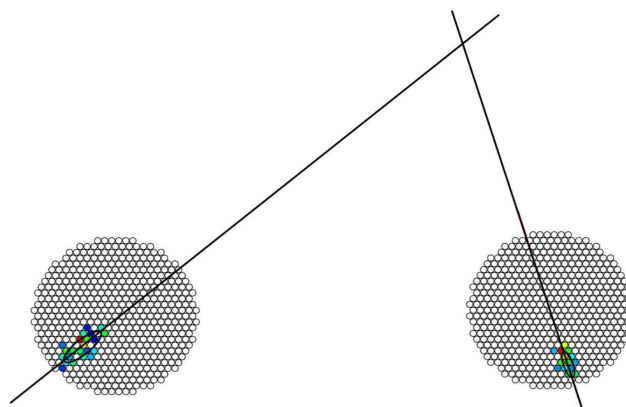


Figure 3.6: Shower core reconstruction. Taken from Cogan (2006).

3.3.4 Gamma-Ray and Cosmic-Ray Discrimination

The quantities called the *Mean Scaled Width (MSW)* and *Mean Scaled Length (MSL)* are used to distinguish gamma-ray images from those created by cosmic-rays, which are 10^4 times more likely than gamma-rays. The Mean Scaled Parameters (MSPs) are calculated for *Width* and *Length* with the values from the lookup tables. The lookup tables are generated with simulated events of gamma-rays for various values of five observing parameters: the zenith and the azimuth angle of the observation, the angular distance between the pointing direction of the telescopes and the source position, noise level (mainly due to the NSB), and the ID of the telescope (Tel1-Tel4). MSP calculated with these tables are defined as follows:

$$MSP = \frac{1}{N_{tel}} \sum_{i=1}^{N_{tel}} \frac{p_i}{\bar{p}_{sim}(Size, r)} \quad (3.2)$$

The parameter p_i is either *Width* or *Length* (to be scaled), where i denotes the ID of the telescope (1-4), and $p_i/\bar{p}_{sim}(Size, r)$ is the simulated parameter for a given *Size* and the impact parameter (*Distance*). The MSPs for true gamma-ray events should be close to 1 from their definition, and cuts on them reduces background events from the cosmic rays by a factor $>10^5$. (see Fig. 2.6 for the image profile of a gamma-ray and a cosmic-ray.)

3.3.5 Energy Reconstruction

We reconstruct the energy of the primary gamma-ray for each of the telescopes with the parameters *Size* and *Distance*, using lookup tables prepared similarly as for those for the MSPs. Then we average the reconstructed energy from each telescope using *Size* as the weight for averaging (see Fig. 3.7).

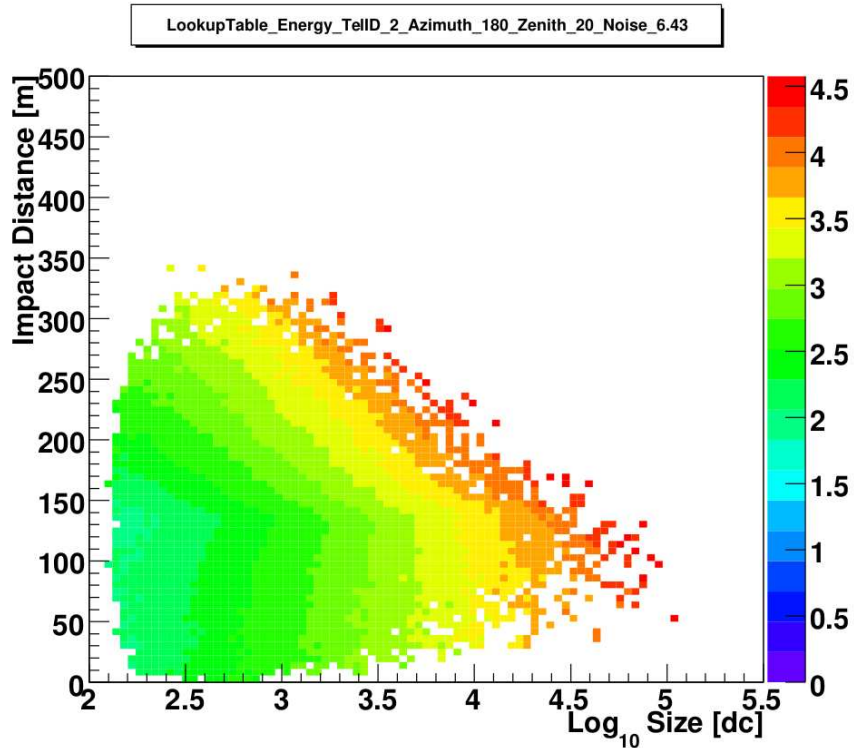


Figure 3.7: An example of energy lookup table. The horizontal axis is the logarithms of $Size$ and the vertical axis is the impact distance. The color scale is the estimated $\log(Energy[GeV])$. Taken from Celik (2008).

3.4 Stage5: Shower Level Cuts

At this stage we can impose cuts for the output file of Stage4.2. This step can be skipped, but this stage is useful for cutting out bad time intervals from the run (times with a steep spike of the trigger rates, or when clouds pass in front of the telescopes, for example).

3.5 Stage6: Results Extraction

Even after completing Stages 1 through 5, it is not possible to remove all the cosmic-ray events from the data. So it is still necessary to estimate the background in the final stage of VEGAS, Stage6. Also, the background level calculation is a must

in the process of the 2-D sky map creation. For these purposes VEGAS adopts two different methods for background estimation: one is the “ring background model,” and the other is the “reflected region model” (wobble model). These two each have their own merits and drawbacks. The number of excess gamma-ray counts is defined as

$$N_\gamma = N_{on} - \alpha N_{off} \quad (3.3)$$

where N_{on} is the number of events in the source region (“ON region”), N_{off} is the number in the background region (“OFF region”), and α is a normalization factor, which is the relative exposure calculated from the differences in area and observing time.

3.6 Ring Background Model

For the ring background model, the OFF region is an annulus around the source region. This method is preferred for the “Sky-Survey” observing mode, in which there is no specific target, and for generating sky maps, where the background must be calculated over the full field of view. The inner radius of the annulus must be large enough that there is no contamination from the source, and the parts of the annulus that cross a known gamma-ray source or bright star must be removed. For this model, the α parameter is defined as follows:

$$\alpha = \frac{\int_{on} \epsilon(r) dA}{\int_{off} \epsilon(r) dA} \quad (3.4)$$

where $\epsilon(r)$ denotes the acceptance, relative event rate at that point on the camera plane, at the point r , and dA is the differential area. In the ring background model, where the background is an annulus around the target, the acceptance of the camera is not azimuthally symmetric. This is because we can have the source position at

an arbitrary point on the camera plane. Thus we need to calculate the acceptance at each point to obtain α , as in eq. (3.4).

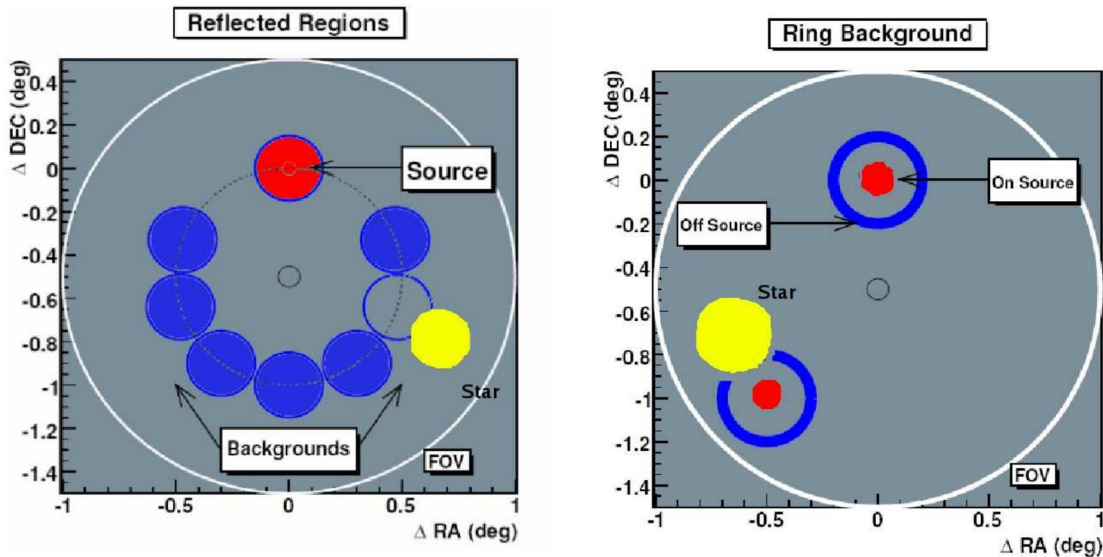


Figure 3.8: The locations of the ON region and the OFF region for the reflected background region model (**Left**), and for the Ring Background model (**Right**). Taken from Celik (2008).

3.7 Reflected Region (Wobble) Model

The most common operating mode of the VERITAS telescope array is the “wobble mode,” for which the observational target is offset from the center of the FoV by $\pm 0.3^\circ$ or $\pm 0.5^\circ$ in right ascension or declination (north, south, east, or west). The reflected region (wobble) model is the background selecting scheme specialized for this observing mode. For this model, a region with a certain radius around the source position is taken as the ON region. In the wobble observing mode, the distribution of the incoming cosmic ray rate is assumed to be azimuthally symmetric around the center of the FoV, due to the isotropic nature of cosmic rays. So the OFF regions having the same area and the same offset from the center of the FoV with the ON region are selected. Just as in the ring background model, regions that

include known sources or bright stars must be avoided. Statistically, it is preferable to have as many OFF regions as possible. The α parameter can be defined as in eq. (3.4), and it is equivalent to $\alpha = 1/N$, where N is the number of OFF regions.

The excess count (eq. (3.3)) is a simple subtraction of background from the ON region events. So it varies as we change the observing time and with how we choose the ON region and the OFF regions. To measure the strength of the source in a way that is less dependent on these factors, we define the quantity “significance” as follows (Li-Ma, 1983):

$$\sigma = \sqrt{2} \left\{ N_{on} \ln \left[\left(\frac{1 + \alpha}{\alpha} \right) \left(\frac{N_{on}}{N_{on} + N_{off}} \right) \right] + N_{off} \ln \left[\left(1 + \alpha \right) \left(\frac{N_{off}}{N_{on} + N_{off}} \right) \right] \right\}^{\frac{1}{2}} \quad (3.5)$$

The gamma-ray rate from the source can be calculated as follows:

$$Rate_{\gamma} = \frac{N_{on} - \alpha N_{off}}{T} \pm \frac{\sqrt{N_{on} + \alpha^2 N_{off}}}{T} \quad (3.6)$$

where T is the observing time after the correction for the dead-time. The rate for the background is

$$Rate_{bg} = \frac{\alpha N_{off}}{T} \quad (3.7)$$

3.8 Spectrum Reconstruction

Another important job of Stage6 is the reconstruction of the energy spectrum of the gamma-rays. VEGAS is used to reconstruct the energy of each primary gamma-ray photon. To determine the differential energy flux of the gamma-rays, the collection areas of VERITAS for gamma-rays of each energy bins must be calculated. The VERITAS telescopes do not catch primary gamma-rays; they collect gamma-rays “indirectly” by observing Cherenkov emissions from an air shower triggered

by the gamma-rays, which extends radially, radius ~ 60 m. The effective collection area is calculated for various energies of the primary particle, zenith angle, NSB level, offset of the source from the center of the FoV, and applied cuts during the analysis. $N_0(E, \theta)$ is a number of Monte-Carlo simulated air showers initiated by gamma-rays with energy E (θ is the zenith angle of the telescope array). Simulated gamma-rays are scattered over an area $A_0(E)$ around the array, greater than the area that VERITAS covers. These simulated events are processed through a simulation of the detectors, and the simulated detectors' responses are recorded as data files, just as real events are processed. These files are then processed through the VEGAS analysis, and a certain number of simulated gamma-rays, $N_{tr}(E, \theta)$, are successfully reconstructed. The effective area for the detector with zenith angle θ and energy E of the primary particle can then be expressed in the following form:

$$A_{eff}(E, \theta) = \frac{N_{tr}(E, \theta)}{N_0(E, \theta)} A_0(E) \quad (3.8)$$

However, VERITAS has a finite energy resolution, and the reconstructed energy does not always represent the true energy. So, there is some shift in the value of $N_{tr}(E, \theta)$, and it must be corrected according to the distribution of the error in the reconstructed energy. With this correction, a ‘‘modified effective area,’’ \tilde{A}_{eff} , is given.

The differential flux in the i 'th energy bin E_i can be expressed in the following equation:

$$\frac{dN}{dE}(E_i) = \frac{1}{\Delta t \Delta E_i} \left\{ \sum_{j=1}^{N_{on,i}} \frac{1}{\tilde{A}_{eff}(E_j, \theta_j)} - \alpha \sum_{k=1}^{N_{off,i}} \frac{1}{\tilde{A}_{eff}(E_k, \theta_k)} \right\} \quad (3.9)$$

where Δt is the live time for the observation, ΔE_i is the energy bin width, $N_{on,i}$ is the ON count in the i 'th energy bin, similarly for $N_{off,i}$, and α is the normalization

factor explained in the previous section (see Fig. 3.10).

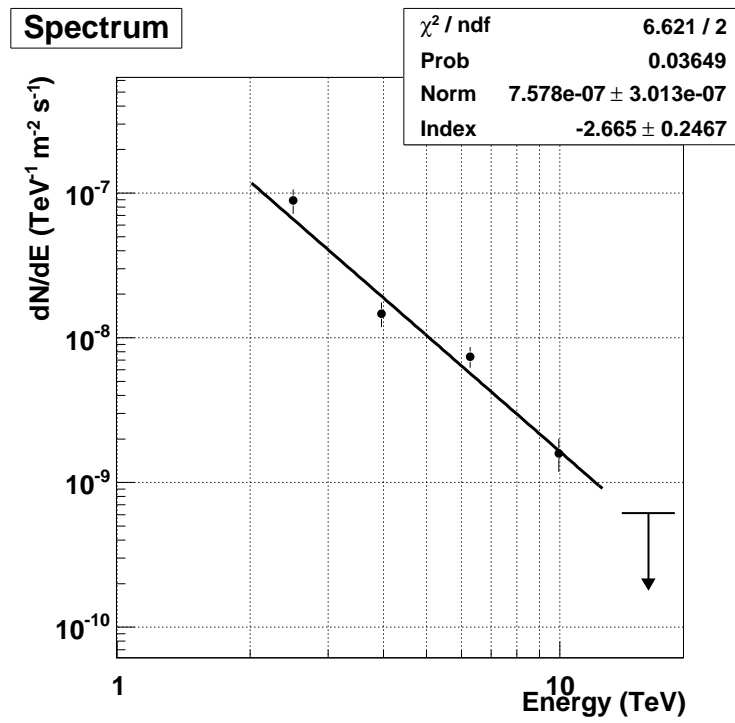


Figure 3.9: Example of a spectrum reconstructed by VEGAS, which obeys the power law derived earlier.

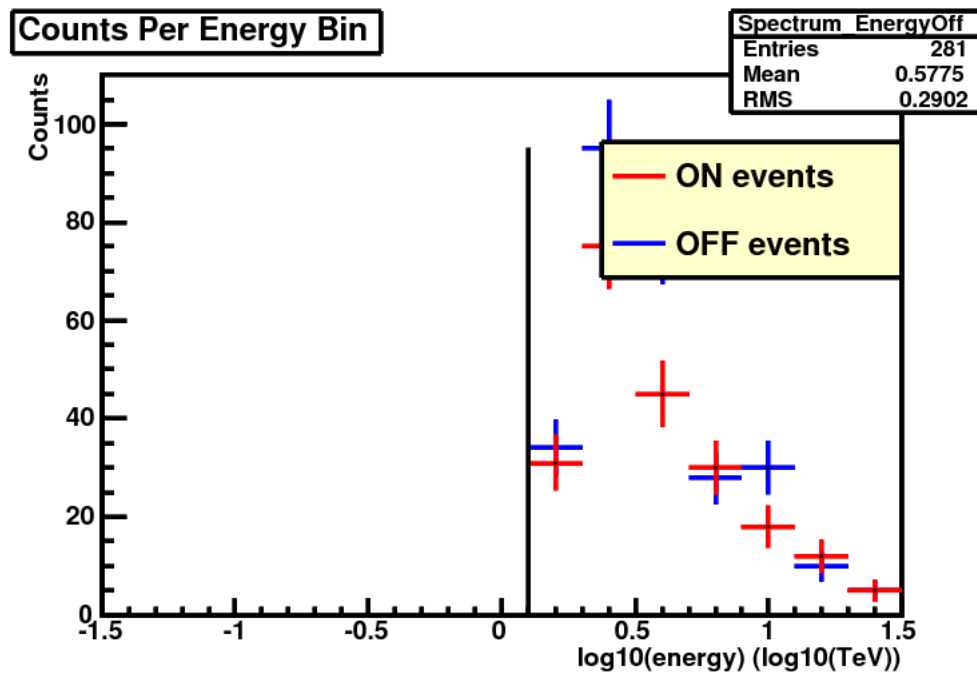


Figure 3.10: The counts (ON&OFF) per logarithmic energy bin for the Crab. Created by VEGAS with the disp method.

CHAPTER 4

FERMI ACCELERATION MECHANISM

A primary concern of my research is the acceleration mechanism of very high energy gamma-rays. As mentioned in the introduction, the observed spectra typically obey a power law distribution, which means that they are not of thermal origin. To explain non-thermal spectra, the acceleration mechanism first proposed in 1949 by the particle physicist Enrico Fermi (1901-1954) is largely accepted nowadays (Fermi, 1949). This mechanism is called “Fermi-acceleration,” or sometimes “diffusive shock acceleration.” It is a stochastic mechanism by which charged particles are reflected by “magnetic mirrors”¹. In turbulent fields, charged particles are repeatedly reflected and accelerated to high energies. Thus, the kinetic energy of macroscopic flows is transferred to single particles. In Sec. 4.1 the mechanism of “shock waves,” at which Fermi acceleration occurs, will be introduced. There are two different theoretical schemes for Fermi acceleration: “Fermi acceleration of the second order” and “Fermi acceleration of the first order.” Second order acceleration is the original idea proposed by Fermi. First order acceleration, developed later, is particularly related to our research. This will be explained in Sec. 4.2.

4.1 Shock Waves

In a gaseous medium, turbulence generally propagates with the local speed of sound as a wave. When a disturbance propagates with supersonic velocity, it will no longer behave like a sound wave. In that case there will be a discontinuity where the pressure, the density, and the normal velocity change abruptly. Such

¹When charged particles move into a stronger magnetic field, they gain the kinetic energy of the perpendicular motion, but because of the conservation of energy, they lose the kinetic energy of the parallel motion. If the magnetic field becomes sufficiently strong, the parallel (drift) component of the motion becomes zero and the particles are reflected back. This phenomenon is called “magnetic mirroring.”

a discontinuity is called a “shock wave” (or a “shock front”), and this is the key mechanism for Fermi acceleration. The discussion hereafter follows p. 315-319 of Longair, volume 1 (1992) and p. 320-335 of Landau (1987).

The gas ahead of the shock wave is stationary, and we assign density ρ_1 , pressure p_1 , and the temperature T_1 to it. The gas behind the shock wave, which propagates with supersonic velocity, we assign density ρ_2 , pressure p_2 , and the temperature T_2 . We assume that the propagation velocity of the shock front is U , as in Fig. 4.1 (left). For convenience, we proceed in the coordinate system in which the shock front is stationary, as in Fig. 4.1 (right). In this coordinate system, the gas ahead of the shock moves toward the shock front with velocity $v_1 = |U|$, and when it goes across the shock it flows away with the velocity v_2 . The state of the gas changes abruptly as it passes through the shock front, but some conservation laws must hold due to the continuity of the medium across the shock.

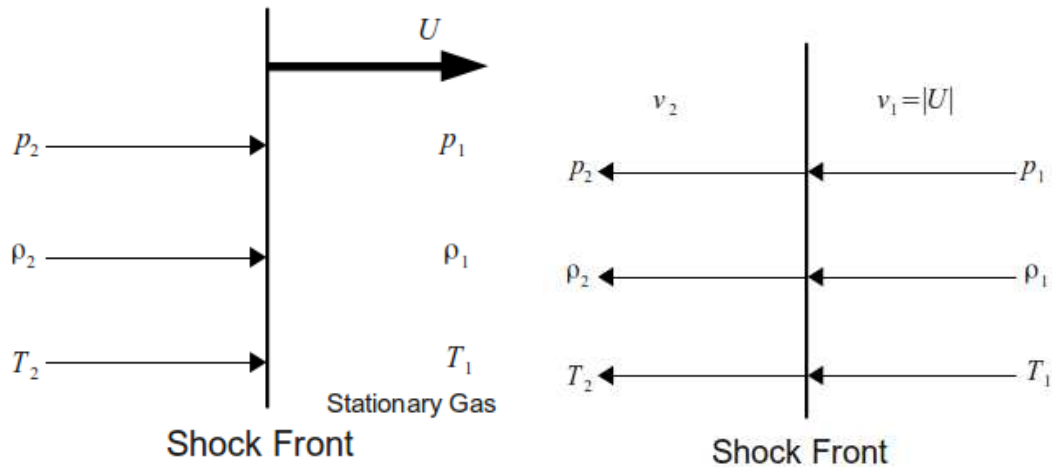


Figure 4.1: **(Left)** A shock wave propagating in a stationary medium with velocity U . **(Right)** A shock wave seen in the frame where the shock front is stationary.

Firstly, the mass of the gas should be conserved before and after passing the

shock front:

$$\rho_1 v_1 = \rho_2 v_2 \quad (4.1)$$

Secondly, the energy flux (the energy that passes through the shock with the speed and the direction of v_1 per unit area) is continuous:

$$\rho_1 v_1 \left(\frac{1}{2} v_1^2 + w_1 \right) = \rho_2 v_2 \left(\frac{1}{2} v_2^2 + w_2 \right) \quad (4.2)$$

In the equation above, w is the enthalpy $w = \epsilon_m + pV$, where ϵ_m is the internal energy per unit mass, and $V = \rho^{-1}$ is the volume per unit mass. The first term in the parenthesis corresponds to the kinetic energy, due to the macroscopic flow of the gas, not the random microscopic motion of the molecules of the gas (this should be ascribed to ϵ_m in w , the internal energy proportional to the temperature). pV in w is the work done by the gas when it passes through the shock front.

Thirdly, momentum flow is conserved:

$$p_1 + \rho_1 v_1^2 = p_2 + \rho_2 v_2^2 \quad (4.3)$$

where ρv is the “density of momentum,” i.e. the momentum carried by the gas in a unit volume. The volume swept by a unit area parallel to the shock front along the gas is v , so the amount of momentum that passes through a unit area of the shock front in the unit time is $(\rho v) \times v = \rho v^2$. The term $(p_2 - p_1)$ is equivalent to the “impulse” that the gas applies to the unit area of the shock front in a unit of time.

The three equations given above are called the *Rankine-Hugoniot conditions* or, more generally, the *shock conditions*.

The quantity specified by eq. (4.1) is called the mass flux, and we define it as

$$j = \rho_1 v_1 = \rho_2 v_2 \quad (4.4)$$

Then we have the following relations:

$$j^2 = \frac{(p_2 - p_1)}{(V_1 - V_2)} \quad (4.5)$$

$$v_1 - v_2 = [(p_2 - p_1)(V_1 - V_2)]^{\frac{1}{2}} \quad (4.6)$$

Combining eq. (4.1), eq. (4.2), and eq. (4.4), we find

$$\frac{1}{2}j^2V_1^2 + w_1 = \frac{1}{2}j^2v_2^2 + w_2 \quad (4.7)$$

With eq. (4.5), this becomes

$$w_1 - w_2 + \frac{1}{2}(V_1 + V_2)(p_2 - p_1) = 0 \quad (4.8)$$

In case of an ideal gas, the enthalpy is $w = \gamma pV/(\gamma - 1)$. For simplicity we assume that the gas is ideal, and use this relation for eq. (4.8):

$$\frac{v_2}{V_1} = \frac{p_1(\gamma + 1) + p_2(\gamma - 1)}{p_1(\gamma - 1) + p_2(\gamma + 1)} \quad (4.9)$$

Because we assumed that the gas is ideal,

$$\frac{T_2}{T_1} = p_2V_2p_1V_1 = \frac{p_2p_1(\gamma + 1) + p_2(\gamma - 1)}{p_1p_1(\gamma - 1) + p_2(\gamma + 1)} \quad (4.10)$$

From eq. (4.5), we remove V_2 using eq. (4.9)

$$j^2 = \frac{p_1(\gamma - 1) + p_2(\gamma + 1)}{2V_1} \quad (4.11)$$

The squared velocity can be obtained with eq. (4.1) and eq. (4.11).

$$v_1^2 = j^2 V_1^2 = \frac{V_1}{2} [p_1(\gamma - 1) + p_2(\gamma + 1)] \quad (4.12)$$

$$v_2^2 = j^2 V_2^2 = \frac{V_2}{2} \frac{[p_1(\gamma + 1) + p_2(\gamma - 1)]^2}{p_1(\gamma - 1) + p_2(\gamma + 1)} \quad (4.13)$$

For the left hand side of eq. (4.9), the relation $\rho = V^{-1}$ was used. Now we define the *Mach number* as $M_1 = v_1/c_1$, where c_1 is the velocity that the sound propagates in the undisturbed gas, and $c_1 = (\gamma p_1/\rho_1)^{\frac{1}{2}}$. So we have

$$M_1^2 = \frac{v_1^2}{\gamma p_1 V_1} \quad (4.14)$$

By combining eq. (4.12) and (2.14), we have the pressure ratio as

$$\frac{p_2}{p_1} = \frac{2\gamma M_1^2 - (\gamma - 1)}{(\gamma + 1)} \quad (4.15)$$

By substituting eq. (4.14) to eq. (4.9), we have

$$\frac{\rho_2}{\rho_1} = \frac{V_1}{V_2} = \frac{(\gamma - 1)p_1 + (\gamma + 1)p_2}{(\gamma + 1)p_1 + (\gamma - 1)p_2} = \frac{(\gamma + 1)}{(\gamma - 1) + \frac{2}{M_1^2}} \quad (4.16)$$

And similarly we have the temperature ratio with eq. (4.10) and eq. (4.15) and eq. (4.16)

$$\frac{T_2}{T_1} = \frac{[2\gamma M_1^2 - (\gamma - 1)][2 + (\gamma - 1)M_1^2]}{(\gamma + 1)^2 M_1^2} \quad (4.17)$$

If we assume that the velocity of the shock wave is much larger than the velocity of sound in the undisturbed gas, which means that the shock is very strong and

$M_1 = v_1/c_1 \gg 1$, the equations for the ratios take the following forms

$$\frac{p_2}{p_1} = \frac{2\gamma M_1^2}{(\gamma + 1)} \quad (4.18)$$

$$\frac{\rho_2}{\rho_1} = \frac{(\gamma + 1)}{(\gamma - 1)} \quad (4.19)$$

$$\frac{T_2}{T_1} = \frac{[2\gamma(\gamma - 1)M_1^2]}{(\gamma + 1)^2} \quad (4.20)$$

According to eq. (4.19), if the gas is mono atomic, $\gamma = 3/5$ and then $\rho_2/\rho_1 = 4$. We use this relation later.

4.2 Fermi Acceleration of the First Order

In 1949, Fermi proposed an acceleration mechanism which explains the power-law distribution of cosmic-rays as a result of collisions between interstellar magnetic clouds and charged particles (Fermi, 1949). Charged particles will be accelerated when they collide with magnetic clouds in a “head-on” style, but decelerated when a collision is of a “catch-up” style. Because the former case is statistically more common than the latter one, particles gain energy in the entire process. With this acceleration mechanism, the energy that a particle gains in a single collision is proportional to $(V/c)^2$ (V is the velocity of the particle, and c is the speed of light), and thus this mechanism has the name of “Fermi acceleration of the second order.” The drawback of this is that the rate of energy increase is small because of the second order dependence on the velocity ratio. In late 1970’s, a more compelling mechanism for particle acceleration, the first-order scenario, was developed independently by some workers (Axford, Leer & Skadron, 1978; Krymsky, 1977; Bell, 1978; Blandford & Ostriker, 1978). The most remarkable point of this new idea is that particles experience “head-on” collisions only, which means they do not lose energy from

collisions, and the acceleration is more efficient. To introduce this mechanism, we follow the discussions of P. 352-355 of Longair, volume 2 (1992). Define the following two values, β and P . β is the factor by which the average energy of the particle is increased in one collision, and P is the probability that the particle stays in the acceleration zone after one collision. After k collisions, the number of particles still in the acceleration zone is

$$N = N_0 P^k \quad (4.21)$$

and they have the energy of

$$E = E_0 \beta^k \quad (4.22)$$

Eliminating k from these two equations,

$$\frac{\ln(N/N_0)}{\ln(E/E_0)} \quad (4.23)$$

and

$$\frac{N}{N_0} = \left(\frac{E}{E_0} \right)^{\ln P / \ln \beta} \quad (4.24)$$

By differentiating this E , we have the following relation:

$$dN(E) = K E^{\ln P / \ln \beta - 1} dE \quad (K : Constant) \quad (4.25)$$

Now let us think of the particle acceleration triggered by a strong shock that runs through the interstellar medium (see Fig. 4.2 (left)). We apply the case of the shock wave that we introduced at the end of Sec. 4.1. As we saw, $\rho_2/\rho_1 = (\gamma + 1)/(\gamma - 1)$, and if we take $\gamma = 5/3$ (the case of mono atomic molecule), then $\rho_2/\rho_1 = 4$ and $v_2 = v_1/4$ (see Fig. 4.2 (right)). Now, let us see the process in the frame where the downstream gas (ahead of the shock front) is stationary (see Fig. 4.3 (left)). In this frame, the shock front advances with the velocity U , and the gas behind

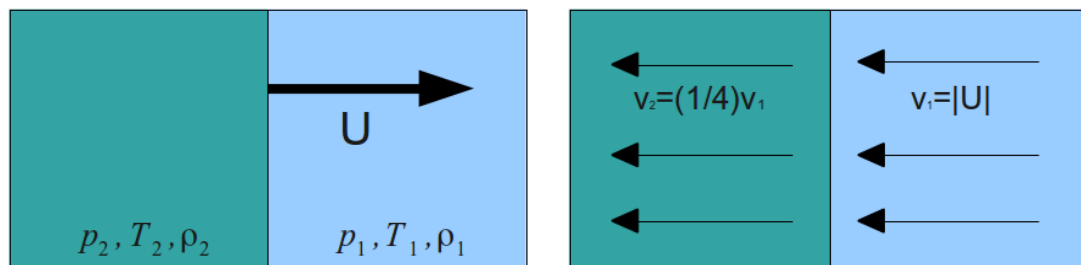


Figure 4.2: **(Left)** The shock propagating in a stationary interstellar medium with the velocity U . **(Right)** The shock in a frame where the shock front is stationary.

the shock front advances with the velocity $U/4$ toward the shock front. When a particle crosses the shock front, it gains energy by a factor of $\Delta E/E \sim U/c$ as will be explained later. After this, the accelerated particle will be advected by the gas flow behind the shock front, and will become isotropic in the frame where the gas behind the shock front is stationary.

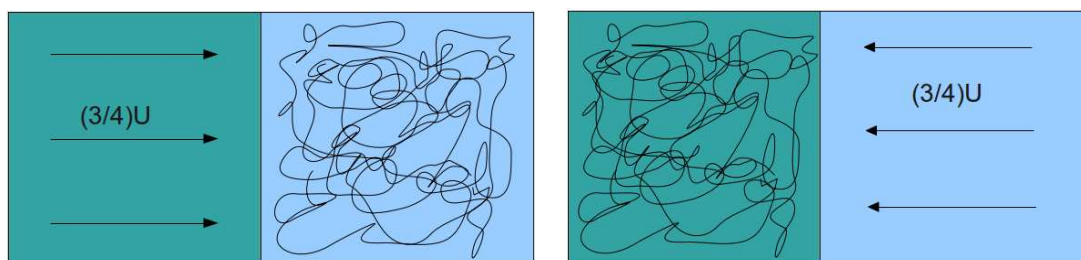


Figure 4.3: **(Left)** The shock in a frame where the downstream gas is stationary. **(Right)** The shock in a frame where the upstream gas is stationary.

Now let us see the case from the opposite viewpoint, in which the gas in the upstream region (behind the shock front) is stationary (see Fig. 4.3 (right)). In this case, when the upstream gas passes the shock front, they meet with the gas moving against them with a velocity of $3U/4$. As you can see, the particle experiences the same process as when it travels in the other direction across the shock front. This means that the particle always gains a certain amount of energy, regardless of

which direction it goes across the shock front. This is because the particle only has head-on collisions, unlike the process originally proposed by Fermi which includes catch-up collisions that make particles lose energy.

Now we calculate the energy that the particle moving from the upstream region to the downstream region with the velocity of $V = 3U/4$ gains. We take the x -axis to be along the normal of the shock front. We can obtain the energy of the particle in the frame of the downstream region by applying a Lorentz transformation

$$E' = \gamma(E + p \cos \theta V) \quad (4.26)$$

Assume that the shock is non-relativistic, $\gamma = 1$, while particles are relativistic, $E = cp$. Then, the increase of the energy of a particle per one collision is

$$\frac{\Delta E}{E} = \frac{E' - E}{E} = \frac{pV \cos \theta}{c} = \frac{V}{c} \cos \theta \quad (4.27)$$

Now we need to average this value with respect to θ . The number of particles in the angular range $\theta \sim \theta + \Delta\theta$ is proportional to $\sin \theta d\theta$. The chance for having the collision is proportional to the x -component of the velocity, $c \cos \theta$. Multiplying these two factors and applying the normalization, we have the following probability factor as a function of θ , ranging between 0 and $\pi/2$

$$p(\theta) = 2 \sin \theta \cos \theta d\theta \quad (4.28)$$

Now we can calculate the average energy gain of a particle through a one-way trip as

$$\left\langle \frac{\Delta E}{E} \right\rangle = \frac{V}{c} \int_0^{\pi/2} 2 \cos^2 \theta \sin \theta d\theta = \frac{2V}{3c} \quad (4.29)$$

As we mentioned, a particle collects the same amount of energy going either way across the shock front. So, the energy gain by a single round trip of a particle would be

$$\left\langle \frac{\Delta E}{E} \right\rangle = \frac{4V}{3c} \quad (4.30)$$

For the β we defined before, we see

$$\langle \beta \rangle = 1 + \frac{4V}{3c} \quad (4.31)$$

Now let N be the number density of particles. Bell (1978) states that according to the classical kinetic theory, the number of particles that go across the shock front is $Nc/4$. And the rate at which the particles leave the shock region is $NV = NU/4$. Then the probability that a particle is removed from the acceleration region is $(NU/4)/(Nc/4) = U/c$. The quantity P can then be written as $P = 1 - (U/c)$. Now

$$\ln P = \ln \left(1 - \frac{U}{c} \right) \approx -\frac{U}{c} \quad (4.32)$$

and

$$\ln \beta = \ln \left(1 + \frac{4V}{3c} \right) \approx \frac{4V}{3c} = \frac{U}{c} \quad (4.33)$$

Then we have

$$\frac{\ln P}{\ln \beta} = -1 \quad (4.34)$$

Finally, we find the power-law distribution of the energy spectrum by substituting this equation to eq. (4.25)

$$dN(E) \propto E^{-2}dE \quad (4.35)$$

Now, let us give a rough estimation for the maximum energy of a particle attainable at a shock wave. We follow the discussion on p. 573 of Longair (2011). Suppose \mathbf{B} is the magnetic flux density where a shock proceeds and L is the scale of a shock, or more simply, the distance a shock travels while accelerating particles to very high energies. Recall that at a shock front particles are reflected by magnetic mirrors, which are due to changes in magnetic field strength. Faraday's law is

$$\nabla \times \mathbf{E} = -\frac{\partial \mathbf{B}}{\partial t} \quad (4.36)$$

Units of curl are 1/length, so $1/L$. Units of time derivative are 1/time, so the characteristic time scale is L/U . Then, eq. (4.36) can be rewritten with L and U :

$$\frac{E}{L} \sim \frac{B}{L/U}; \quad E \sim BU \quad (4.37)$$

The maximum energy of a particle with charge ze is

$$E_{max} = \int zeE dx = zeBUL \quad (4.38)$$

If we use a simple approximation, $L \sim Ut$, then

$$E_{max} = zeBU^2t \quad (4.39)$$

This means that the highest reachable energy is proportional to the squared value

of the shock speed and the time spent for acceleration.

CHAPTER 5

V407 CYGNI

V407 Cygni is a variable star originally discovered by Hoffmeister of Sonneberg Observatory in 1940 (Hoffmeister, 1949). It is a symbiotic binary system that consists of a Mira type pulsating red giant (RG) with a 745-day pulsation period and a white dwarf (WD) companion. Its estimated distance is 2.7 kpc (~ 8800 light years). Until recently it has been considered to be mundane and only slightly variable. However, on 2010 Mar.10 8UT, two Japanese astronomers, K. Nishiyama and F. Kabashima, discovered a dramatic optical brightness change to a magnitude of ~ 6.9 (Nishiyama & Kabashima, 2010). They reported their discovery to H. Maehara of Kyoto University, who notified astronomers all around the world of this discovery.

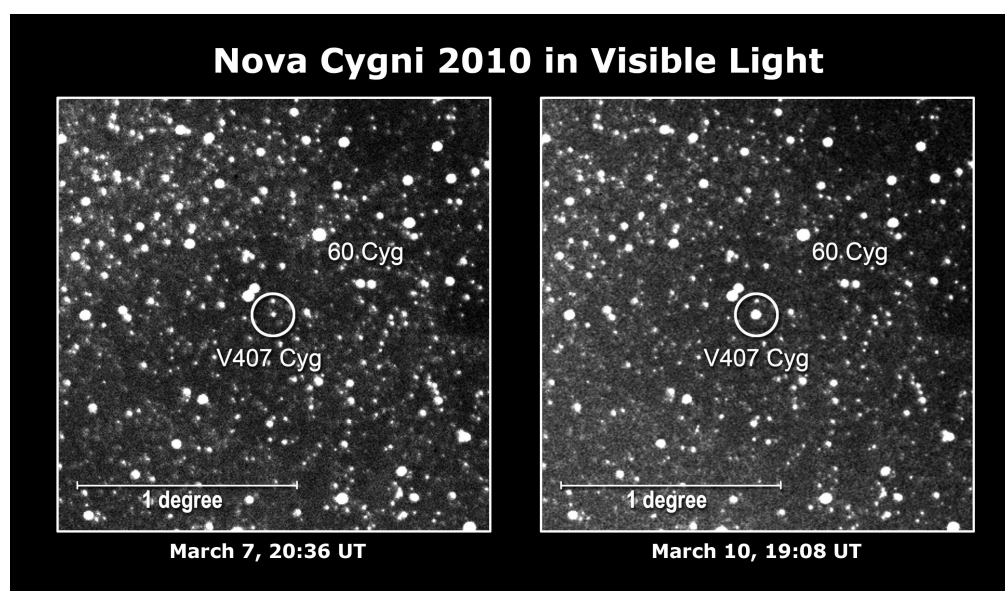


Figure 5.1: An image of Nova of V407 Cygni taken at 19:08 UT on March 10 (**Right**), and an image taken on March 7 (**Left**). Credit: K. Nishiyama and F. Kabashima/H. Maehara, Kyoto Univ.

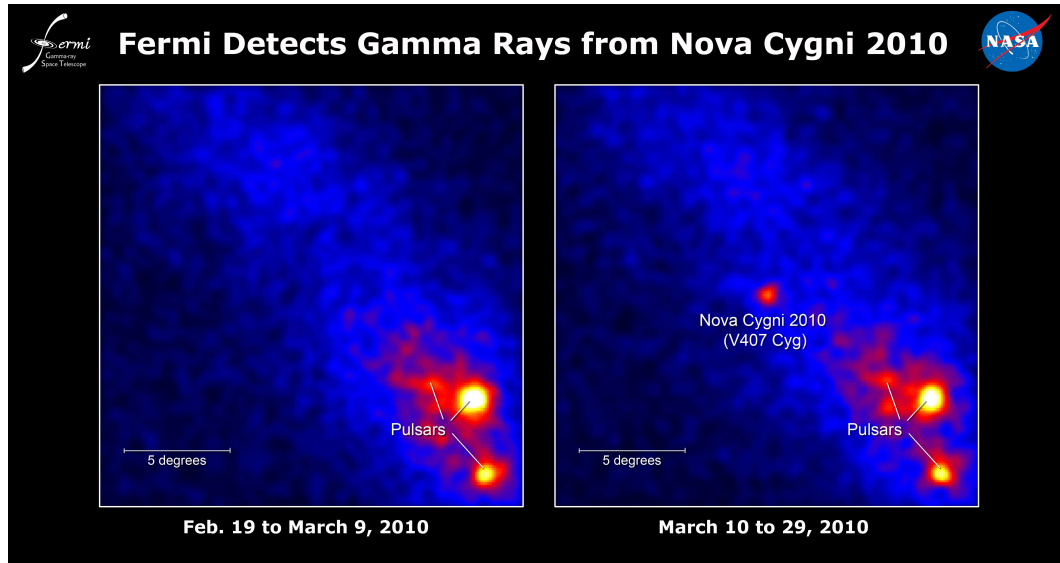


Figure 5.2: Fermi-LAT’s gamma-ray images of V407 Cygni before (**Left**) and after (**Right**) the nova. Credit: NASA/DOE/Fermi LAT Collaboration.

5.1 Fermi-LAT and V407 Cygni

Independent of the nova discovery, the Large Area Telescope on Fermi Gamma-ray Space Telescope (Fermi-LAT) of NASA detected a high energy transient gamma-ray source, FGL J2102+4542. Its first significant detection (4.3σ) was made on Mar.10, and the flux on that day was up to 3 times larger than the 1-day upper limit (95% confidence level). The flux in gamma-rays, segmented in 1 day, peaked between 13 to 14 March with a flux of 9×10^{-7} photons $\text{cm}^{-2}\text{s}^{-1}$. The significant detection ($>3\sigma$) lasted about two weeks. The Fermi-LAT collaboration obtained a position for the gamma-ray source that is 0.040° offset from the position of V407 Cygni, which is within the 95% confidence region circle (radius = 0.062°) of the LAT. Because of this proximity and the temporal correlation of the activity (see Fig. 5.3), FGL J2102+4542 is most likely associated with V407 Cygni.

V407 Cygni is a binary system in which the WD and the RG are rotating around the center of mass of the system. The WD accretes hydrogen gas emitted

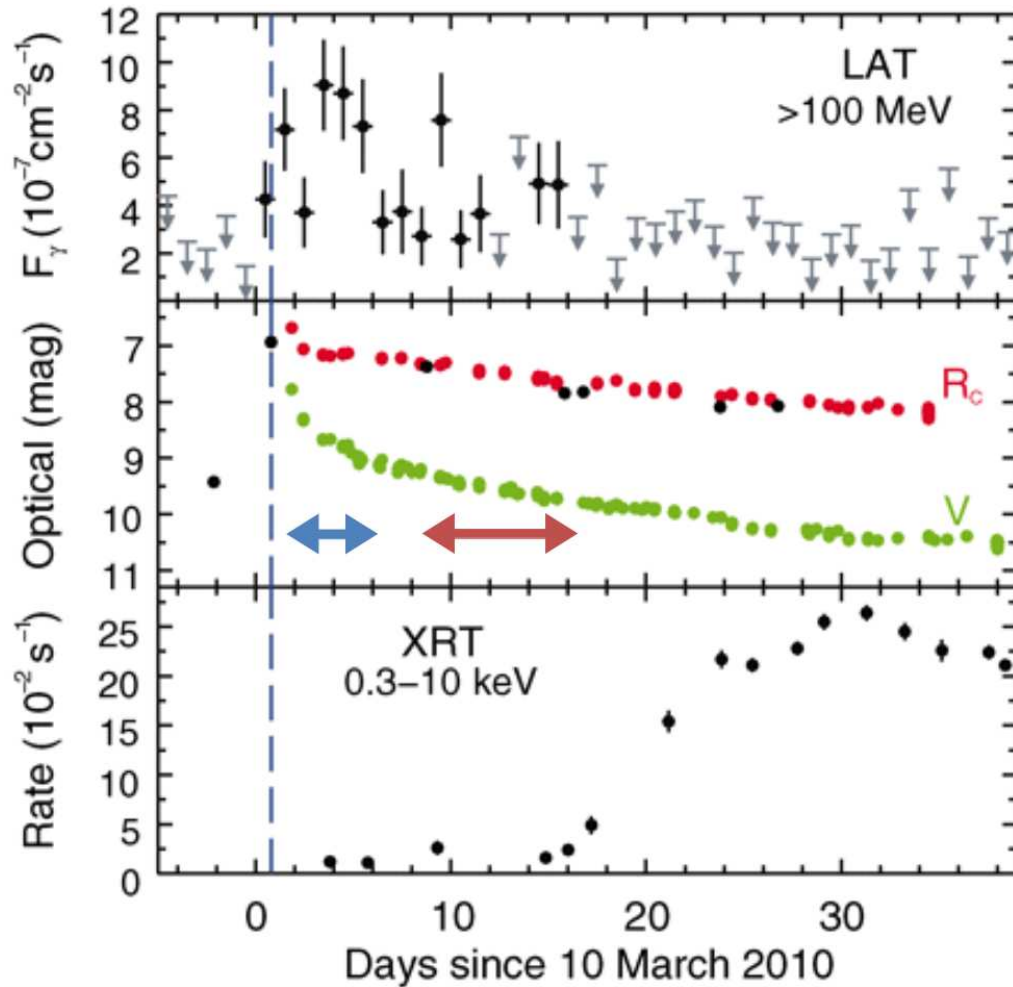


Figure 5.3: The light curves of V407 Cygni, taken from Abdo et al. (2010a). The top column is the gamma-ray taken from the Fermi-LAT. The middle column is the optical, and the bottom is X-ray from Swift. Vertical bars are 1σ statistical error. For the gamma-ray, the gray arrows indicate 2σ upper limits. The blue horizontal arrow indicates the VERITAS observational period of Crab nebula (March 12-16), and the red horizontal arrow indicates the VERITAS observational period of the V407 Cygni (March 19-26) (see Sec. 5.3).

from the RG, and when the accreted matter on the surface of the WD has high enough density and temperature, an explosive nuclear fusion reaction is triggered. Generally, this phenomenon is called a “nova” (*pl. novae*).

The Fermi-LAT detection of V407 Cygni implies that the nova generates high energy (>100 MeV) gamma-rays. Its luminosity, spectrum, and light curve, can be

interpreted as the outcome of shock acceleration in the nova shell. Observation of the radio emission from V407 Cygni showed that the emission was extended at a resolution of a few milli-arc seconds, which corroborates the idea that V407 Cygni has an extended nova shell (Abdo et al., 2010a).

This gamma-ray detection from V407 Cygni is the first example of gamma-rays from a nova, whereas X-ray emission from novae has been previously observed. The key for creating a gamma-ray is a particle (electron or proton) accelerated up to near the speed of light. The particle acceleration method for this nova is suspected to be similar to that found in supernovae. The expanding shock wave of a supernova shell (called a supernova remnant) has a speed $U \sim 10^4$ km/s and is thought to accelerate particles to very high energies via the Fermi acceleration mechanism. Gamma-rays have been detected up to energies of ~ 10 TeV. The expanding matter from the nova ($U \sim 3000$ km/s) collides with the gas from the RG ($U \sim 50$ km/s), and generates a shock wave. Thus the nova shock wave should also accelerate particles up to high energies.

5.2 Two Physical Models for Gamma-Ray Creation

The Fermi-LAT team adopted two physical models to explain the creation of gamma-rays: one is the hadronic model, and the other one is the leptonic model. In the former, a high energy p - p collision (they assumed that the protons are from the binary, either of the nova shell or the RG wind) at the shock front creates π^0 via several kinds of processes, and the π^0 immediately (after a mean life time of 8.4×10^{-17} sec) decay into gamma-rays, with a probability of 98.8%. The Fermi-LAT team analyzed the gamma-ray spectrum following the method of Kamae, Karlsson, Mizuno, Abe, & Koi (2006), assuming that the spectrum of cosmic protons is of the following form: $N_p = N_{p,0} \cdot (W_p + m_p c^2)^{-s_p} \cdot \exp(-W_p/E_{cp})$ (proton/GeV), where

W_p, E_{cp}, m_p are kinetic energy, cut-off energy, and mass of the proton, and s_p is the spectral slope in the power law factor. Gamma-ray spectra for various s_p and E_{cp} were fitted to the Fermi-LAT data, and χ^2 values were calculated for each of the data points. With these χ^2 values, they created a confidence region map of s_p and the logarithm of E_{cp} in GeV (Figure 5.8).

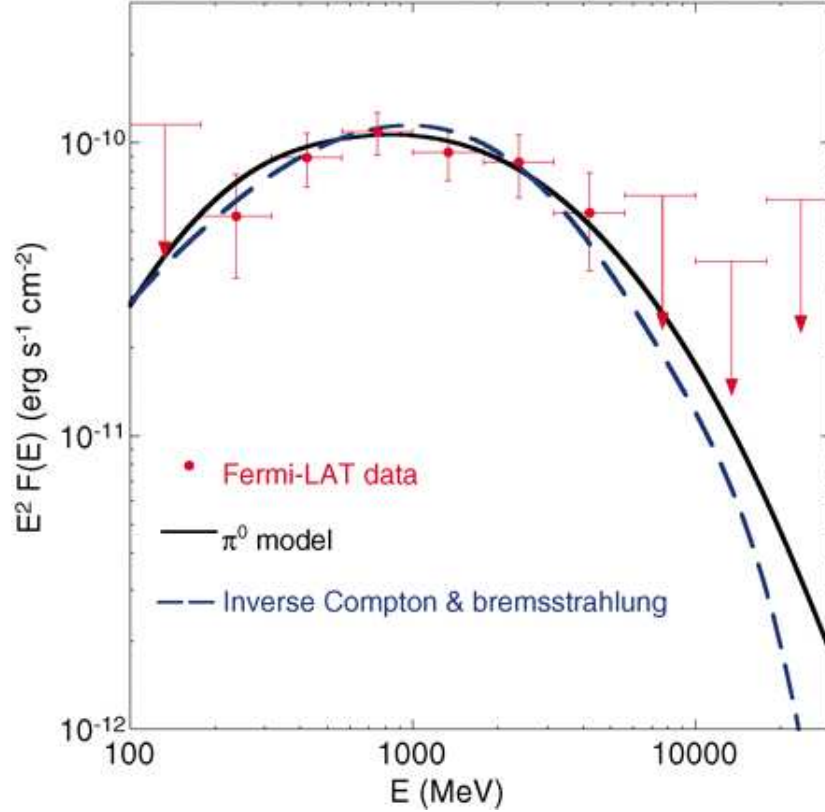


Figure 5.4: SED of V407 Cygni taken from Abdo et al. (2010a). Vertical bars indicate 1σ statistical error, arrows indicate 2σ upper limits, and horizontal bars shows energy ranges. The black solid line is the spectrum modeled with the hadronic model, the blue dashed line is the one modeled with the leptonic model.

For the leptonic model, the accelerated electrons play the main role. There are two mechanisms that are involved: Bremsstrahlung, and (Inverse) Compton scattering. The main contribution in the GeV band is from Compton scattering. In this case, electrons hit infrared photons from the RG (Fermi-LAT team assumed

that they were thermally emitted by the RG with $T = 2500\text{K}$: Supporting Online Material (SOM) of Abdo et al., 2010), and accelerate them via inverse Compton (IC) scattering. The Fermi-LAT team assumed the spectrum form $N_e = N_{e,0} \cdot W_e^{-s_e} \cdot \exp(-W_e/E_{ce})$ (electron/GeV), where W_e, E_{ce}, m_e are kinetic energy, cut-off energy, and mass of the electron, and s_e is the spectral slope in the power law factor.

5.3 VERITAS Analysis on V407 Cygni

The Fermi-LAT collaboration's initial report of GeV emission from V407 Cygni triggered VERITAS observations of the source as part of an ongoing campaign to observe very high energy (VHE: $E > 100$ GeV) transients detected by the Fermi-LAT. VERITAS observed V407 Cygni from March 10-26 in 2010 (see Fig. 5.3) in the wobble observational mode (see Sec. 3.7) with 0.5° angular offset, with the sets of predominantly 20 minutes per observation. The wobble direction cycled between North, South, East and West, to reduce the systematic error. During this period, the zenith angle of FGL J2102+4542 was between 50° and 66° . The total duration of the observation was 335 minutes, reduced to 304 minutes after removing observations with bad weather or instrumental problems.

We use the two different event reconstruction methods described in Sec. 3.7. To see the effectiveness of the disp method for the large zenith angle (LZA) data, we also analyzed observations of the Crab nebula, considered to be a "standard candle" in high energy astrophysics, which was also at large zenith angles in the sky during the observational period of FGL J2102+4542. The Crab was observed from March 12-16 in 2010 (see Fig. 5.3). The number of runs we used was 17, which adds up to 244 minutes of observing time, of which 203 minutes was used in our analysis. The zenith angle of the Crab during the observational period ranged from 55° and 65° , similar to that of FGL J2102+4542.

5.4 Results

The analysis results are displayed in Table 5.1. The Significance and the rate are higher for the disp method than for the standard method for both targets; this implies that the disp method is more effective at LZAs. The Fermi-LAT team modeled the photon energy spectrum with various values of the fitting parameters and made confidence region maps (see Sec. 5.2). Though a significant detection at the location of V407 Cygni was not found with the VERITAS observation, VERITAS covers higher energies than the Fermi-LAT. Thus, we can impose a restriction to the fitting models by calculating the flux upper limit at ~ 1 TeV. The flux upper limits (ULs) were calculated with the method of Rolke et al. (2005) from the results of both shower direction reconstruction schemes (see Sec. 3.3). To minimize the dependence on the chosen photon index, the energy at which the UL was calculated was the decorrelation energy (the energy where the differential flux fluctuates least when the photon index is changed). This yielded 1.8 TeV for the standard method and 1.6 TeV for the displacement method, with the assumption that the power law index of the photons is 2.5 (this is the default value of the power law index for simulated photon spectra in VEGAS). The energy threshold was 1.15 TeV for both of the reconstruction methods with this index (see Table 5.1). When the photons' power law index is set to 2 and 3, the calculated energy thresholds were 1.05 TeV and 1.15 TeV, respectively. If we assume a softer spectrum (index = 2), the relative portion of higher energy photons in the spectral distribution gets larger, so photon detection becomes easier, and thus we have a lower threshold energy.

5.5 Discussion

To see the validity of the gamma-ray upper limit on the object by VERITAS, we need to know the opacity of the photon path for gamma-rays generated

Reconstruction method	Standard		Displacement	
Source	Crab	J2102+4542	Crab	J2102+4542
ON (Source) counts	255	91	300	76
OFF (Backgrounds) counts	744	841	351	630
α (see Sec. 3.7)	0.111	0.125	0.111	0.125
Significance	15.7σ	0.5σ	25.1σ	1.0σ
Rate [photons/min]	0.97 ± 0.09	0.02 ± 0.04	1.40 ± 0.09	0.03 ± 0.03
Energy threshold (TeV)	1.5	1.15	1.7	1.15
Decorrelation energy (TeV)	–	1.8	–	1.6
Flux Upper Limit at decorrelation energy (99%c.l.) [E*F(E); erg cm ⁻² s ⁻¹]	–	3.49×10^{-12}	–	2.81×10^{-12}

Table 5.1: Analysis results. The disp method gives higher significance for both the Crab and J2102+4542 (V407 Cygni). Also, the flux upper limit is tighter using the disp method.

at the shock front. For the absorption of cosmic high energy photons, electron-positron pair production by photon-photon collision is the important factor (Gould & Schröder, 1967). We assumed that the gamma-ray undergoes this process with infrared photons around the RG, inside a shell with radius = 1.4×10^{14} cm around the RG (Supporting Online Material (SOM) of Abdo et al. 2010). The largest absorption occurs when the gamma-ray traverses from one point on the shell to the opposite point on the shell. To model the density distribution of the infrared photons, which is a function of the energy of the infrared photon and the distance from the RG, we used the model of Ñunez (2011). For the cross section for photon-photon collisions, we used the model of Gould & Schröder (1967). We assumed that 1 TeV is the energy of the projected photon. The energy threshold for the target photon is then 0.26 eV (p.128 in Longair, volume 1 (1992)) and we assumed the

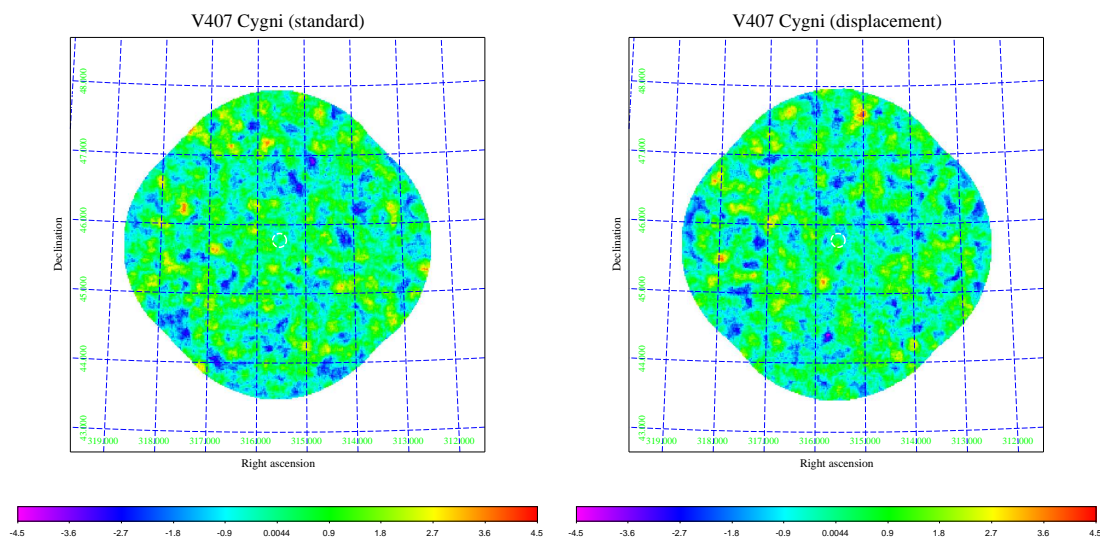


Figure 5.5: Significance maps of FGL J2102+4542 reconstructed by the two methods: **(Left)** standard method, **(Right)** disp method. The white circle at the center indicates the source position and the size of the source region used for the analysis.

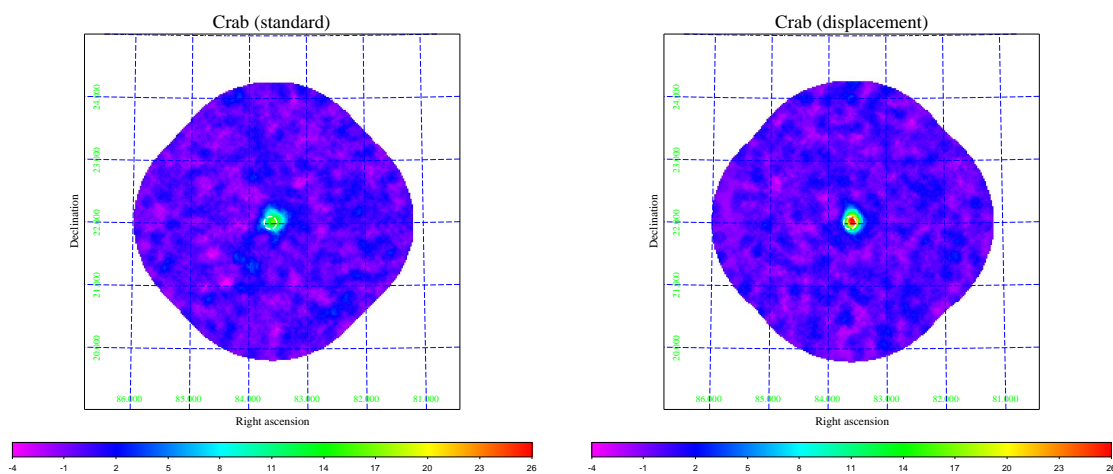


Figure 5.6: Significance maps of the Crab Nebula reconstructed by the two methods: **(Left)** standard method, **(Right)** disp method. The white circle at the center indicates the putative Crab nebula position and the size of the source region used for the analysis.

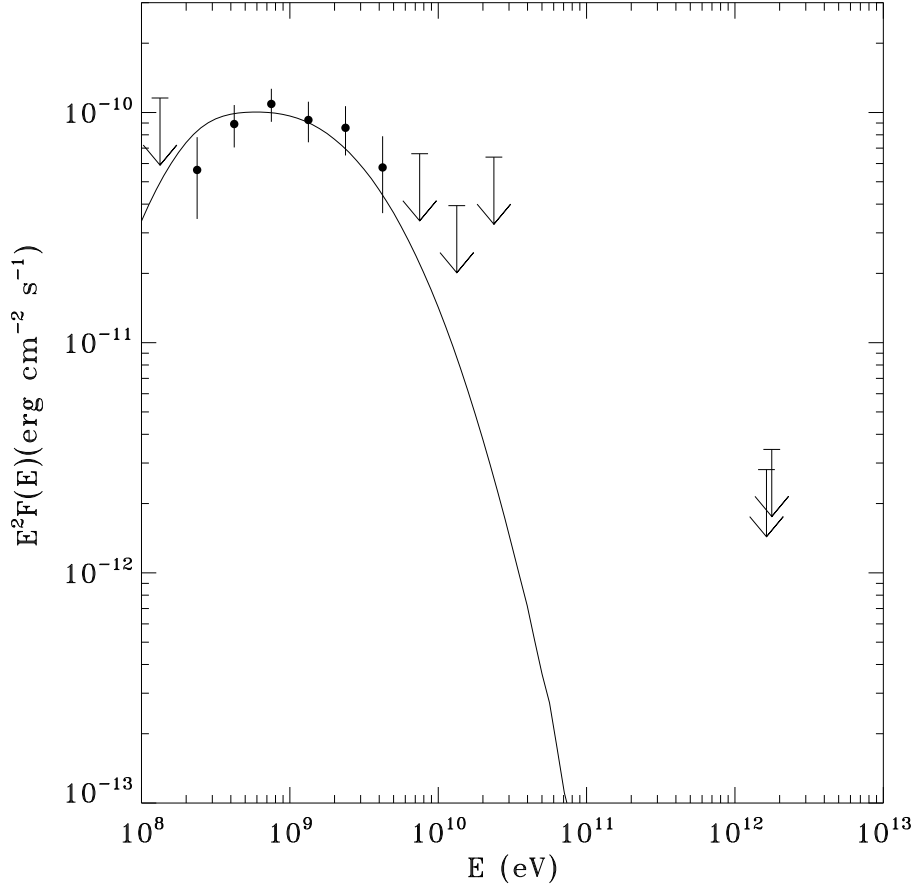


Figure 5.7: Modeled spectrum of V407 Cygni (FGL J2102+4542), modification of the spectral plot of Abdo et al. (2010a). The black dots with error bars are the Fermi-LAT’s data points. Vertical bars indicate 1σ statistical error, and arrows indicate 2σ upper limit. The two rightmost arrows show the VERITAS flux upper limits calculated using the displacement method (lower left) and the standard method (upper right) for event reconstruction. The fitting curve was constructed with the method of Kamae, Karlsson, Mizuno, Abe, & Koi (2006) with the parameters $(s_p, \log(E_{cp}))=(2.15, 1.5)$. See Sec. 5.2.

maximum energy of the target photon to be 20 eV. Then the optical depth was less than 10^{-14} . So we can say that the opacity for TeV photons from V407 Cygni is negligible.

The key for gamma-ray creation is being able to accelerate particles up to very high energies. There are two models that can explain the gamma-ray generation

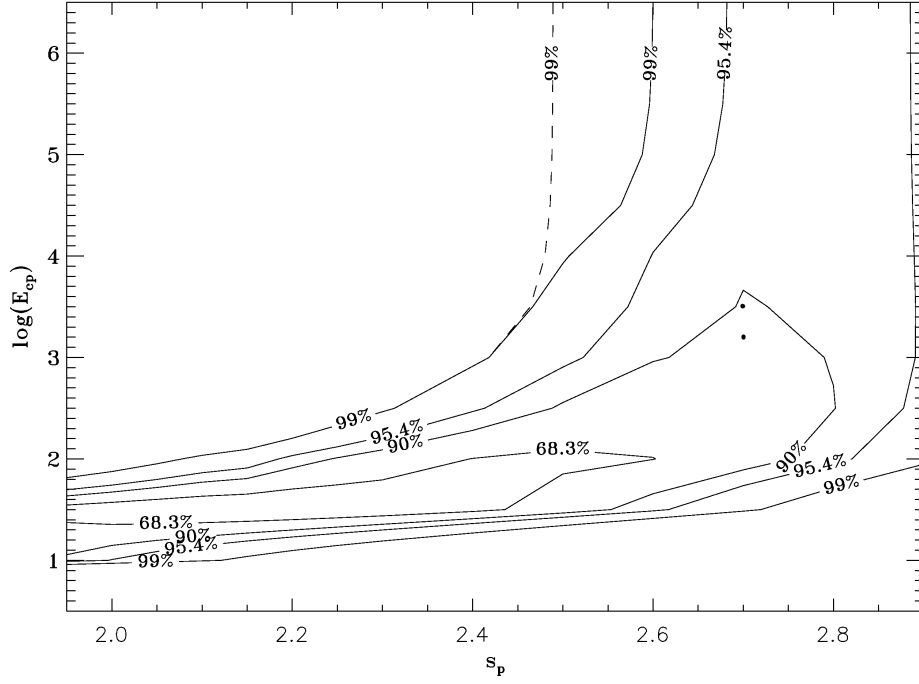


Figure 5.8: The confidence region map including the upper limit constraints from both Fermi-LAT and VERITAS (solid lines), and the one constraint from Fermi-LAT only for a 99% confidence level (broken line, taken from the Supporting Online Material of Abdo et al. (2010a)). The x-axis is the spectral slope (s_p), and the y-axis is the logarithm of the cutoff energy (E_{cp} in GeV). The maximum value of y-axis was extended from 4 to 6.5. The percentile values correspond to the confidence levels of the fit of the Fermi-LAT data (see Sec. 5.4.) The contour data from the Fermi results was provided by Pierre Jean of the Fermi-LAT collaboration.

The two dots right below the tip of the 90% level contour are the positions of the best fitting parameter sets with the cutoff energy set at the maximum attainable energies for protons: The upper dot is $(s_p, \log(E_{cp})) \sim (2.7, 3.5)$ for the extrapolation model, and the lower one is $(s_p, \log(E_{cp})) \sim (2.7, 3.2)$ for the free expansion model.

(see Sec. 5.2). For the leptonic model, we calculated the electron threshold energy for creating 1 TeV photons via inverse Compton scattering off 0.6 eV photons (the peak of the RG spectrum) to be 300 GeV, while the cutoff energy of the best fitting electron spectrum is 3.2 GeV (Abdo et al., 2010a). Thus VERITAS gives no constraints on the leptonic model. So we focus our attention on the hadronic

model.

For the hadronic model, using the Fermi-only confidence region map created with the χ^2 calculated with the modeled spectrum and Fermi's data points and ULs, the constraints on the proton spectrum are looser at the higher cutoff energies (E_{cp}) (see the broken lines in Fig. 5.8. The 95.4% and 99% regions do not narrow down as the cutoff energy increases). We can improve this with the UL that VERITAS calculated. The UL given by the disp method is more confining (lower energy, lower UL value: see Fig. 5.7) than that given by the standard method, so we use the UL found with the disp method. We calculated χ^2 values for various values of the fitting parameters (spectral index s_p and cutoff energy E_{cp}) at the decorrelation energy (1.6 TeV), using the flux at the energy. Then we added these χ^2 values to the Fermi-only confidence region map created with Fermi's data points and the ULs. Originally, with Fermi's ULs only, the higher cutoff energy (E_{cp}) regions were very loosely constrained, but the VERITAS result successfully gave restrictions to the original confidence regions, narrowing down the 99% and the 95.4% confidence level contours (Compare the broken lines and the corresponding solid lines in Fig. 5.8). The VERITAS result excludes the proton spectrum extension to very high energies.

5.6 Physical profile of the nova

5.6.1 Time Evolution of the Nova

In this section, we roughly estimate the temporal evolution of the nova. The nova outburst of V407 was first optically observed on Mar.10.8 UT. The ANS collaboration in northern Italy obtained H α spectra beginning on Mar.13 (+2.3d after the optical nova detection: Fig. 5.10), and measured the FWHM of the broad component of each spectrum (Munari et al., 2010). By treating the broad component

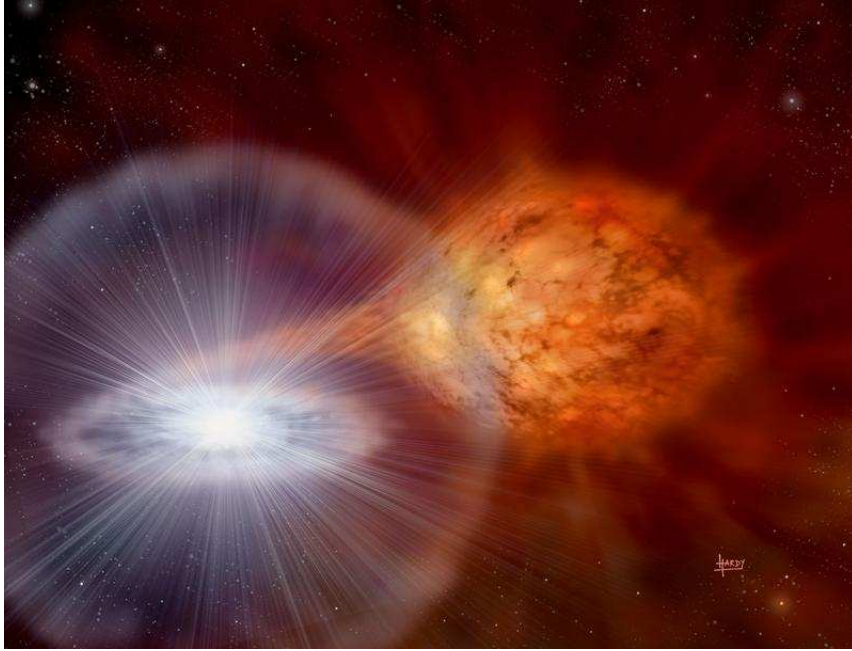


Figure 5.9: Artist's image of the nova of RS Ophiuchi in 1985. Credit: David Hardy/PPARC

of the spectral peaks as a result of the Doppler effect, we can see the temporal evolution on the ejecta velocity. The fitting formula they found for the FWHM (km/s) is as follows:

$$FWHM = 4320 - 5440 \log t + 2635(\log t)^2 - 460(\log t)^3 \quad (5.1)$$

where t is the time in days after the first detection of the nova (Mar.10.8 UT). The error on the expansion velocity was less than 10%.

The speed of sound in an ideal gas is $c_{ideal} = \sqrt{\gamma kT/m}$, where k is the Boltzmann constant, T is the temperature, and m is the mass of a molecule in kg. With this equation, we made a very rough estimation of the speed of sound near the RG, assuming that the gas in the vicinity of the RG is made of hydrogen molecules. For the gas temperature, we adopted $T = 700\text{K}$ (Munari et al., 1990), and assumed that $\gamma = 7/5$ because hydrogen molecule is di-atomic. Then the estimated speed is $\sim 2\text{km/s}$, which is much lower than the ejecta velocities in eq. (5.1) and in Fig. 5.11,

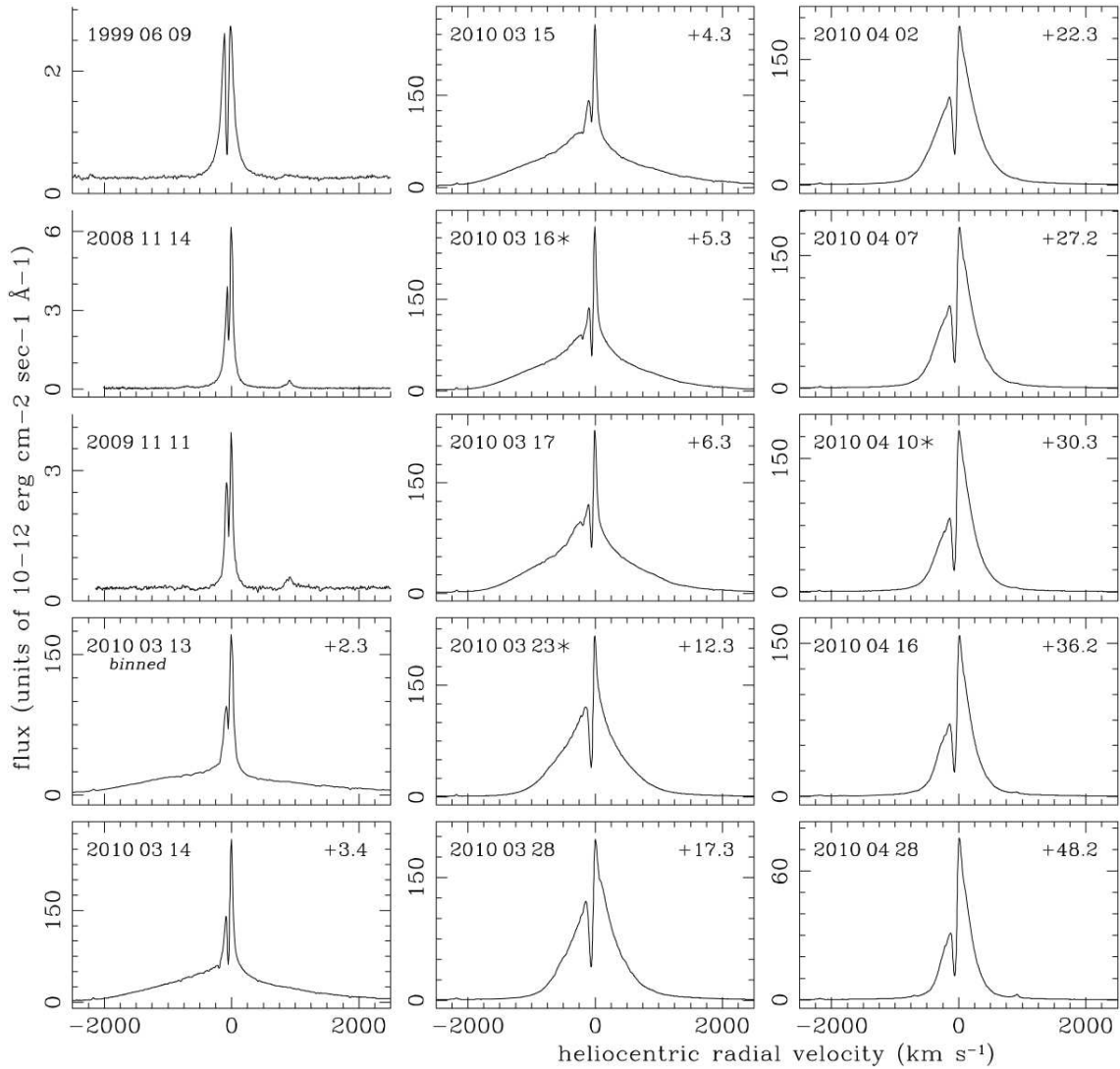


Figure 5.10: Temporal profile of the H α spectra of V407 Cygni that the ANS collaboration obtained. The upper three plots in the left column are those in the quiescent phase (in the year 1999, 2008 and 2009), and the rest shows the profile after the nova explosion (20100313=+2.3d and thereafter). Taken from Munari et al. (2010).

so we can conclude that the nova caused a shock wave.

This relation was fitted to the data taken on Mar.13 (+2.3d after the optical detection of the nova) and thereafter, and we must infer the velocity before that period. We have two options for the velocity profile of the nova between Mar.10

and 12: 1) The nova shell incurred no deceleration (experienced free expansion), with the assumption that the mass collected by the nova shell during this period was small (free expansion model). 2) Simply apply eq. (5.1) for the velocity before Mar.13 (extrapolation model). The earliest data for the $H\alpha$ spectrum is from +2.3d (see Fig. 5.10), and eq. (5.1) gives the nova velocity at that point to be 2675 km/s. We have no information about the nova velocity before +2.3d, but the deceleration should have begun sometime between the onset of the nova and +2.3d.

RS Ophiuchi (RS Oph) is a recurrent nova known to have similar characteristics with V407 Cygni (Orlando & Drake, 2011). Its He/N spectrum is close to that of V407 Cygni (Munari et al., 2010), which implies that the temporal evolution of its nova velocity is comparable with that of V407 Cygni. Sokoloski et al. (2006) studied the X-ray spectra of the 2006 nova outburst of RS Oph, and inferred when the deceleration phase for the blast wave had begun. The data they used were taken on +3d and thereafter. With the assumption that the X-rays are from the heated material of the shock wave, they related the shock velocity and the temperature of the shock. With the equation $u \propto T^{1/2}$, they surmised that the speed of the shock decreased as $t^{-1/3}$. Using this equation and the initial velocity of 3500 km/s, they concluded that the deceleration began on +1.7d. The velocity profile observed at early times for RS Oph lies between the two models calculated for V407 Cyg. Thus, it is reasonable to use those two models as bounds on the true velocity profile of V407 Cyg.

Orlando & Drake (2011) simulated the nova of V407 Cygni with various physical models, and some of the models could reproduce the observed X-ray light curve quite well. So, besides the equation for the velocity above, we adopt some physical parameters of the binary (RG size, binary separation) from Orlando & Drake (2011, see Table 5.2).

As we have seen, one component of V407 Cygni is a WD. Generally, it is known that a radius of a WD is $\sim 0.01 \times R_{\odot}$, and its mass is $\sim 1 \times M_{\odot}$. The maximum mass with which a star can exist as a WD is called the “Chandrasekhar limit,” and its value is estimated to be $\sim 1.4 \times M_{\odot}$. Munari et al. (1990) estimated the binary separation for some typical WD masses ($0.5 \times M_{\odot}$, $1 \times M_{\odot}$, and $1.4 \times M_{\odot}$) with the RG mass $\sim 1 \times M_{\odot}$ (Allen, 1976). Orlando & Drake (2011) adopted a WD mass of $1 \times M_{\odot}$, and the corresponding binary separation they calculated is 15.5 AU.

Parameter	Value
RG radius	$R_{cs} = 2.2 \text{ AU}$
RG mass	$1 \times M_{\odot}$
WD mass	$1 \times M_{\odot}$
Binary separation	$a = 15.5 \text{ AU}$

Table 5.2: Parameter set Orlando & Drake (2011) used for the simulations.

With these three pieces of information (the velocity, the binary separation, and the RG radius), we calculated the velocity profile and the position of the nova shell on a line connecting the centers of the WD and the RG for the two models (see Fig. 5.11 and Fig. 5.12).

Abdo et al. (2010a) argue that the gamma-rays are primarily generated by the nova shell when approaching the RG. Their main points are: (i) The gamma-ray flux reaches its maximum within 3 days from the optical nova detection. This can be explained as a result of the increasing efficiency for p-p interaction and the increasing area of the nova shell surface. (ii) The gamma-ray flux declines ~ 5 days after the onset, and it is due to the deceleration of the nova. The blue line in Fig. 5.11 indicates the period of the VERITAS observation. According to this plot,

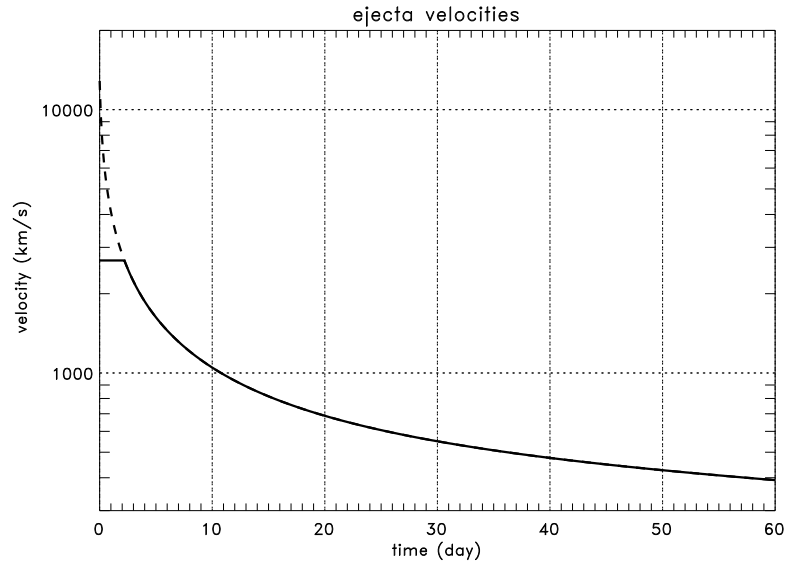


Figure 5.11: Velocity profile of the nova shell. For the period between +0d and +2.3d, the solid line is the “free expansion model,” and the broken line is the “extrapolation model.”

in both models, the VERITAS observation was carried out when the nova shell was approaching the RG.

The X-ray light curve of the nova on V407 Cygni shows a sharp rising of the emission during +15d \sim +24d, and a plateau between +24d and +40d (although there is a peak at \sim +31d. see Fig. 5.3). Orlando & Drake (2011), after their simulations, conclude that the blast wave is blocked by the RG, and converges to the back side of it. This conversion of the blast creates the hot and dense shock plasma behind the RG, and this is where most of the X-rays are generated. Fig. 5.11 shows that the nova shell reaches the RG surface at \sim +15d using the extrapolation model and \sim +21d using the free expansion model. The nova shell reaches the far end of the RG at \sim +26d using the extrapolation model and \sim +34d using the free expansion model. Comparing the actual X-ray light curve and our two models, the extrapolation model fits better but the free expansion model also is acceptable.

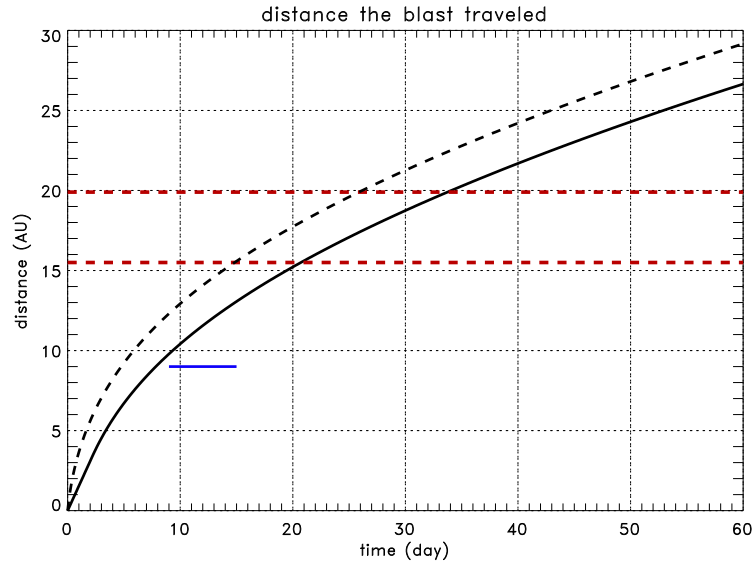


Figure 5.12: Position of the nova shell on the line between the WD center and the RG center by time. The solid line is the “free expansion model,” and the broken line is the “extrapolation model.” The lower red line corresponds to the front face of the RG (15.5 AU from the WD surface), and the upper red line is the rear end of the RG (19.9 AU from the WD surface). The blue horizontal line indicates the period in which VERITAS observed V407 Cygni (Mar. 19-26: +9d \sim +16d).

The actual profile of the nova is likely to be somewhere between these two models.

5.6.2 Magnetic Fields in the Binary

Bode & Kahn (1985) calculated the magnetic field strength by assuming the equipartition of the magnetic energy density, $B^2/8\pi$, and the thermal energy density, ρkT , in the RG wind (ρ is the number density of gas molecules, k is the Boltzmann constant, and T is the temperature of the gas):

$$B = (8\pi\rho kT)^{\frac{1}{2}} \quad (5.4)$$

In the shock, if the gas is mono atomic, the gas densities behind and ahead of the shock front have the relation $\rho_2/\rho_1 = 4$ (ρ_2 is the density behind the shock, and ρ_1 is the density ahead of the shock. see Sec. 4.1). This means that the gas density

inside the shock front is four times larger than that outside of the shock. Applying this to eq. (5.4), we have the following relation (Abdo et al., 2010a):

$$B = (32\pi\rho kT)^{\frac{1}{2}} \quad (5.5)$$

As noted in Bode & Kahn (1985), the RG gas density is proportional to R^{-2} , where R is the distance from the center of the RG. For some simulation models, Orlando & Drake (2011) assumed the existence of what they call CDE (circumbinary density enhancement), the enhancement of the gas density in the binary orbital plane, in addition to the simple R^{-2} factor. This corresponds to the accretion disk of the binary, the existence of which seems physically reasonable. Among the models of Orlando & Drake (2011), those with CDE best simulated the observed X-ray light curve. The gas mass density of their best fitting model is written in the following form:

$$\rho_{mass} = \rho_W \left(\frac{R_{CS}}{R} \right)^2 + \rho_{cde} \exp[-(x/l_1)^2 - (y/l_2)^2 - (z/l_3)^2] \quad (5.6)$$

Note that ρ_{mass} is not the number density, but the mass density of the gas. Now, $\rho_W = \mu m_H n_W$ is the wind mass density of the RG near its surface, where $\mu = 1.3$ is the mean atomic mass for cosmic abundances, m_H is the hydrogen atom mass, and $R_{CS} = 2.2\text{AU}$ is the RG radius. Likewise, $\rho_{cde} = \mu m_H n_{cde}$ is the mean atomic mass for the CDE near the RG. $n_W = 10^7\text{cm}^{-3}$ and $n_{cde} = 2 \times 10^6\text{cm}^{-3}$ are the number density of the gas molecules for the R^{-2} component and the CDE, respectively. Finally, the scaling factors for CDE are defined as $(l_1, l_2, l_3) = (53 \text{ AU}, 53 \text{ AU}, 27 \text{ AU})$.

We convert the equation above (mass density) to the number density of gas molecules as:

$$\rho = n_W \left(\frac{R_{CS}}{R} \right)^2 + n_{cde} \exp[-(x/l_1)^2 - (y/l_2)^2 - (z/l_3)^2] \quad (5.7)$$

where $(n_W, n_{cde}, l_1, l_2, l_3) = (10^7 \text{ cm}^{-3}, 2 \times 10^6 \text{ cm}^{-3}, 53 \text{ AU}, 53 \text{ AU}, 27 \text{ AU})$.

With eq. (5.5), (5.7) and our calculated position of the nova shell versus time (see Sec. 5.6.1), we can calculate the magnetic field strength (in G) at the shock front versus time (Fig. 5.13). For the RG gas temperature in eq. (5.5), we used $T = 700\text{K}$ (Munari et al., 1990). This shows that the magnetic field increases as the nova approaches the RG surface, which is a simple outcome of the fact that it is proportional to $(\text{gas density})^{\frac{1}{2}}$ and the gas becomes denser as it gets closer to the RG.

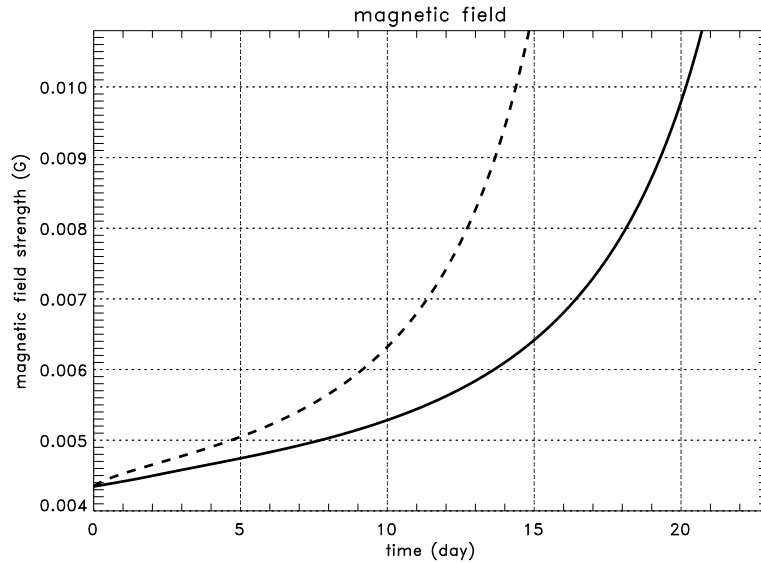


Figure 5.13: The time evolution of the magnetic field strength (in G) at the shock front in time. The solid line is the “free expansion model,” and the broken line is the “extrapolation model.” The upper limit of the vertical axis corresponds to the magnetic field strength at the front face of the RG; the shock reaches the RG at the time when the curve touches the upper edge for both models.

5.6.3 Particle Acceleration

Eq. (4.39), $E_{max} = zeBU^2t$, where U is the shock velocity, implies that the maximum energy that a particle can obtain in shock acceleration per time is proportional to the magnetic field and the square of the shock velocity. If B and U change over time, this equation can be re-written as $E_{max} = \int_0^t zeB(t)U^2(t)dt$. With this equation, we estimate the maximum energy of accelerated particles E_{max} , assuming that the particles are continuously accelerated without energy loss until they hit the RG surface, and that the shock wave travels directly from the WD to the RG. Fig. 5.14 is the time profile of E_{max} for the two models. We saw that the nova reaches the RG at $\sim +21$ d for the free expansion model, and at $\sim +16$ d for the extrapolation model (Fig. 5.12). Fig. 5.14 shows that the maximum particle energy when it reaches the RG is ~ 1.7 TeV for the free expansion model, and ~ 2.8 TeV for the extrapolation model. This plot shows that the acceleration efficiency drops steeply after +3d to +5d, due to the deceleration of the nova shell.

According to this plot, on the first day of VERITAS observation of V407 Cygni, $E_{max} \sim 1.4$ TeV for the free expansion model and ~ 3.0 TeV for the extrapolation model. On the last day, it was ~ 1.7 TeV and ~ 3.4 TeV, respectively, for the two models. The “decorrelation energy” (see Sec. 5.4 and Sec. 5.5) at which we imposed the flux upper limit was 1.63 TeV for the disp method and 1.77 TeV for the standard method. Unfortunately, the energy threshold obtained with VERITAS was quite high due to the large zenith angle of the observation (see Table 5.1). The threshold is close to the maximum particle energy expected from standard shock acceleration theory applied to models of the motion of the shock wave through the binary system. Thus, if the magnetic field we calculated and the nova blast velocity we assumed were correct, no strong constraints can be obtained from the VERITAS data. Future VHE observations of another nova obtained with a lower energy

threshold, due to improved instrumentation or a more favorable zenith angle, would be of interest to constrain the acceleration of very high energy particles in novae.

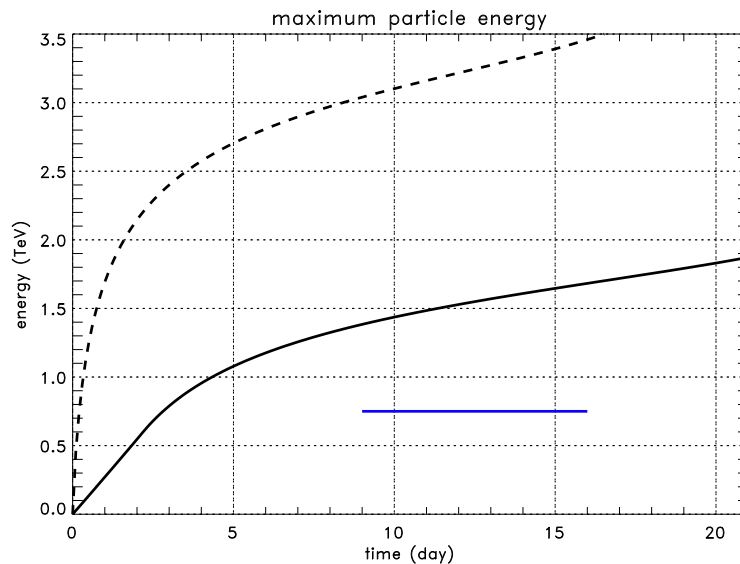


Figure 5.14: The profile of the maximum energy a particle can obtain in the nova shell. The solid line is the “free expansion model,” and the broken line is the “extrapolation model.” The blue line indicates the period of the VERITAS observation of V407 Cygni. For the “free expansion model,” the nova reaches the RG at $\sim +21$ d. For the “extrapolation model,” the nova reaches the RG at $\sim +16$ d.

Now suppose that the maximum proton energy we calculated for the two models (~ 1.7 TeV and ~ 3.4 TeV) are the cutoff energy, E_{cp} , of the analytic form used for the gamma-ray spectrum, and let us estimate how well the spectra fit the data. Fixing $E_{cp} = 1.7$ TeV or 3.4 TeV, the best fitting spectral index is 2.7 in both cases. The photon spectral energy distributions obtained with these parameters are shown in Fig. 5.15. From Fig. 5.7, we see that these parameter sets are inside the 90% confidence level contour.

As noted, the energy that a particle gains in unit time is proportional to the magnetic field and the squared velocity of the nova blast. Our calculation of the magnetic field strength is based on the best fitting gas density model from Orlando

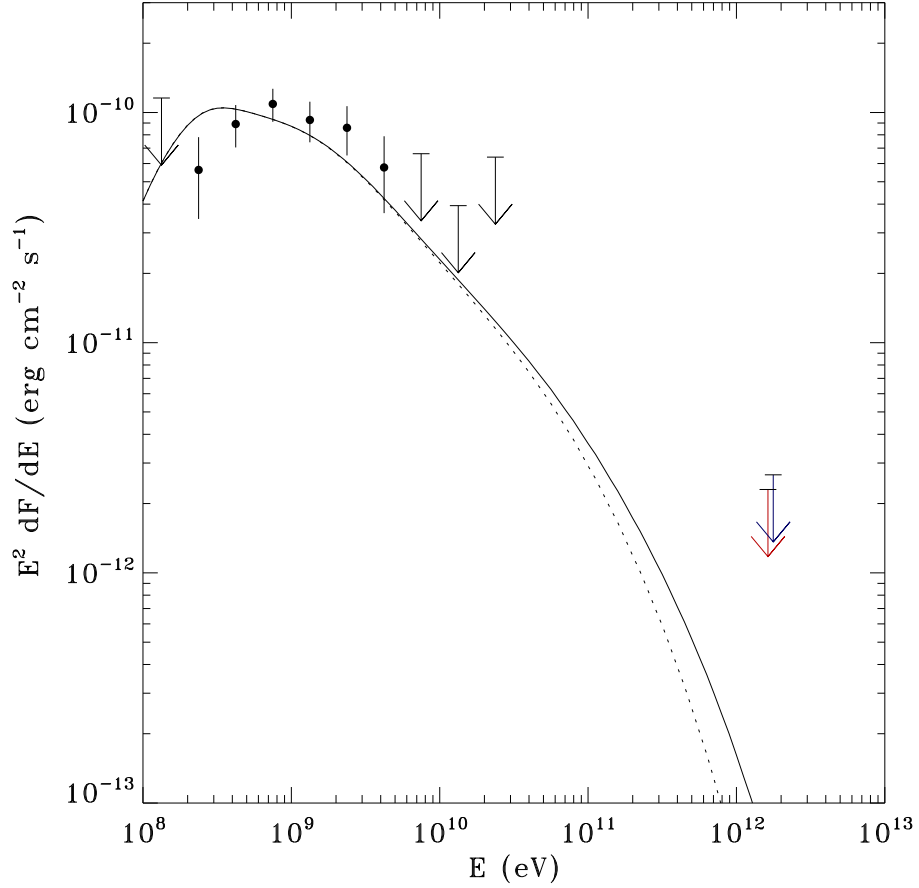


Figure 5.15: The photon energy spectra for the best fitting proton spectra parameters, with the protons’ cutoff energies set at the maximum obtainable energies for the two velocity models: the solid line is the case for the “extrapolation model,” $(s_p, \log(E_{cp})) \sim (2.7, 3.5)$, and the dotted line is the case for the “free expansion model,” $(s_p, \log(E_{cp})) \sim (2.7, 3.2)$.

& Drake (2011). However, the gas density near the WD surface that Fermi-LAT assumed is about one order of magnitude higher than our model (Munari et al., 2010), and accordingly the magnetic field near the WD surface is 0.03G, which is much higher than our calculation for the same position (~ 0.045 G). This magnetic field will result in a higher proton energy, as well as different profiles of the nova blast velocity. Moreover, with the future upgrade of VERITAS, the energy threshold

can be below 200 GeV (Kieda, 2011), and so VERITAS may be sensitive enough to detect gamma-rays from novae like V407 Cygni in the future.

CHAPTER 6

MGRO J1908+06

6.1 Observational history and features

The observational history of our next target, MGRO J1908+06, is quite new; it was recently found by the Milagro Gamma-Ray Observatory. Milagro was a very high-energy telescope system located in New Mexico, composed of a large water pool and 723 PMTs, which detected Cherenkov radiation from particle showers passing through the water pool triggered by primary photons from gamma-ray sources. It was used to survey TeV gamma-ray sources in the Northern Hemisphere, and MGRO J1908+06 was one of the objects that the Milagro collaboration reported as their new findings in 2007 (See Fig. 6.1) (Abdo et al., 2007). The new TeV source MGRO J1908+06 was observed at a median energy of 20 TeV (Abdo et al., 2010b), with a significance of 8.3σ and a flux of 80% of the Crab flux (Abdo et al., 2007). Its angular size is not yet certain, but has an upper limit of 2.6° . In the subsequent years other ground-based telescopes, including HESS (High Energy Stereoscopic System) and VERITAS, imaged and measured the spectrum of MGRO J1908+06 in the range of 0.3-20 TeV (Aharonian et al., 2009; Ward, 2008).

HESS performed a Galactic Plane survey of the central region of the Milky way during 2005-2007, and its first detection of HESS J1908+063 was made in this period (Aharonian et al., 2009). The angular size of the HESS detection is $\sigma = 0.34^\circ$, and its centroid position and flux were in good agreement with MGRO J1908+06 (See Fig. 6.2). Thus they concluded that these two sources are identical (Aharonian et al., 2009). Our work hereafter is aimed on examining how the gamma-ray emission from MGRO J1908+06 is generated.

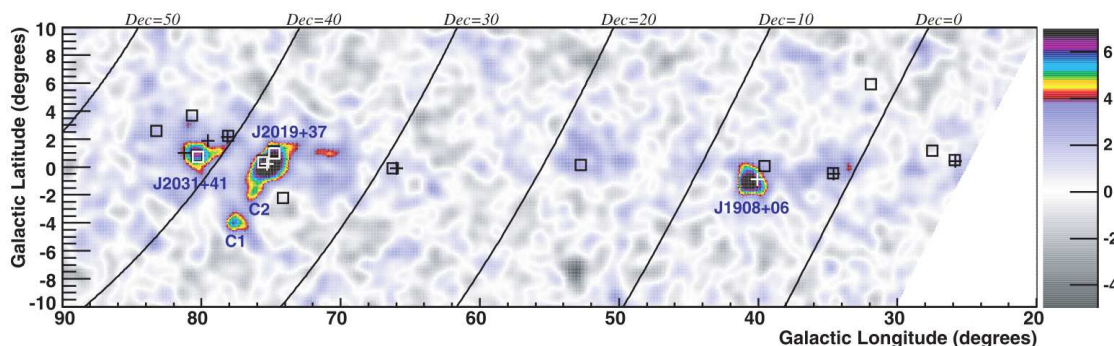


Figure 6.1: The Significance map taken from the Milagro paper (Abdo et al., 2007). Boxes and crosses are the locations of the GeV sources in the third EGRET catalog (3EG). J1908+06 is located at the Galactic Longitude of $\sim 40^\circ$ with a significance of 8.3σ .

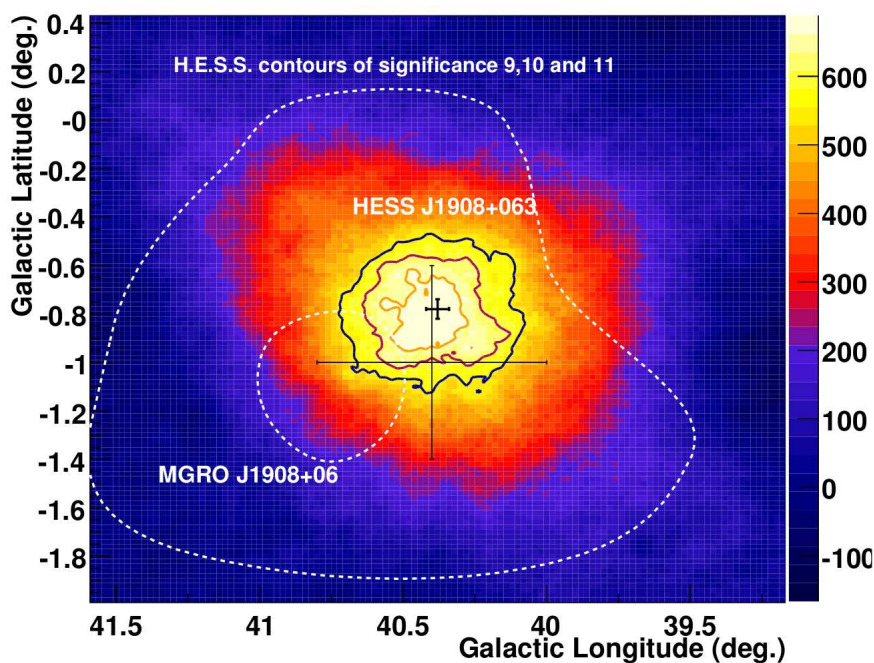


Figure 6.2: The Excess map taken from the HESS paper (Aharonian et al., 2009). The three colored contours correspond to the pre-trial significance level 9σ , 10σ and 11σ . The source extent found with Milagro is shown by the dotted white lines; 8σ contour (inner) and 5σ contour (outer). The crosses are the best HESS and Milagro fitted positions, of which the error bars are the summation of the statistical and systematic errors.

6.2 Supernova Remnants, Pulsars, and Pulsar Wind Nebulae

MGRO J1908+06 lies on the sky near a supernova remnant and a pulsar, that may be the source of a pulsar wind nebula. In this section, we provide some background material on these classes of objects that will be used in our discussion of the physical nature of the TeV emission later on. The information in Sec. 6.2.1 and Sec. 6.2.2 is from Kifune (2004), Longair (2011), Melia (2009), Osaki (1996), and Takahara (2002).

6.2.1 Supernovae and Supernova Remnants

A Supernova explosion is an astrophysical phenomenon which happens as a result of the evolution of a heavy star. The energy source of a star is nuclear fusion that occurs in its core. A main sequence star shines using hydrogen as fuel, and helium is accumulated as the “ash” of the fusion process. When the hydrogen in the core region is burned out, hydrogen fusion mainly takes place in a thin shell that covers the core. As the helium core shrinks, its temperature increases, and when it goes above 10^8 K, the helium nuclei are ignited and they undergo the 3α process, producing carbon and oxygen.

If the star has a large enough mass, the fusion process proceeds with heavier nuclei until iron is generated in the core. Iron is the element that has the most stable nucleus, so nuclear fusion stops at this point. As a result, the core shrinks due to gravity, and its temperature reaches as high as 3×10^8 K. Then, “photo-disintegration” process occurs as follows, and iron is decomposed into helium and neutron; ${}^{56}\text{Fe} + \gamma \rightarrow 13{}^4\text{He} + 4\text{n} - 124.4\text{MeV}$. Because this process absorbs heat, the pressure in the core decreases, which leads to the further shrinking of the core at an accelerated pace.

Finally, the core implodes and experiences “gravitational collapse.” The density of the core becomes as high as that of a nucleus, as the protons of the core catch electrons and become neutrons. The shrinking process stops when the nuclear force takes effect in the core. As the core shrinks to a very small volume, the outer layer undergoes free fall due to gravity, hits the core, and bounces back. This liberates a huge amount of gravitational potential energy. The liberated energy is mostly released in the form of neutrino emission, a part of which is absorbed by the outer shell, which is blown off. This process is called a “Supernova explosion.” Ejected mass from a supernova explosion is scattered around in the range of $\sim 10\text{pc}$, called a “Supernova Remnant (SNR).” Cosmic particles are accelerated due to the Fermi acceleration mechanism in SNRs, just as in nova explosions. The core of extreme density remains after supernova explosion as a neutron star. If its radius is smaller than the Schwarzschild radius, it becomes a black hole.

6.2.2 Pulsars

Pulsars were first discovered by Jocelyn Bell and Antony Hewish in 1967 (Hewish et al., 1968). They observed a radio pulse with a periodic time separation of 1.3373 Sec, the source of which is today called PSR B1919+21. Now, pulsars are identified as a neutron star rotating at a very high speed. As noted in the previous section, pulsars are generated as the core of a star that underwent a Supernova explosion. The extremely high rotational speed originates from conservation of angular momentum, as a result of the huge loss of moment of inertia in the collapse from the normal stars to the neutron star, typically with a mass as much as the solar mass and a radius of $\approx 10\text{ km}$. There are several types of pulsars and neutron stars. Here we are interested in radio pulsars.

Pulsars have a very strong magnetic field, and the magnetic field axis is usually not aligned to the rotational axis. A braking effect works on this rotation, due to the

magnetic fields rotating along with the neutron star. Due to moving magnetic fields with a velocity v , electric fields are induced with the intensity of $E = |\vec{v} \times \vec{B}| \approx R_0 \omega B$. Electrons are accelerated by the electric fields, and accelerated electrons emit gamma-rays. The emitted gamma-rays further create electron-positron pairs, and they generate secondary and ternary particles via synchrotron radiation and inverse Compton scattering. This flow of particles, the “pulsar wind,” collides with matter around the pulsar and a “pulsar wind nebula” (PWN) is created.

The energy source of a radio pulsar is the rotational energy of the neutron star which is written in the following form:

$$E = \frac{1}{2} I \omega^2$$

where I is the moment of inertia, and ω is the angular velocity. The decrease in rotational energy in time powers the radiation and production of winds of energetic particles;

$$\frac{dE}{dt} = I \dot{\omega}$$

Using the pulse period, P , and its first time derivative, \dot{P} , the approximate age of the pulsar can be inferred. The characteristic age τ of the pulsar is $\tau = P/2\dot{P}$.

6.2.3 Pulsar Wind Nebula

The rotation of magnetic field converts the rotational energy of a neutron star into electromagnetic energy, which produces an outflow of electrons and positrons. This relativistic flow of electrons and positrons is called a pulsar wind. The pulsar wind collides with surrounding material and a shock front is formed, at which particles are accelerated via Fermi acceleration mechanism, and these particles form a Pulsar Wind Nebula (PWN). The energetic particles generate very high energy gamma-rays (> 100 GeV) via inverse Compton scattering. Inverse Compton Scattering is a very important process in high energy astrophysics. When high energy

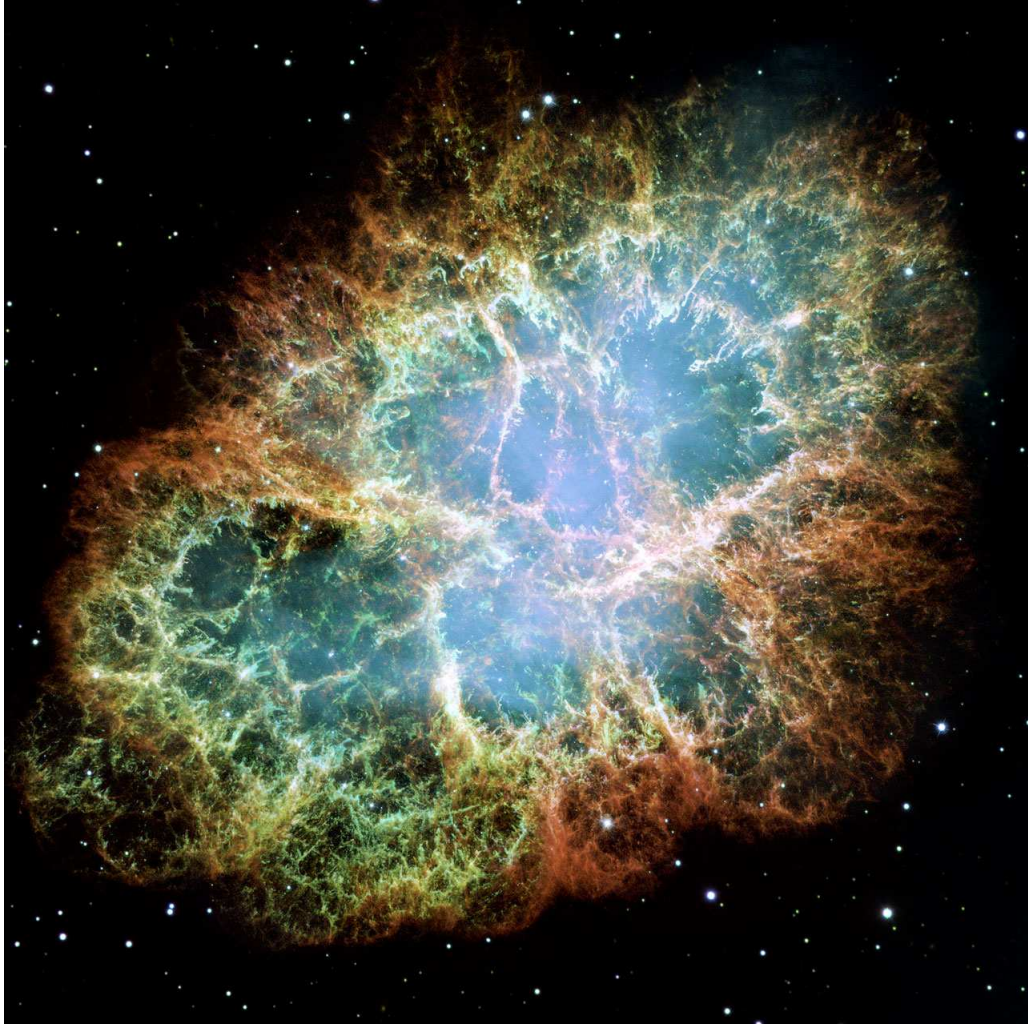


Figure 6.3: Hubble telescope image of the Crab nebula, known as the most representative supernova remnants. The supernova explosion at this was observed in 1054 AD by Japanese and Chinese observers. Credit: NASA, ESA and Allison Loll/Jeff Hester

electrons hit photons, the photons are scattered off and gain energy. Low energy photons from synchrotron radiation or CMB photons are the seed photons for this process. The energy of the scattered photon is $\varepsilon_{sc} \sim \gamma^2 \varepsilon_0$, where ε_0 is the energy of the soft photon and γ is the Lorentz factor.

Tanaka & Takahara (2010) modeled the spectral evolution of PWNe, assuming that the PWN is a uniform sphere that expands with a constant velocity, and the

energy injected by the pulsar is divided into magnetic fields energy and relativistic particle energy with a ratio that can vary with time. They assumed the injection spectrum of the relativistic particle obeys a broken power law, and simulated the time evolution of the magnetic fields by solving the relativistic magnetohydrodynamics (MHD) equations.

The Crab Nebula is the remnant of a Supernova explosion that occurred about one thousand years ago, and is today considered to be a standard of PWNe. Starting from the physical parameters of the Crab Nebula (rotational period, braking index, age etc.), they calculated a spectrum and compared it with the observed Crab spectrum (See Fig. 6.4). The model spectrum agrees well with the observed data.

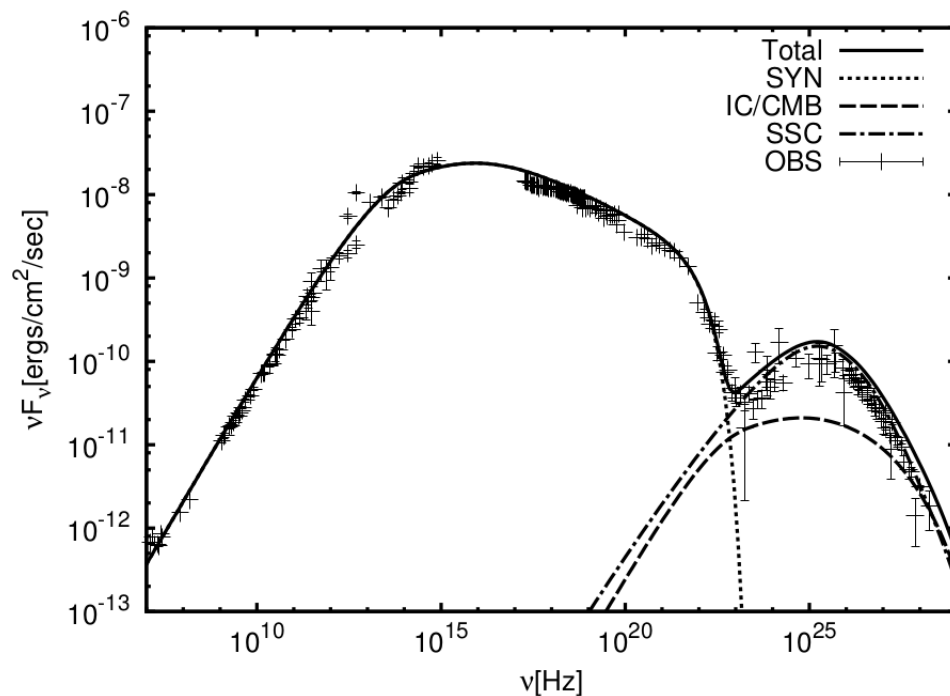


Figure 6.4: The current modeled spectrum of the Crab Nebula Taken from Tanaka & Takahara (2010). The total spectrum (Total) is the summation of the synchrotron radiation (SYN), Inverse Compton/Cosmic Background (CMB) and synchrotron self-Compton (SSC). The error points are the observed data, and those data match the simulated model (Total) very well.

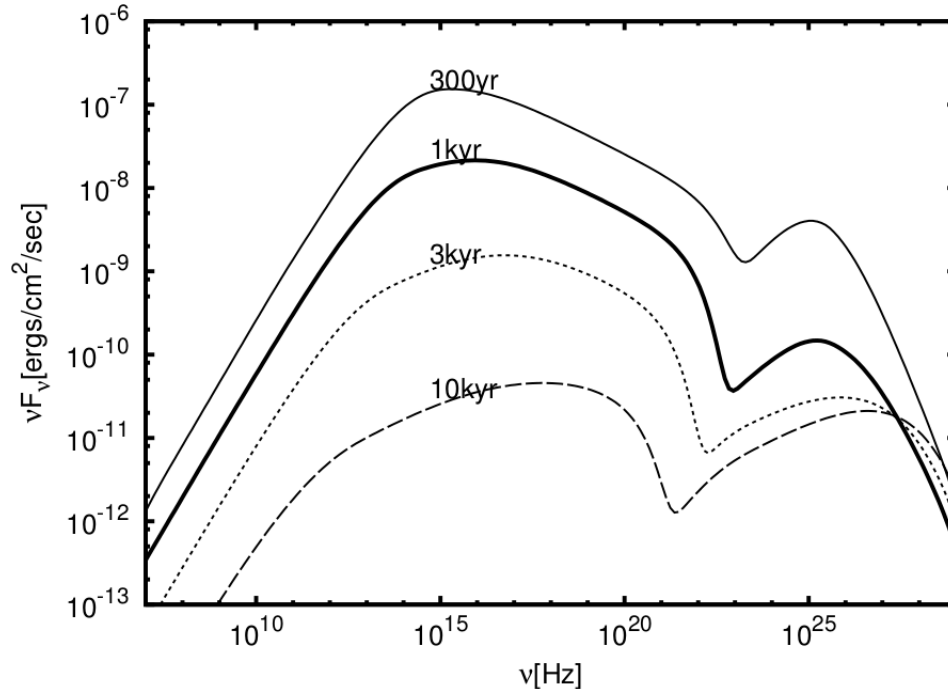


Figure 6.5: The spectral evolution of the Crab Nebula Tanaka & Takahara (2010) simulated. The thick solid line (the spectrum of the Crab at 1kyr old) is the current one. Taken from Tanaka & Takahara (2010).

There are two peaks in the spectrum. The one at the lower energies is predominantly from the synchrotron radiation due to motion of energetic particles in the magnetic field inside the PWN. The one at high energies is from the Inverse Compton scattering (IC). There are two different types of soft photon seed for IC emission: one is Cosmic Microwave Background photons (CMB) and the other is synchrotron photons, created by the synchrotron radiation of this PWN itself (this mechanism is called synchrotron self-Compton, SSC). The former factor is dominant for IC emissions especially at the frequency range $\nu < 10^{22}$ Hz.

Tanaka & Takahara (2010) calculated the evolution of the Crab Spectrum at 300 yr, 1 kyr (current), 3 kyr, and 10 kyr (See Fig. 6.5). This figure shows that both the synchrotron flux component (left, lower frequency) and the IC flux component (right, higher energy) decrease with the age, but the decrease of the IC component is

slower. According to their study, the SSC (synchrotron-self Compton) flux decreases as the decrease of the synchrotron flux (it is the natural outcome), but the decrease of the IC/CMB flux is slower than that. Tanaka & Takahara (2010) conclude that this is caused by the rapid decrease of the magnetic field. As a result, the flux ratio of gamma-rays to X-rays increases with age, and as a general trend, the sizes of the gamma-ray PWNe are generally larger than those of the X-ray PWNe.

Fig. 6.6 is a plot of $\log(L_\gamma/L_X)$ [erg/s] vs $\log(\text{Age})$ [yrs] for known PWNe using the data compiled in Kargaltsev & Pavlov (2010). We can see some positive correlation between these two parameters which means that as the pulsars get older, the relative strength of the X-ray luminosity in PWNe becomes smaller, compared with that of the gamma-ray luminosity. This corroborates the idea mentioned above. Fig. 6.7 is the plot of spectrum index vs $\log(\text{Age})$ [yrs] of PWNe, also using the data set of Kargaltsev & Pavlov (2010). At this map, we do not see a correlation between the parameters, and we cannot say anything on the trend between the spectral index and the age of PWNe from this plot.

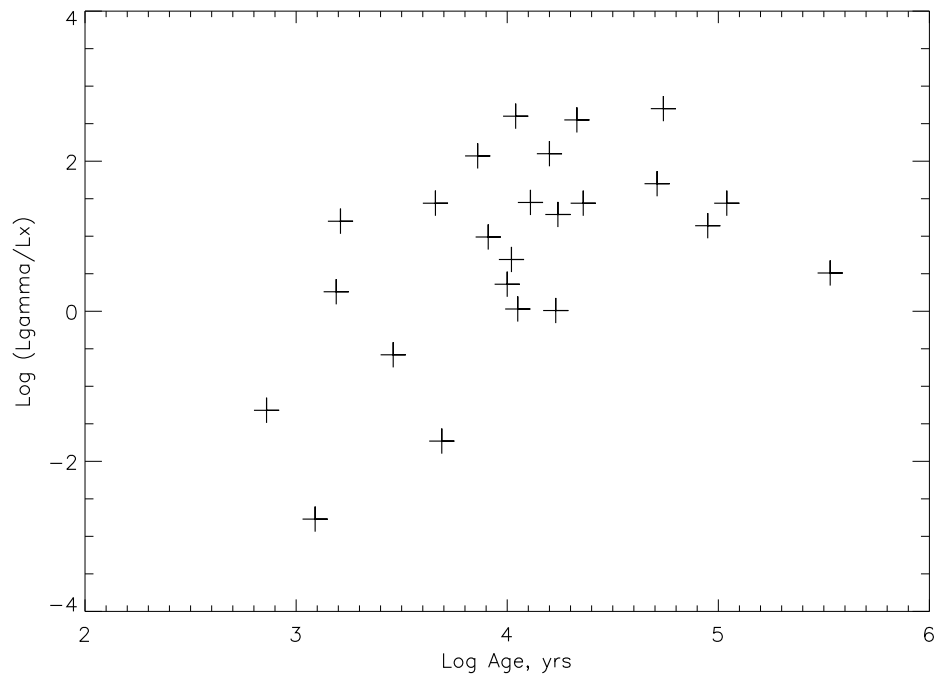


Figure 6.6: The relation between $\log(L_{\gamma}/L_X)$ and $\log(\text{Age})$ [yrs] of PWNe. A positive correlation between the two parameters can be observed. The data are from Kargaltsev & Pavlov (2010).

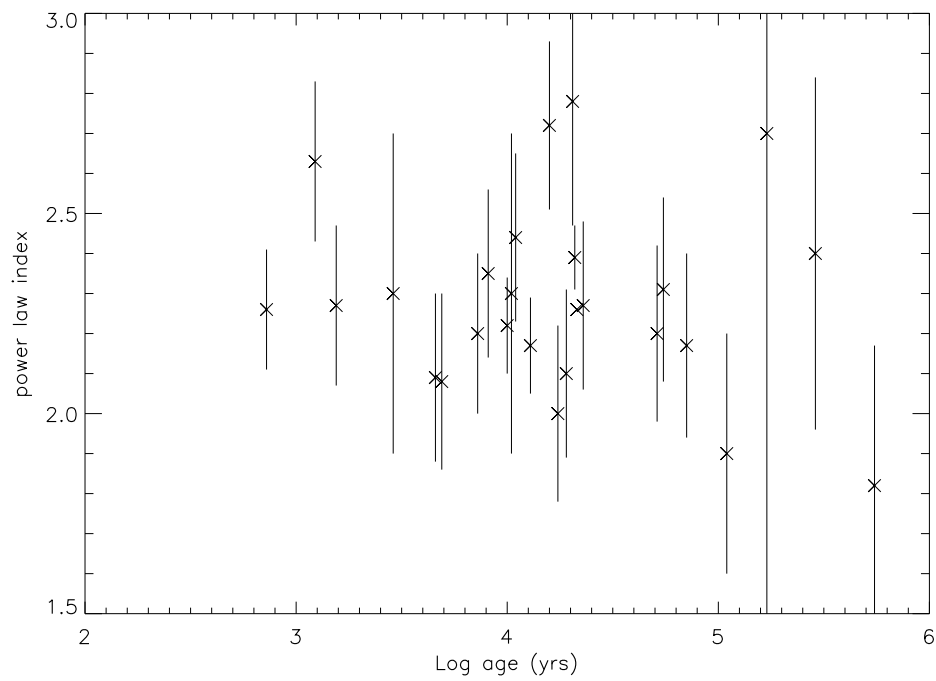


Figure 6.7: The relation between spectrum index and $\log(\text{Age})$ [yrs] of PWNe. The data are from Kargaltsev & Pavlov (2010).

6.3 Objects near the source

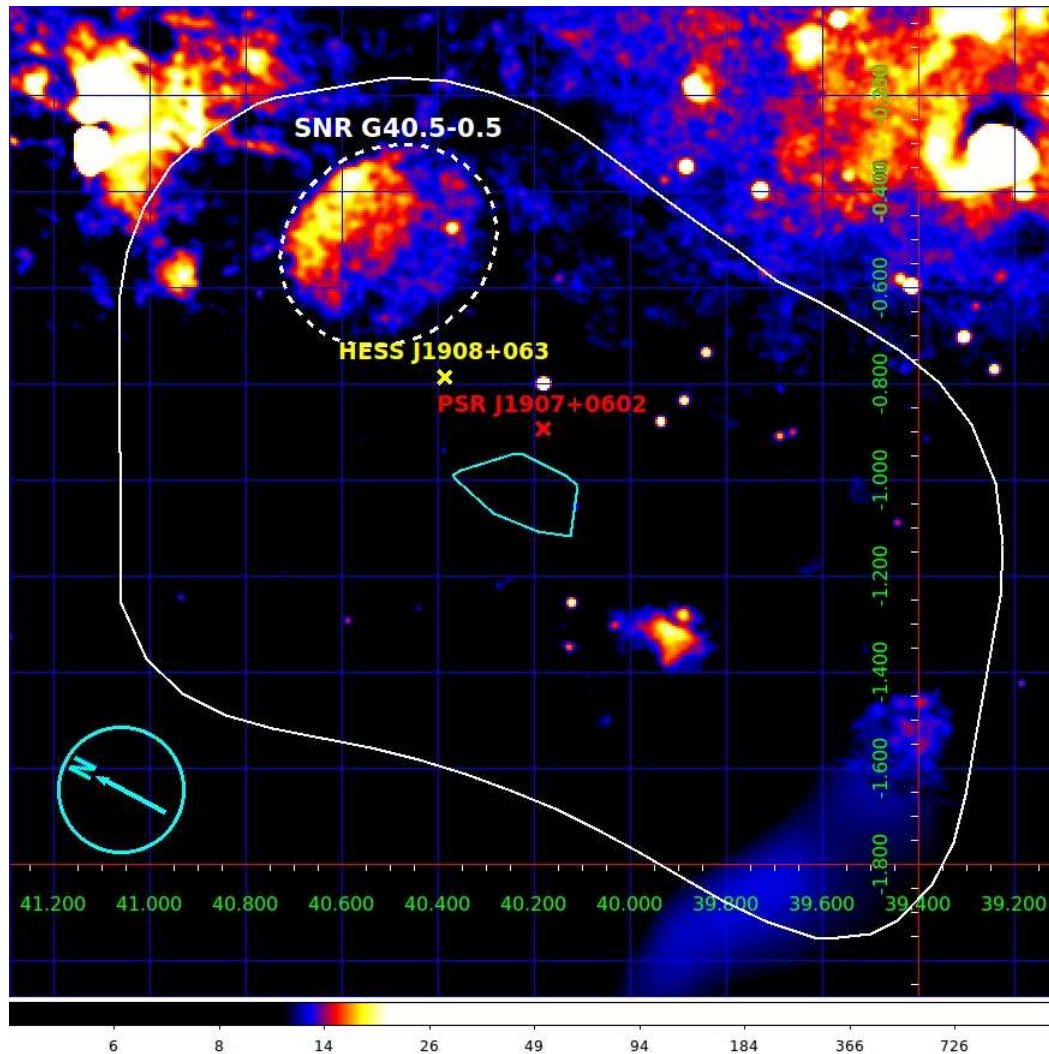


Figure 6.8: Very Large Array Galactic Plane Survey (VGPS) (Stil et al., 2006) map of the continuum radio emission near 1420 MHz, but excluding the H I line around the J1908+063 region. The small light blue line is the Milagro significance contour of the significance level $\sigma = 8$, and the large white line that encloses the entire region is the Milagro significance contour of $\sigma = 5$. The dashed ellipse shows SNR G40.5-0.5, following Yang et al. (2006). Its center is positioned at (RA, Dec)=(19:07:08.6, +06:29:53.0) (Abdo et al., 2010b), its size is $28' \times 24'$ (=25 pc) (Yang et al., 2006), and the angle of major axis in galactic coordinates is 31° . The light blue arrow inside a circle on the lower left corner indicates North for RA/Dec.

The HESS source (HESS J1908+063) lies between the supernova remnant SNR G40.5-0.5 and the pulsar PSR J1907+0602 (See Fig. 6.8). The Fermi-LAT collaboration used the Very Large Array Galactic Plane Survey (VGPS) (Stil et al., 2006) 1420 MHz continuum image to determine the position of the SNR (See Fig. 6.8). The SNR center they estimated is RA=286.79°, Dec=6.50° (Abdo et al., 2010b), and its angular diameter is 0.43° (Downes et al., 1980). Using the distances of the two objects from the earth, the separation between the SNR and the pulsar was estimated to be 28 pc. Assuming that the pulsar originated at the center of the SNR, with the characteristic age (see Sec. 6.2.1) of 19.5 kyr, the transverse velocity of the pulsar would be 1400 km/s (Abdo et al., 2010b), which is rather high as the transverse velocity of a pulsar, if it were born at the center of the SNR.

6.4 SNR G40.5-0.5

The supernova remnant that lies near MGRO J1908+06, SNR G40.5-0.5, was first detected as a radio source by Pauliny-Toth & Kellermann (1966), who gave it the name of NRAO 596. Since then several groups observed this object, but it was not until 1980 when G40.5-0.5 underwent a detailed investigation. Downes et al. (1980) observed SNR G40.5-0.5 with the Effelsberg 100-m telescope, and created 1720 MHz and 2700 MHz maps of the region around it (See Fig. 6.9). On their maps, a vivid shell-like structure can be seen in the northeast region, showing the typical morphology of a shell-type supernova remnant.

Downes et al. calculated the total flux densities of G40.5-0.5 to be 9.3 ± 1.3 Jy at 1720 MHz and 7.2 ± 0.5 Jy at 2700 MHz. Combining these results with the flux densities from Pauliny-Toth & Kellermann (1966), 12.3 ± 3.2 Jy at 750 MHz and 10.2 ± 1.6 Jy at 1400 MHz, they estimated a spectral index of $\alpha = 0.41 \pm 0.05$ for G40.5-0.5 (See Fig. 6.10). This found the non-thermal nature of G40.5-0.5 and the calculated index matches the mean spectral index of $\alpha = 0.45$ for supernova

remnants (Clark & Caswell, 1976). Thus Downes et al. concluded that G40.5-0.5 is a supernova remnant. From the Σ -D (surface brightness-linear diameter) relationship, Downes et al. estimated the distance of G40.5-0.5 to be 5.5-8.5 kpc, giving the size of 40-65 pc and the corresponding age of $2-4 \times 10^4$ yrs. This distance locates G40.5-0.5 near the inner edge of Sagittarius arm.

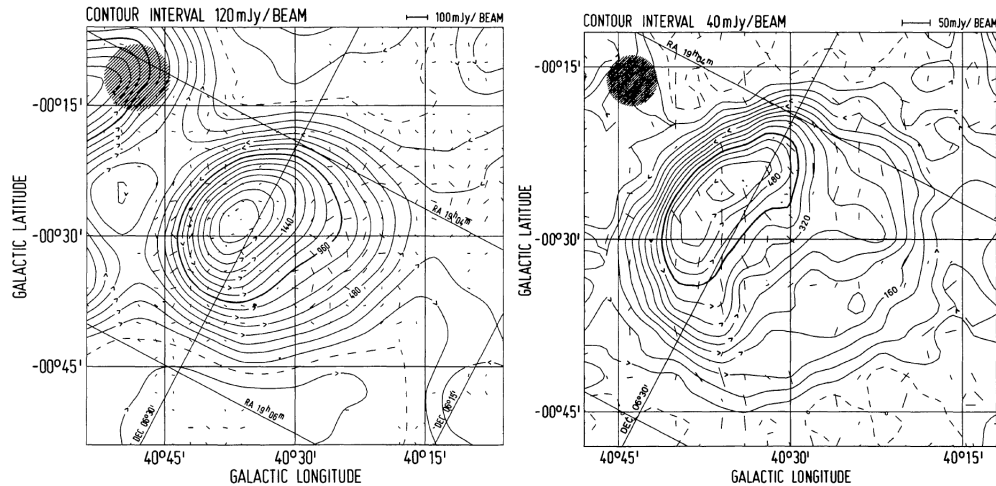


Figure 6.9: The 1720 MHz contour map of SNR G40.5-0.5, the contour interval of which is 120 mJy/beam (**Left**), and the 2700 MHz contour map of SNR G40.5-0.5, the contour interval of which is 40 mJy/beam (**Right**). Both are taken from Downes et al. (1980). The contours with anticlockwise arrows are around the peaks, and those with clockwise arrows are around the minima. The broken lines indicate the local zero level for SNR G40.5-0.5. The vectors represent the direction and the intensity of the linearly polarized component of the electric vectors.

Yang et al. (2006) observed G40.5-0.5 in the ^{12}CO ($J = 1 - 0$) line at 115.271 GHz with the 13.7 m millimeter-wave radio telescope of Purple Mountain Observatory at Tibet in Jan-May 2003 and investigated the gas distribution around the source. They created velocity fields maps along the E-W (East-West) and the N-S (North-South) directions, and three main velocity components were separated. One velocity component, $V = 45-65 \text{ km s}^{-1}$ (See Fig. 6.11), shows features that match the morphology of the continuum radio shell found by Downes et al. (1980). Inside

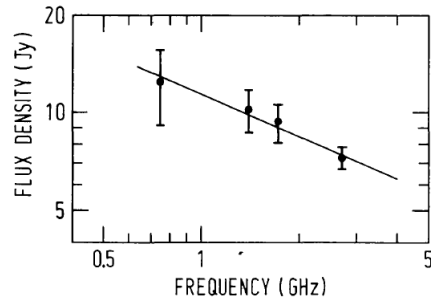


Figure 6.10: The spectrum of G40.5-0.5, fitted for the flux density data of Downes et al. (1980) and Pauliny-Toth & Kellermann (1966). Taken from Downes et al. (1980).

the region of continuum radio emission the molecular gas density is smaller, which suggests a shell structure of the source. From their position-velocity maps, Yang et al. (2006) found the velocity discontinuity at the outer radius of the shell, which suggests that there is a shock between the SNR and the gas medium surrounding it. The inferred velocity of the shocked gas is 10 km s^{-1} , and the estimated kinetic energy of the shocked gas is $(3-6) \times 10^{49}$ ergs, which amounts to 3-6 % of the total kinetic energy of a supernova explosion. Such shocks can accelerate particles to high energies via the Fermi Acceleration mechanism (See Chap.4). Using their identified velocity component $V = 55 \text{ km s}^{-1}$ and the rotation curve, Yang et al. (2006) estimated the source distance to be 3.4 kpc, and we will adopt this value in this work as the distance to G40.5-0.5.

Fig. 6.12 is an HI map in the 45-65 km/s velocity range, using data obtained in the VGPS. Some structures can be observed along the edge of G40.5-0.5 region, which possibly suggests the existence of high density gas at the boundary of the SNR.

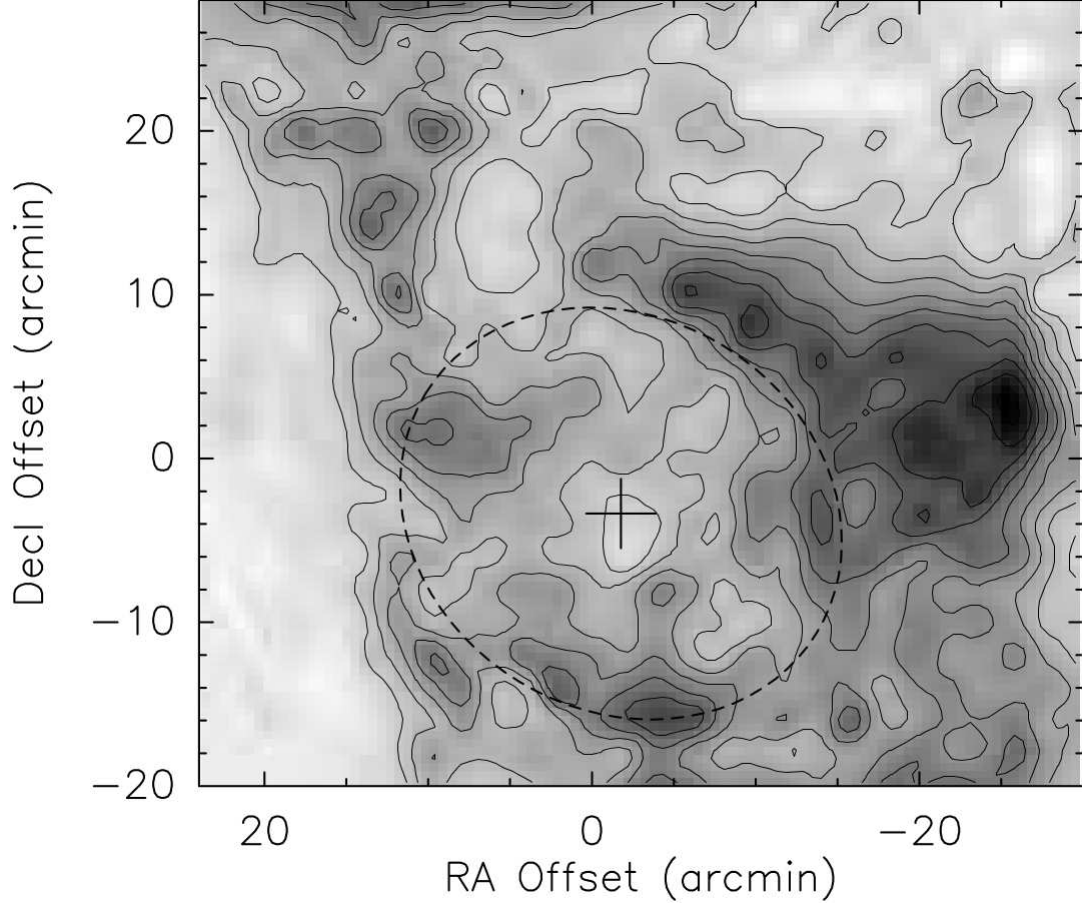


Figure 6.11: CO intensity map of the G40.5-0.5 region taken from Yang et al. (2006). The contours correspond to the intensity levels of the velocity component, $V_{LSR} = 45\text{-}65 \text{ km s}^{-1}$. This is the same ellipse plotted in Fig. 6.8. The ellipse is the shocked shell of the SNR ($28' \times 24'$), and the cross is its center.

Size of Shocked Shell	$28' \times 24'$ ($=25\text{pc}$)
Position Angle	121° (in the Galactic coordinates)
Distance	3.4 kpc
Gas Velocity	10 km s^{-1}
Shocked Mass	$(3\text{-}6) \times 10^4 M_\odot$
Momentum	$(3\text{-}6) \times 10^5 M_\odot \text{ km s}^{-1}$
Energy of Shocked Gas	$(3\text{-}6) \times 10^{49} \text{ erg}$

Table 6.1: Parameters of the shocked gas, taken from Yang et al. (2006). The information of the position angle was directly given by the author.

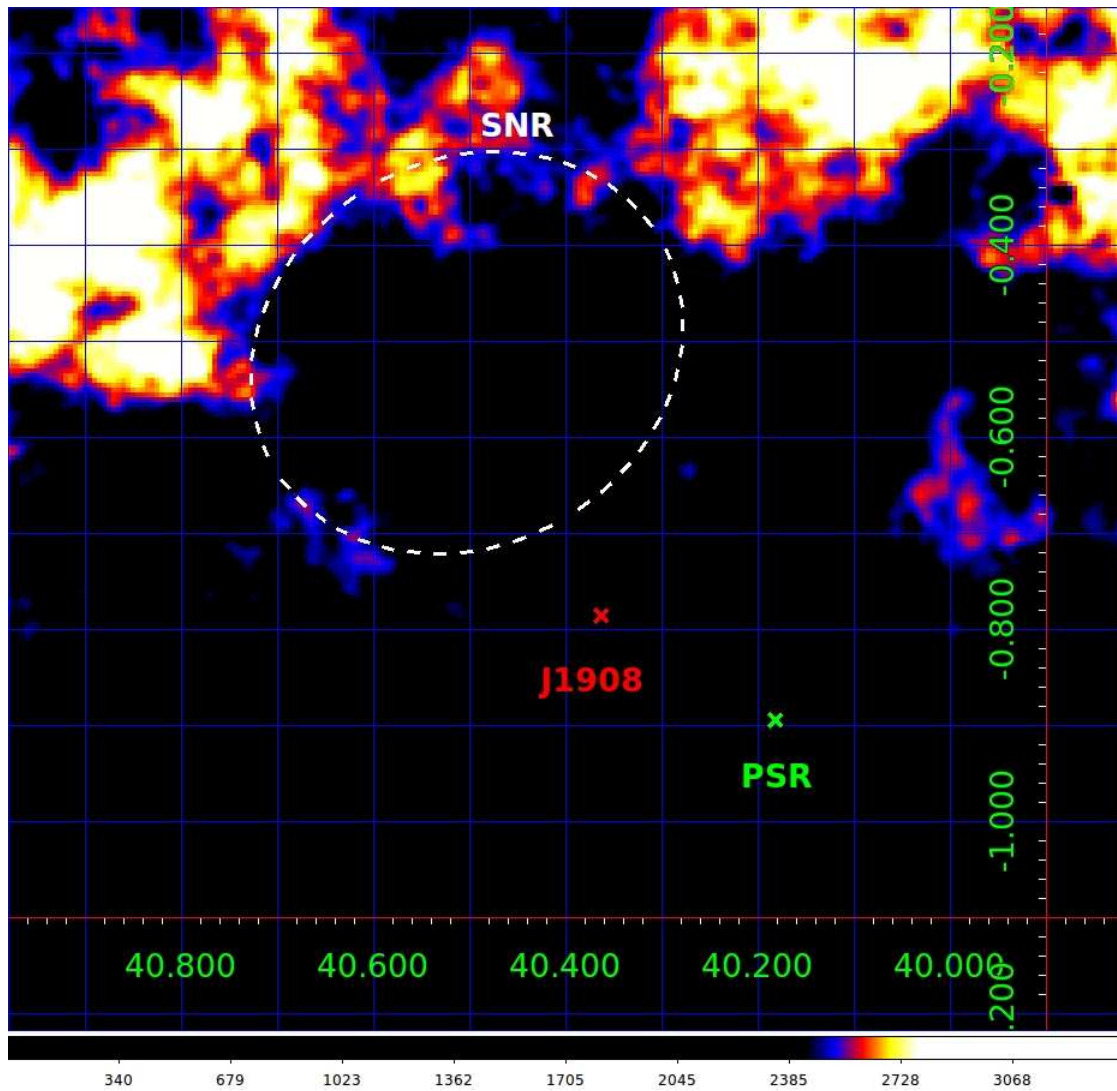


Figure 6.12: HI map of the Galactic plane around G40.5-0.5 in the velocity interval 45-65 km/s from the VGPS (Stil et al., 2006). Some structures can be seen along the rim of G40.5-0.5 area.

6.5 PSR J1907+0602

The Fermi-LAT collaboration detected 16 gamma-ray pulsars at energies above 300 MeV in blind searches with the Large Area Telescope (LAT), and one of them within the Milagro source region was designated as PSR J1907+0602 (Abdo et al., 2009). The pulsar has a characteristic age of about 20 kyr and a spin-down power of 3×10^{36} erg/s, see Table 6.2 for a full list of the derived pulsar parameters. Later they derived a timing solution with 14 months data allowing a more precise position determination (See Table 6.2) and study of the pulse profile. The gamma-ray pulse profile has two peaks (P1 and P2 in the five upper columns of Fig. 6.13.), and they did not find significant change in the shape of P1/P2 for different energies (Abdo et al., 2010b).

Abdo et al. (2009) also made follow-up observations at other wavelengths. With the Arecibo 305m radio telescope (located in Puerto Rico), they observed the timing position of PSR J1907+0602 for 55 minutes at a frequency of 1.51 GHz. The time-averaged flux density was $3.4 \mu\text{Jy}$. From the position and the dispersion measure, the distance was estimated to be 3.2 kpc with a nominal error of 20% (Abdo et al., 2010b). (Because of the interstellar medium, among the pulsed radio signals of the pulsar, the higher frequency components arrive faster to the earth than the lower frequency components. Dispersion measure (DM) is the column density of free electrons between the pulsar and the earth, and is estimated from the time delay of arrival for radio signals of different frequencies. The distance to a pulsar can be estimated using the pulsar's DM and a model of the distribution of the electrons in the galaxy.)

Pulsar name	PSR J1907+0602
Right ascension	286.98°
Declination	6.038°
Pulse period	106.6 ms
\dot{E}	$2.8 \times 10^{36} \text{ erg s}^{-1}$
Surface magnetic field	$3.1 \times 10^{12} \text{ G}$
Characteristic age	19.5 kyr
Dispersion measure (DM)	$82.1 \pm 1.1 \text{ cm}^{-3} \text{ pc}$
Distance	3.2 kpc

Table 6.2: Parameters of PSR J1907+0602, taken from Abdo et al. (2010b).

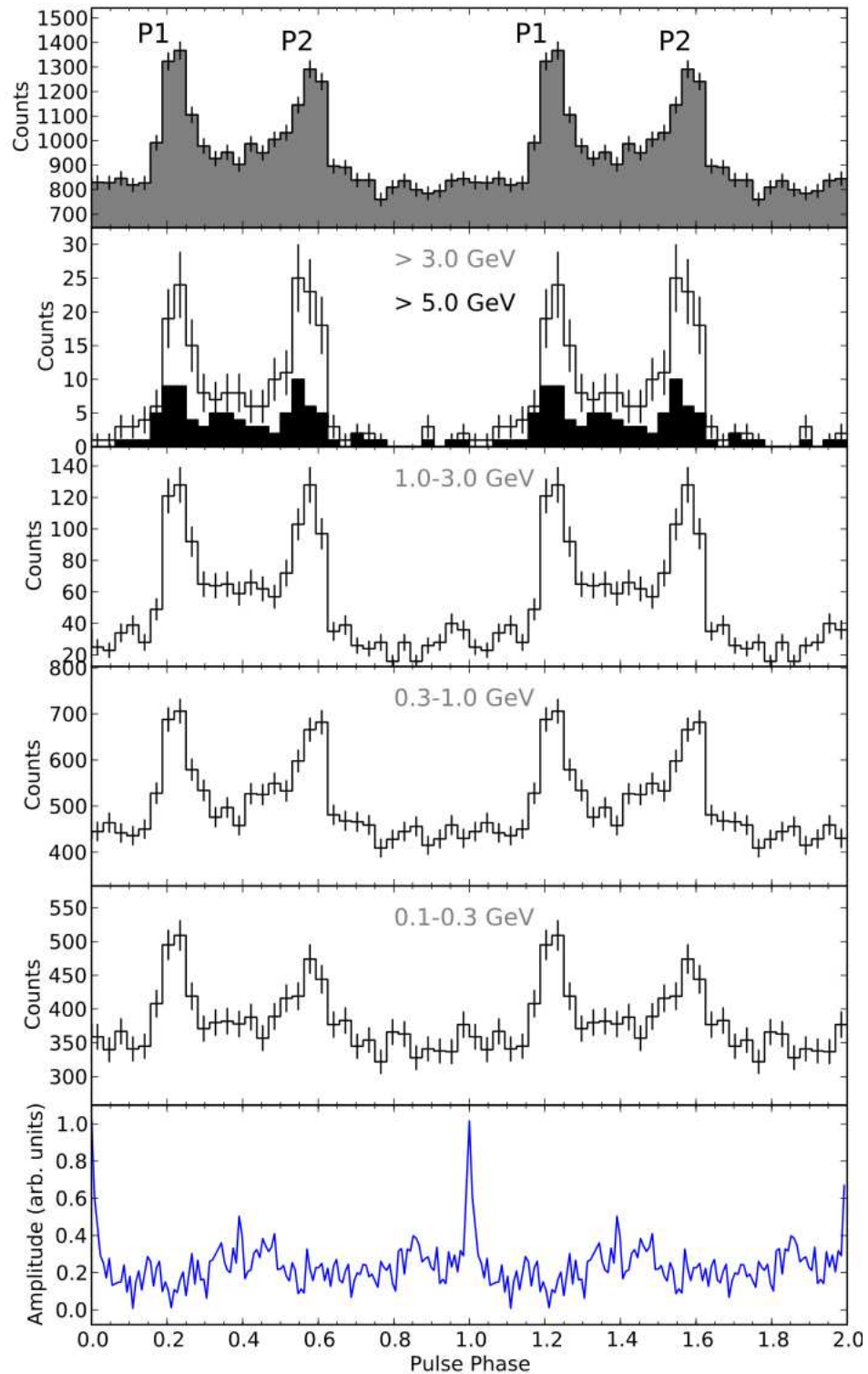


Figure 6.13: The folded light curves of PSR J1907+0602 taken from Abdo et al. (2010b). The top five are those made with the LAT data for different energy band, and the rest (bottom one) is the light curve of the Arecibo (radio) data.

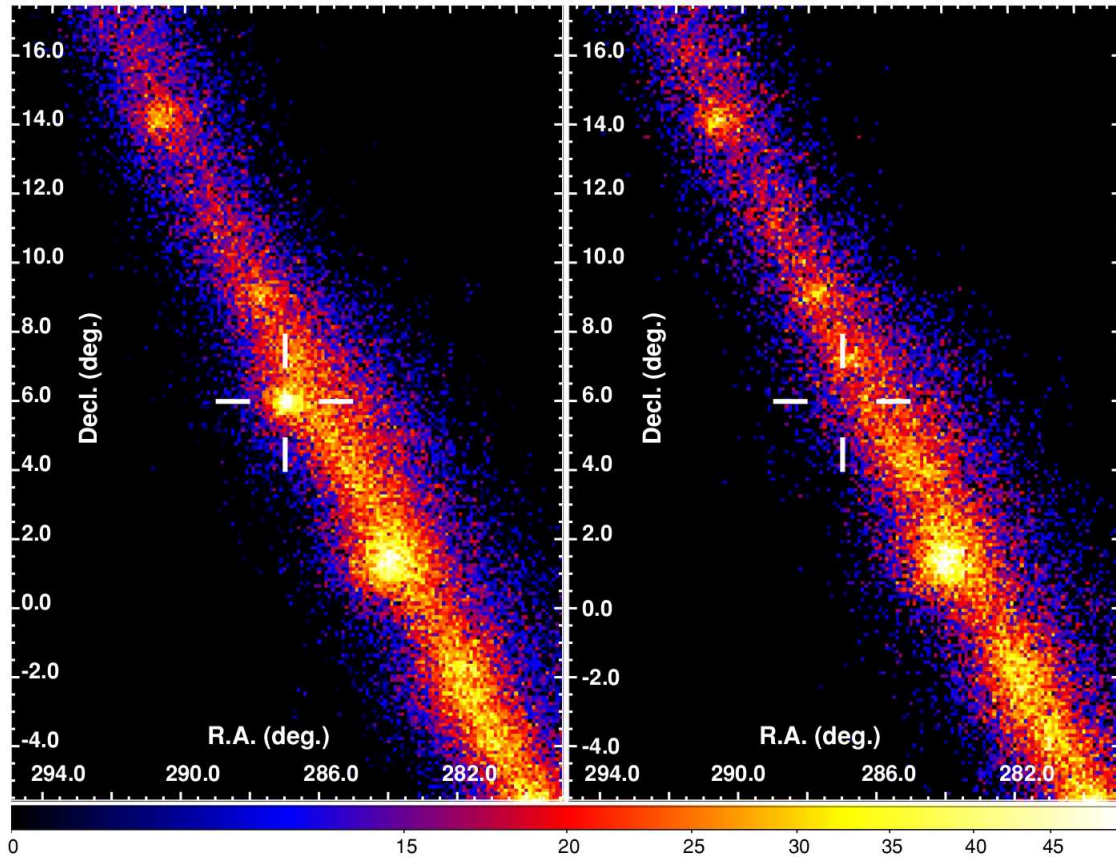


Figure 6.14: The Fermi-LAT counts map around PSR J1907+0602 taken from Abdo et al. (2010b). Left is the image at the “on” phase of PSR, and right is that at the “off” phase.

6.6 VERITAS analysis on the target

In this section, using the VERITAS observational data of MGRO J1908+06, we examine the spatial distribution of the gamma-rays at different energies.

6.6.1 Data used for the analysis

The total number of VERITAS runs that include MGRO J1908+06 in the useful field of view is 185, and the live time after the cleanup is 54 hours. We used 48 wobble runs targeted at an exotic gamma-ray object, SS433, with the wobble direction of north, because MGRO J1908+06 is in the northern vicinity of SS433 with a separation of about 1° . Table 6.3 shows the various runs used in this analysis, and Table 6.4 shows the zenith angle distributions of the files used for this analysis. It is primarily in the range of $25^\circ - 40^\circ$.

Kind of run	Year	# of runs
Wobble runs for MGRO J1908+06	09-10	5
Sky-Survey runs I originally used for SS433	07-08	28
SS433, wobbled to North	09-11	48
Sky-Survey runs and wobble runs for the HESS source	07-08	46
MGRO J1908/SS433 Straddle	11	4
MGRO J1908/SS433 Straddle	12	50
MGRO J1909+06 [Sic]	12	4
TOTAL	07-12	185

Table 6.3: VERITAS observations used for our analysis of MGRO J1908+06.

Zenith Angle	# of runs
25° – 30°	110
31° – 40°	58
41° – 50°	17
TOTAL	185

Table 6.4: Zenith angle distribution of the observing runs used for this analysis.

6.6.2 Significance and Excess calculation

We analyzed these data sets with the VEGAS version 2.3.0. The background rejection techniques of VEGAS are based on gamma-ray/cosmic ray selection, and this depends on the strength and the spectrum of the source. Table 6.5 shows the example of the selection criteria used for some of the Hillas parameters (See Sec. 3.2.2). These criteria were selected so that the detection sensitivity is maximized, based on a Monte-Carlo simulation for three different types of the source, soft, medium and hard. Cuts are applied to *Size* (total charge in all the pixels in the image, corresponding to the total light content), Mean Scaled *Width* (MSW: *Width* is the RMS spread of the light along the minor axis of the image ellipse on the telescope’s field of view. For Mean Scaled Parameters see Sec. 3.3.4.) and Mean Scaled *Length* (MSL: *Length* is the RMS spread of the light along the major axis of an image ellipse). We chose “Hard cuts for the analysis of MGRO J1908+06 because the source is detected at very high gamma-ray energies. We used the Ring Background Model (RBM) for the background estimation, but for the spectral analysis (Sec. 6.6.3) we used the wobble model, which is the current default of a spectral calculation (See Sec. 3.5, 3.6, and 3.7 for these models for background estimation).

Name	Source Spectrum	Size	MSW	MSL
Soft	6.6% Crab at 0.2 TeV, Index -4	> 200	< 1.15	< 1.3
Medium	2% Crab at 0.4 TeV, Index -2.4	> 400	< 1.15	< 1.3
Hard	2% Crab at 1 TeV, Index -2.0	> 1000	< 1.1	< 1.2

Table 6.5: Examples of cuts on the Hillas parameters, optimized for different types of the source. See Sec. 3.2.2 for the Hillas parameters, and see Sec. 3.3.4 for the Mean Scaled Parameters (MSPs). We chose “Hard” for the analysis of MGRO J1908+06.

6.6.2.1 Analysis 1

For VEGAS stage6 (See Sec. 3.5), the target position was set to the Milagro source position, RA=287.17° and Dec=6.18° ($l = 40^{\circ}24' \pm 6'_{stat} \pm 18'_{sys}$ and $b = -1^{\circ}0' \pm 6'_{stat} \pm 18'_{sys}$; Abdo et al., 2007; Aharonian et al., 2009). The search window (inside which “ON” events are counted) radius was set to 0.5°, following the HESS collaboration’s analysis of this source (Aharonian et al., 2009), and the source exclusion radius, the radius of the circle from which no background region is taken (See Fig. 3.8), was set to 0.7°. This region is called the “source exclusion region,” which in this case is centered on the Milagro source position. For the Ring Background Model (RBM) analysis, the inner radius of the background ring was = 0.7°, and the outer radius was = 0.9°. The analysis with these settings is called “Analysis 1” hereafter.

We found that the Significance at the source location was 8.5σ , and the maximum significance in the field of view was 10.7σ (See Table 6.7 and Fig. 6.15). The HESS team fitted 2D-Gaussians function to their excess map, and evaluated the source position and its error. The centroid of their best fit is RA=286.98° and Dec=6.27° ($l = 40^{\circ}23'9''.2 \pm 2'.4_{stat}$ and $b = -0^{\circ}47'10''.1 \pm 2'.4_{stat}$), and the extension is $\sigma_{src} = 0.34^{+0.04}_{-0.03}$ (Aharonian et al., 2009). Following the HESS team, we fitted our

excess map with 2D-Gaussian functions. For the fitting, we tried multiple ROOT macros, but as the primary tool we adopted “fit2DgaussDumm_acc.C,” which originally was developed for VEGAS by Jon Dumm of the University of Minnesota and revised by Brett McArthur of the Washington University in St. Louis. We fitted the map with a symmetrical 2D-Gaussian which has major and minor axes of equal length. We have some systematic errors when fitting due to the window size we choose. When its value is 1 (default), it means that the range of the fitting window is -1.0° to $+1.0^\circ$ from the target position, in RA and Dec (so the size is $2.0^\circ \times 2.0^\circ$ for this case).

VERTIAS has a finite angular resolution. By applying a 2D-Gaussian fitting to a map of a source such as Mrk421 (which is variable on time scales of minutes thus can be treated as a point source), we can measure the angular resolution of VERITAS. The $1-\sigma$ value of the 2D-Gaussian fitted for such a map is 0.063° . In case of an extended source, the reconstructed source image is the convolution of the true shape of the source and this PSF of VERITAS. Thus, the sigma of the source extension is calculated as $\sigma_{source} = \sqrt{\sigma_{fit}^2 - \sigma_{PSF}^2}$. We used this default value of $1-\sigma$ of the VERITAS PSF, 0.063° , for all the work described in this thesis.

We use what is called Uncorrelated Excess map for a 2D-Gaussian fitting. This is a kind of Excess map, but the ON counts are taken only in a single bin of the corresponding location of the map, unlike the normal (smoothed) Excess map where the ON counts are taken from a circle (search window, or integral window) with a certain radius centered on each locations. Because the background estimations is correlated with the bins in the vicinity, this map is not perfectly uncorrelated, but the excess counts (ON - background) is dominated by the ON counts, which are uncorrelated.

The variation of centroid and size with window size is not significant, so we

chose the result given when the fitting window size is $3.0^\circ \times 3.0^\circ$ for the source location: the centroid of the best-fitting Gaussian was RA= $286.96^\circ \pm 0.02$ and Dec= $6.23^\circ \pm 0.02$, which lies close to the Milagro positions and especially the HESS position. The extension was $\sigma_{src} = 0.42^\circ \pm 0.02$, which is a bit larger than the the HESS result. But we can say that our results are well consistent with that of the two groups at the source location.

Fitting Region (RA×Dec)	Gaussian Size (σ)	Centroid (RA, Dec)
$2.0^\circ \times 2.0^\circ$	0.45 ± 0.03	$(286.956^\circ \pm 0.019^\circ, 6.232^\circ \pm 0.020^\circ)$
$3.0^\circ \times 3.0^\circ$	0.42 ± 0.02	$(286.962^\circ \pm 0.018^\circ, 6.226^\circ \pm 0.020^\circ)$
$4.0^\circ \times 4.0^\circ$	0.41 ± 0.02	$(286.961^\circ \pm 0.018^\circ, 6.224^\circ \pm 0.020^\circ)$

Table 6.6: The results of the 2D-Gaussian fittings of the excess map of analysis 1. The fitting regions are the squares with different sizes centered on the Milagro source position.

	Source Location	Max. Sig. Location
RA	287.174°	287.049°
Dec	6.183°	6.108°
ON (Source) counts	4230	4366
OFF (Backgrounds) counts	4032	3828
Excess counts (See Sec. 3.7)	719.4	918.6
α (See Sec. 3.7)	0.871	0.901
Significance	8.5 σ	10.7 σ
Exposure	3240.8 min	

Table 6.7: The RBM analysis results for analysis 1 on MGRO J1908+063. The source position is set on the Milagro source position, and radius of the search window is set to = 0.5° as HESS to compare their Excess map with ours.

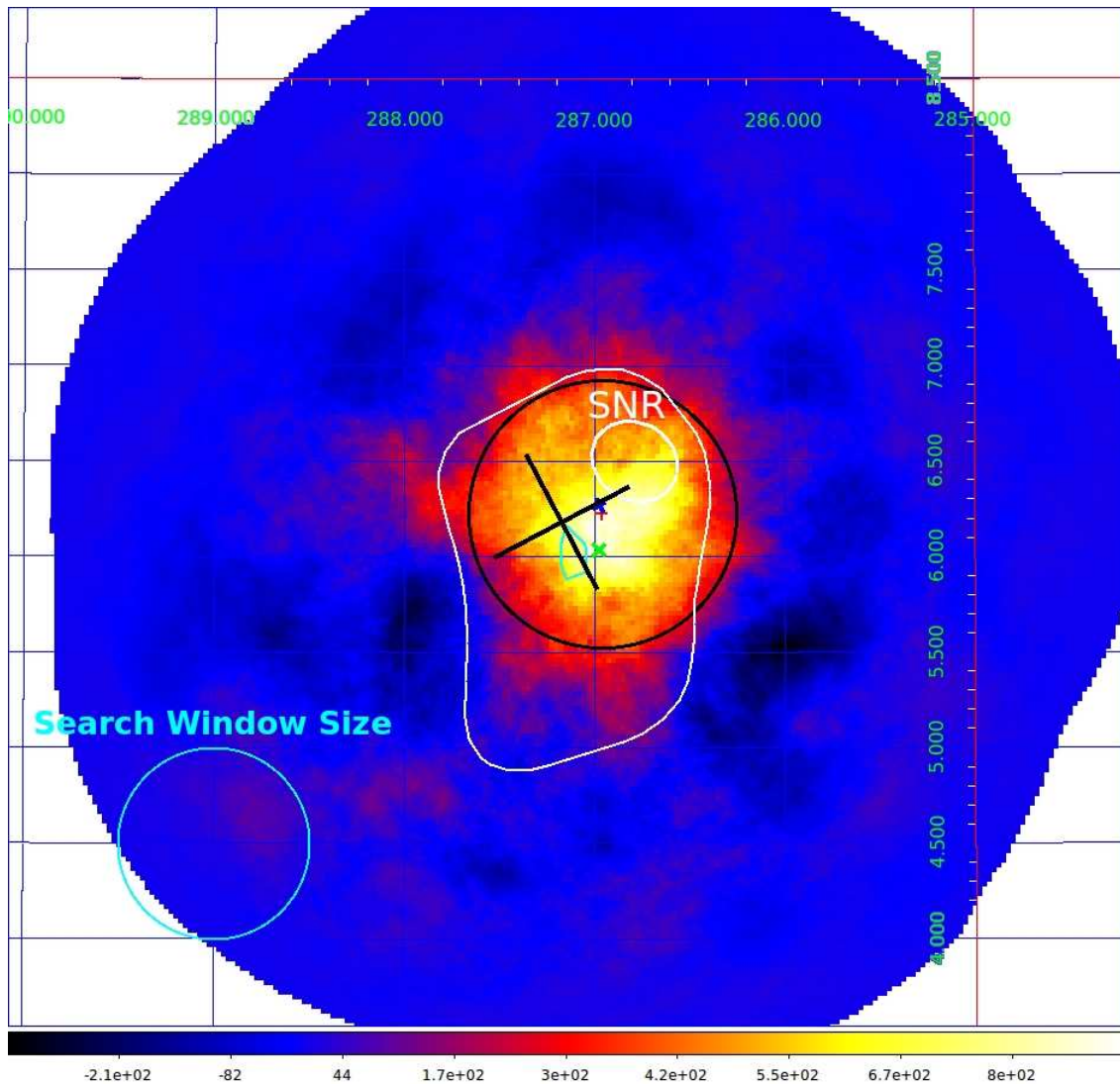


Figure 6.15: The RBM Excess map of MGRO J1908+06 of the search window radius of 0.5° , given as the result of analysis 1 (Sec. 6.6.2.1). The large black cross mark shows the Milagro source position and its error (simple summation of the statistical error and the systematic error.). The blue smaller cross is the HESS source position with the statistical error. The red cross is the centroid of the best fitting 2D-Gaussian function for the VERITAS Excess map given with the window size of $3.0^\circ \times 3.0^\circ$ (See Table 6.6). The white ellipse is SNR G40.5-0.5, and the green X is PSR J1907+0602. The contours near the center are the Milagro Significance contours of 8σ (inner, light-blue) and 5σ (outer, white). The black circle notes the region to be used as the “exclusion region” in analysis 2. It is centered on the best fitting 2D-Gaussian centroid (red cross) and has a radius of 0.7° .

6.6.2.2 Analysis 2

The problem with analysis 1 is that the Milagro source position is obviously displaced from the actual peak of the emission (See Fig. 6.15), and the source exclusion region does not satisfactorily cover the brightest region of the map. Thus, at some parts of the map the OFF region is contaminated by some source photons, which results in a lower significance. To avoid this, we set the source exclusion region to match the Gaussian centroid we adopted as the source location in analysis 1 (RA= 286.962° and Dec= 6.226° , while keeping the same radius of 0.7°). In VEGAS, we do this by loading a text file called the exclusionlist which contains the information on the centroid and the radius of the source exclusion circle at the stage 6. Moreover, we changed the size of the background ring, to be 0.75° for the inner radius and 1.00° for the outer radius. These changes increased the Significance and the Excess counts (See Table 6.8). We name this analysis as “Analysis 2”.

We then fitted the Excess map with 2D-Gaussians just as in analysis 1. Using a window size of $3.0^\circ \times 3.0^\circ$ we find a location of RA= $286.966^\circ \pm 0.017$ and Dec= $6.249^\circ \pm 0.019^\circ$. This location is totally within the error range of the HESS source location (See Fig. 6.16 and Fig. 6.17). The centroids for analysis 1 and analysis 2 are not identical, but close (compare the red cross at Fig. 6.15 and the red square right behind the blue cross in Fig. 6.16.), and the source exclusion region (the black circle near the center in Fig. 6.16 and in Fig. 6.17) evenly covers the high emission region, so we used this same source exclusion region for all our subsequent analysis.

	Source Location	Max. Sig. Location
RA	287.174°	286.973°
Dec	6.183°	6.208°
ON (Source) counts	4230	4366
OFF (Backgrounds) counts	4273	4894
Excess counts (See Sec. 3.7)	840.0	1007.0
α (See Sec. 3.7)	0.793	0.686
Significance	10.2 σ	12.5 σ
Exposure	3240.8 min	

Table 6.8: The RBM analysis results for analysis 2 on MGRO J1908+063. The source position is set on the Milagro source position, and radius of the search window is set to $= 0.5^\circ$ following HESS in order to be able to compare their Excess map with ours.

Fitting Region (RA×Dec)	Gaussian Size (σ)	Centroid (RA, Dec)
2.0° × 2.0°	0.48 ± 0.03	(286.961° ± 0.017°, 6.253° ± 0.019°)
3.0° × 3.0°	0.44 ± 0.02	(286.966° ± 0.017°, 6.249° ± 0.019°)
4.0° × 4.0°	0.43 ± 0.02	(286.966° ± 0.017°, 6.248° ± 0.019°)

Table 6.9: Results of 2D-Gaussian fitting of the excess map of analysis 2.

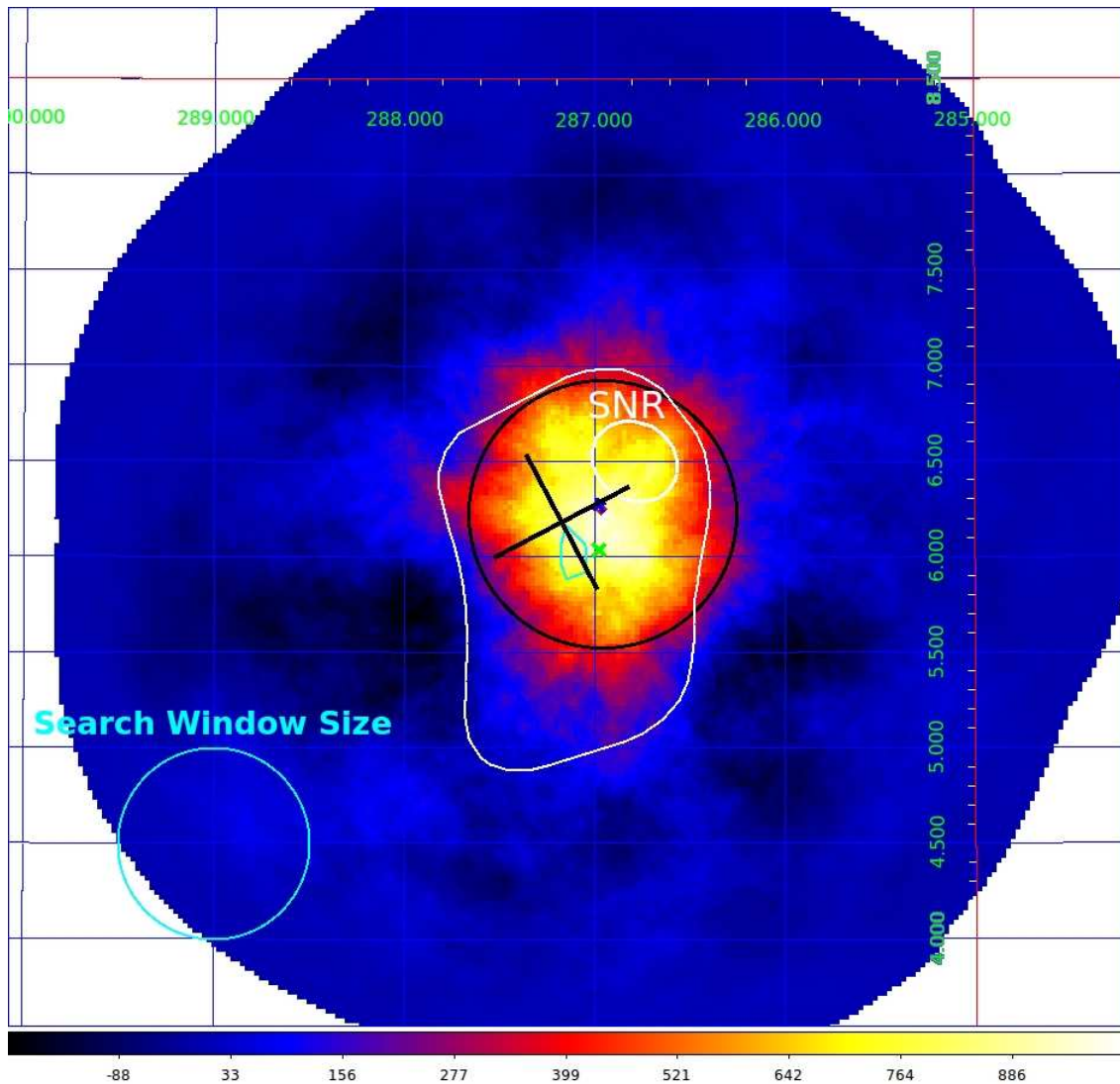


Figure 6.16: The RBM Excess map of MGRO J1908+06 using a search window radius of 0.5° , given as the result of analysis 2 (Sec. 6.6.2.2). The large black cross mark shows the Milagro source position and its error (simple summation of the statistical error and the systematic error.). The blue smaller cross is the HESS source position with the statistical error. The tiny red square behind the HESS cross (blue) is the centroid of the best fitting 2D-Gaussian function for this Excess map given at this analysis with the fitting window size of $3.0^\circ \times 3.0^\circ$ (See Table 6.9). The white ellipse is SNR G40.5-0.5, and the green X is PSR J1907+0602. The contours near the center are the Milagro Significance contours of 8σ (inner, light-blue) and 5σ (outer, white). The black circle is the source exclusion region.

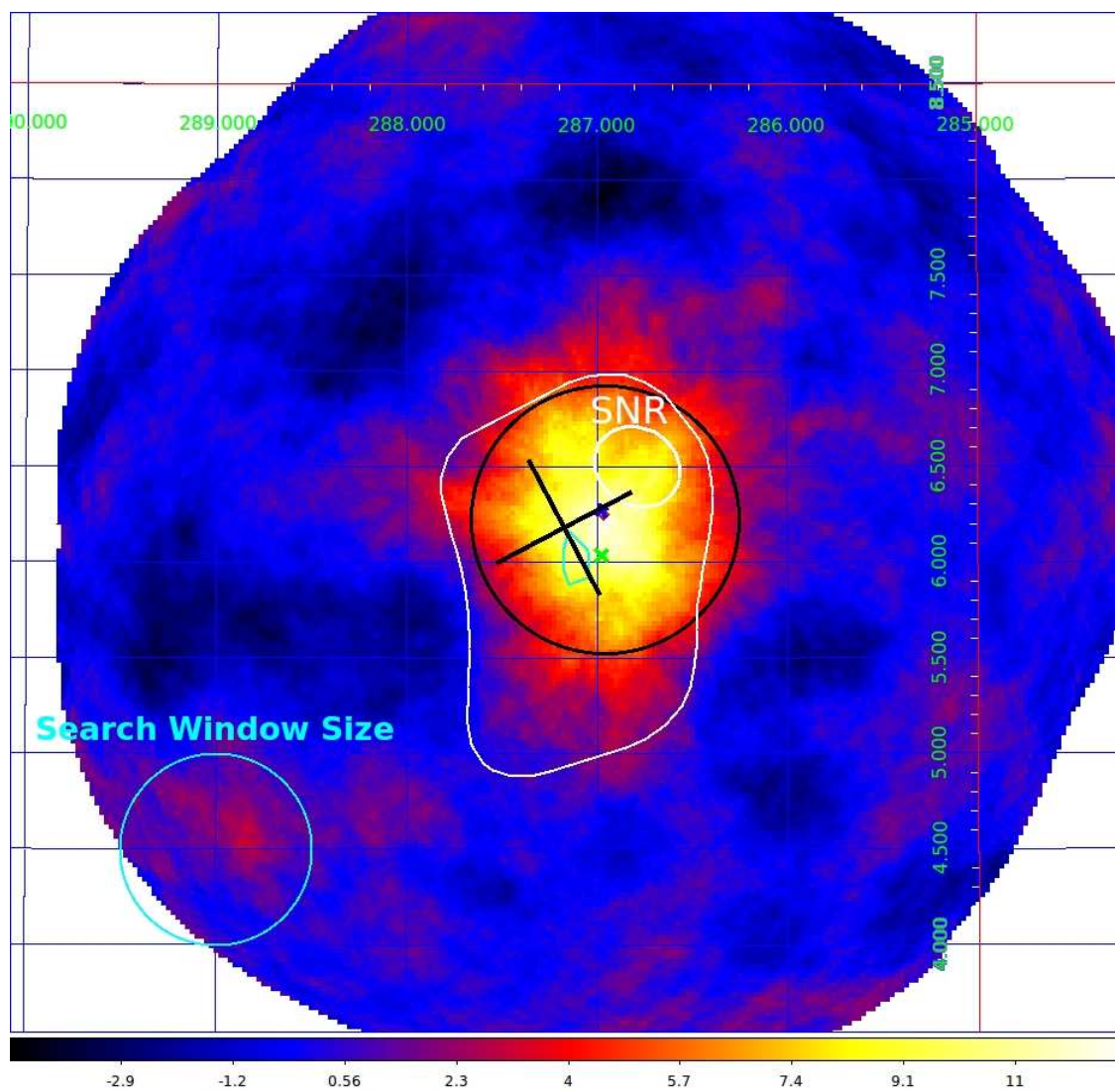


Figure 6.17: The RBM Significance map of MGRO J1908+06 corresponding to Fig. 6.16.

6.6.3 Energy Spectra of J1908 and Pulsar

We then calculated energy spectra for the source region and the pulsar region. As the position for the spectrum measurement of MGRO J1908+06, we used RA= 286.97° and Dec= 6.25°, the centroid of the best fitting 2D-Gaussian from analysis 2 (See Table 6.9), and an integration radius of 0.5° for the comparison with the HESS spectrum. This region (around MGRO J1908+06) is hereafter called “Region A.” The pulsar region, named “Region B,” is centered on the pulsar position (RA= 286.97° and Dec= 6.04°), and the integration radius was set to 0.4° to match the extension of the source at the lower energy (0.5-1.25 TeV: See Sec. 6.7.1).

For the spectral calculations, we need information on the effective area of the telescope array for different energies and zenith angles (See Sec. 3.8). Spectra are calculated at the stage 6 of VEGAS, and we need to specify what effective area lookup file is used at each of the analysis. The lookup files are sorted by the type of the source (hard, medium and soft), the season (Summer [May-Oct], Winter [Nov-Apr]) and the type of the telescope array (new, old), because the configuration of the telescope changed in Summer of 2009 (See 6.11). With the current version of VEGAS, the spectral calculation is carried out with the wobble model by default, not the RBM, and analyses with different effective area lookup tables must be run separately. Some runs have fields of view that do not cover the areas where their wobble background regions are located, so we removed such files from the run lists (See Table 6.11, 6.12 and 6.13). We specified the number of the energy bins of the spectra as 60 at stage 6. When three different analyses for MGRO J1908+06 position (See Table 6.12) and four for the pulsar position (See Table 6.13) were completed for each source, we combined the output spectra with the ROOT macro, “CombineMultipleStage6Results.C.” For this macro, we input the re-binning factor

for the energy bins, the number of the “fine bins” (the raw energy bins, the total number of which is 60 in this case) to be merged into one “coarse bin.” The energy threshold, the lowest energy of the energy bins with non-zero counts (the lowest energy level at which events can be reconstructed with accurate information on energy), was 0.47 TeV for both the two analyses (See Table 6.12 and 6.13). We increased this number from 1 until the error ranges of all the data points are above 0, so that the results represent detections. When this factor is 6, we have a data point at $E=20$ TeV, at which the flux data was taken by Milagro. So we adopted this re-binning factor for J1908. The PSR had good spectra also for larger re-binning factors of 4 and 5, but both of the normalization and the index did not vary much (the fractional error was less than $\sim 1.5\%$ for the norm and less than $\sim 1.5\%$ for the index), so we adopted a re-binning factor of 6 for the PSR also. The energy threshold, the lowest energy of the energy bins with non-zero counts (the lowest energy level at which events can be reconstructed with accurate information on energy), were 0.47 TeV for both of the two analyses (See Table 6.12 and 6.13).

Array	Season	Centroid (RA, Dec)
New	Summer	ea_Nov2010_na_ATM22_vegasv230_7sam_allOffsets_hard-1.root
Old	Summer	ea_Nov2010_oa_ATM22_vegasv230_7sam_allOffsets_hard-2.root
New	Winter	ea_Nov2010_na_ATM21_vegasv230_7sam_allOffsets_hard-1.root
Old	Winter	ea_Nov2010_oa_ATM21_vegasv230_7sam_allOffsets_hard-2.root

Table 6.10: Effective area lookup tables we used for the different epochs of observational data.

Fig. 6.18 and Fig. 6.19 show the spectra for the two regions. For the region A, the spectrum was $(\text{Norm}, \text{Index}) = ((4.4 \pm 0.6) \times 10^{-8} \text{ TeV}^{-1} \text{ m}^{-2} \text{ s}^{-1}, -1.79 \pm 0.11)$, and for the region B the spectrum was $(\text{Norm}, \text{Index}) = ((2.9 \pm 0.5) \times 10^{-8} \text{ TeV}^{-1}$

Array	Season	# of Files
New	Summer	109
Old	Summer	68
New	Winter	2
Old	Winter	6
Total		185

Table 6.11: The files used for the Significance and the Excess analysis sorted by the seasons and the type of the telescope array. Some of these were removed from the run lists for the spectral analyses in stage 6, because they did not have proper background regions in the field of view for the wobble model.

Array	Season	# of Files	Energy Threshold	Live Time
New	Summer	102	0.473 TeV	1802.2 min
Old	Summer	40	0.596 TeV	721.7 min
New	Winter	2	0.531 TeV	36.8 min
Old	Winter	0	N/A	N/A
Total		144	0.473 TeV	2560.8 min

Table 6.12: The numbers of the different files of the different types, used for the spectral analysis of MGRO J1908+06. All of these had background region inside the field of view for the wobble model. Energy Threshold is the energy of lowest energy bin where we have counts. The threshold of the combined spectrum for this analysis is the lowest one of these values, 0.473 TeV.

$\text{m}^{-2} \text{s}^{-1}$, -2.0 ± 0.1). The HESS spectrum around the centroid of their best fitting 2D-Gaussian with the integration radius of 0.5° was $(\text{Norm}, \text{Index}) = ((4.1 \pm 0.32_{stat} \pm 0.83_{sys}) \times 10^{-8} \text{ TeV}^{-1} \text{ m}^{-2} \text{ s}^{-1}, -2.1 \pm 0.07_{stat} \pm 0.2_{sys})$, which matches our region A spectrum within the error range. Fig. 6.20 shows the spectra from HESS and VERITAS. It also shows that the differential flux at 20 TeV that Milagro measured,

Array	Season	# of Files	Energy Threshold	Live Time
New	Summer	103	0.473 TeV	1810.9 min
Old	Summer	43	0.596 TeV	763.7 min
New	Winter	2	0.531 TeV	36.8 min
Old	Winter	3	1.06 TeV	54.3 min
Total		151	0.473 TeV	2665.8 min

Table 6.13: The numbers of the different files of the different types, used for the spectral analysis of PSR J1907+0602. All of these had background region inside the field of view for the wobble model. Energy Threshold is the energy of lowest energy bin where we have counts. The threshold of the combined spectrum for this analysis is the lowest one of these values, 0.473 TeV.

$(8.8 \pm 2.4) \times 10^{-11} \text{ TeV}^{-1} \text{ m}^{-2} \text{ s}^{-1}$, overlaps the VERITAS flux error range in the same energy, $(1.86 \pm 0.87) \times 10^{-10} \text{ TeV}^{-1} \text{ m}^{-2} \text{ s}^{-1}$. So we confirm that our spectral analysis results also match the HESS and Milagro results.

The energy spectrum for the region centered on the pulsar (region B) has a somewhat softer photon index. We investigate this in more detail in the next section.

From the spectral information we had now, we estimated the luminosities of J1908 (region A) and the pulsar (region B) with the assumption that they both are located at the distance of 3.2 kpc. We integrated the spectra between the energy range of the energy threshold (0.473 TeV) and the upper limit energy of the spectral calculations (30 TeV). The results were $2.15 \times 10^{33} \text{ erg/s}$ for region A and $1.05 \times 10^{33} \text{ erg/s}$ and for region B, respectively.

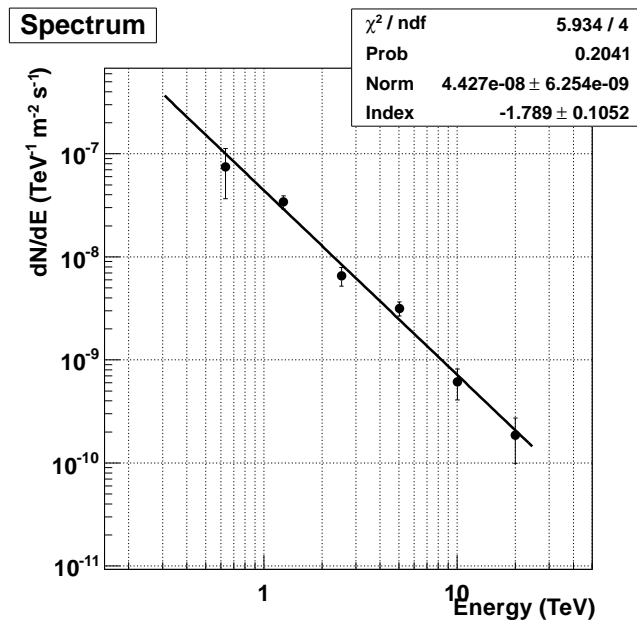


Figure 6.18: The spectrum of the “Region A,” the region around MGRO J1908+06 with 0.5° radius centered on the 2D-Gaussian centroid obtained at analysis 2 (RA= 286.97° and Dec= 6.20° ; See Sec. 6.6.2.2).

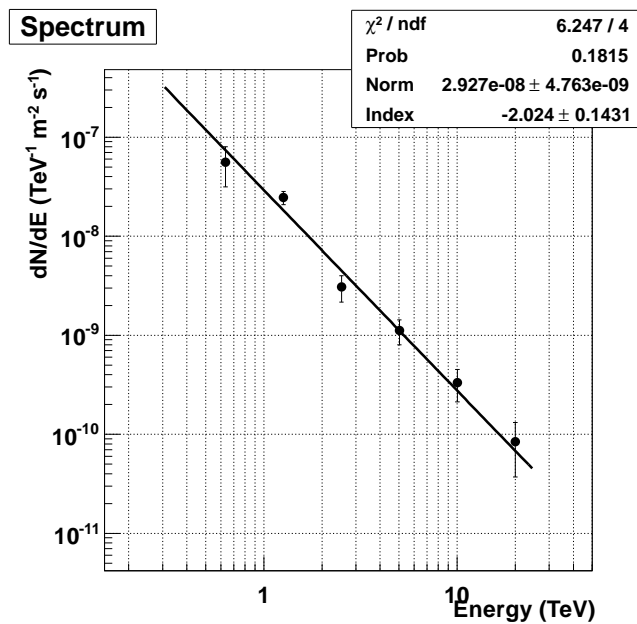


Figure 6.19: The spectrum of the “Region B,” region centered on PSR J1907+0602 (RA= 286.97° and Dec= 6.04°) with the window radius of 0.4° .

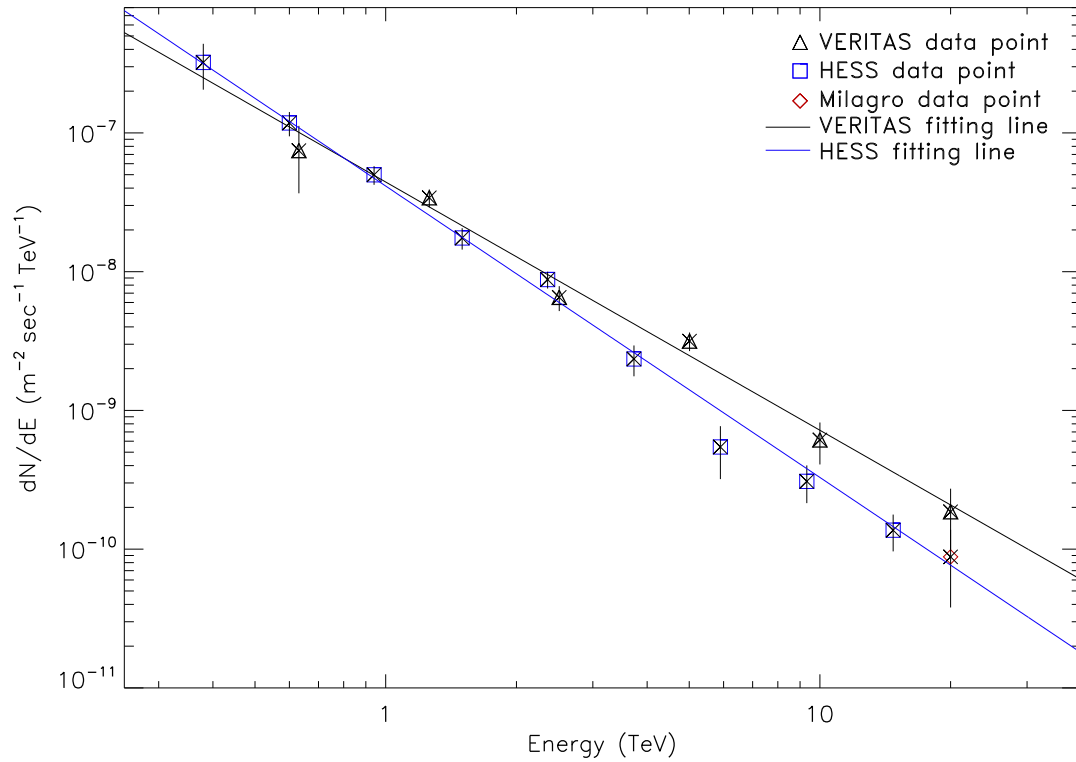


Figure 6.20: MGRO J1908+06 spectra from HESS (blue) and VERITAS (black). Our spectrum of J1908 is (Norm, Index) = $((4.4 \pm 0.6) \times 10^{-8} \text{ TeV}^{-1} \text{ m}^{-2} \text{ s}^{-1}, -1.79 \pm 0.11)$, and the HESS spectrum is (Norm, Index) = $((4.1 \pm 0.32_{stat} \pm 0.83_{sys}) \times 10^{-8} \text{ TeV}^{-1} \text{ m}^{-2} \text{ s}^{-1}, -2.1 \pm 0.07_{stat} \pm 0.2_{sys})$, so the two fitting lines match in the error range, and the Milagro data point (red: $(8.8 \pm 2.4) \times 10^{-11} \text{ TeV}^{-1} \text{ m}^{-2} \text{ s}^{-1}$) at 20 TeV is covered in the VERITAS error range ($(1.86 \pm 0.87) \times 10^{-10} \text{ TeV}^{-1} \text{ m}^{-2} \text{ s}^{-1}$) at that energy.

6.7 Energy dependent analysis

As noted in Sec. 6.3, MGRO J1908+06 is not a point source. Then, the issue of this study is the origin of the TeV emissions, namely whether they are from the pulsar or the SNR or possibly both of them. For this morphological study, we need to see the source with better spatial resolution, and it is useful to see it for different energy ranges. The angular resolution of VERITAS telescopes is $\sim 0.1^\circ$, but use of a search window radius of that size gives statistically unsatisfactory maps, so we choose 0.2° . Fig. 6.22 shows maps of MGRO J1908+06 in the energy bands 0.5-1.25 TeV, > 1.25 TeV and the full energy range. As we can see in the Table below, the maximum Significance in the Significance maps for these energy ranges are all high enough ($> 5\sigma$) that the structures are significant.

Energy Range	Maximum Significance
0.5-1.25 TeV	6.51σ
> 1.25 TeV	8.11σ
full energy range	8.71σ

Table 6.14: The maximum Significance in the energy dependent Significance maps taken with 0.2° integral window radius. The Max. Significance is above 5σ at all of these maps.

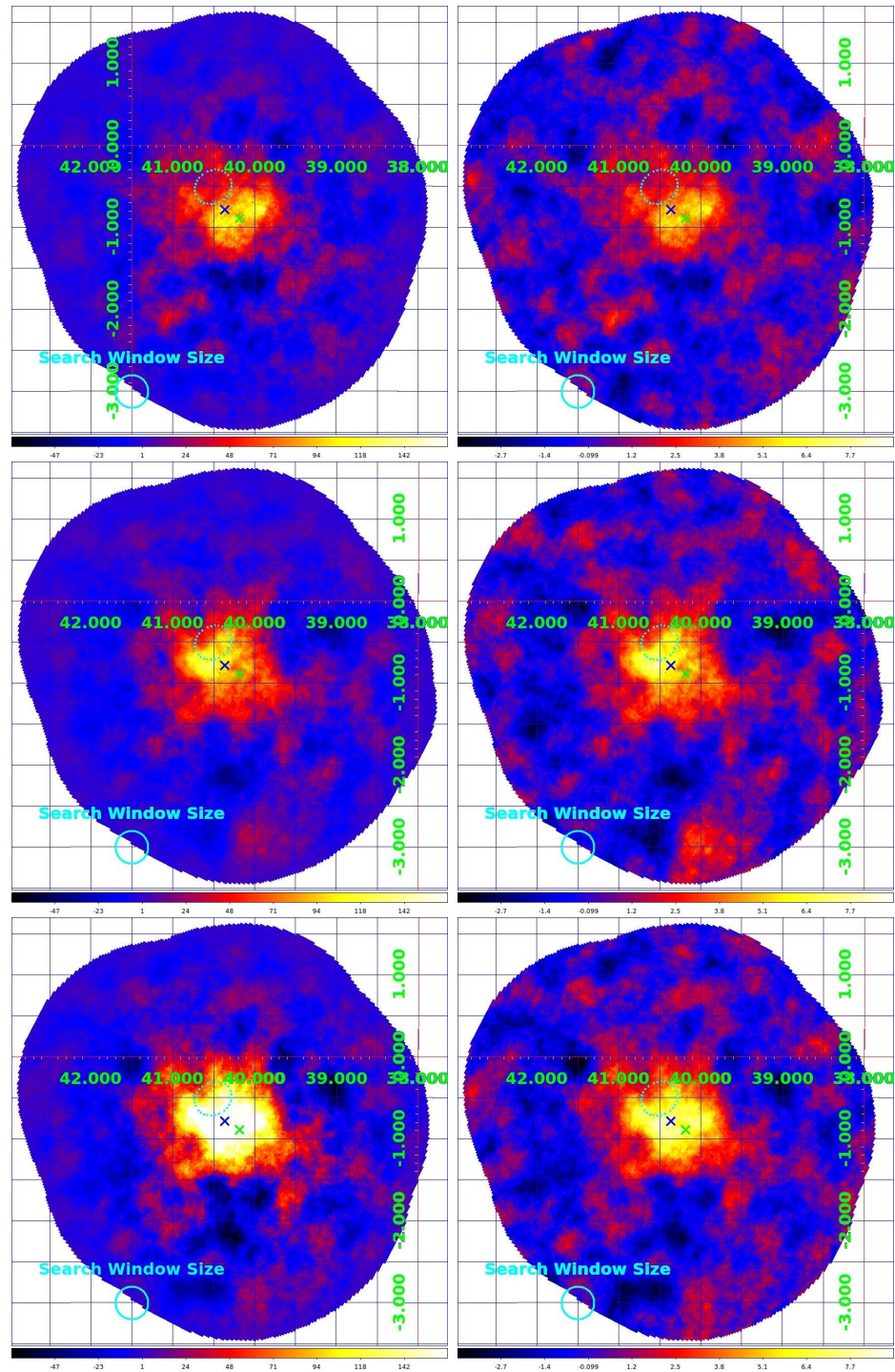


Figure 6.21: Excess (**Left**) and Significance (**Right**) maps of MGRO J1908+06 for the energy range of 0.5-1.25 TeV (first row), > 1.25 TeV (second row) and the full energy range (third row). The search window size is 0.2° . The blue X mark specifies our source position we had at analysis 2, the green cross is the position of PSR J1907+0602, and the ellipsis of the light blue line is SNR G40.5-0.5, respectively in each maps. The scale of Excess maps is -70 to 165, and the scale of Significance maps is -4 to 9.

6.7.1 2D-Gaussian fitting of the two maps

MGRO J1908+06 is an extended source, and may have an energy dependent structure. To investigate its nature, we created excess maps for three energy bands, 0.5-1.25 TeV, > 1.25 TeV and the full energy range, and fitted these with 2D-Gaussian functions, as we did in Sec. 6.6.2.

Fig. 6.23 shows the excess maps of the energy range of 0.5-1.25 TeV (**Left**) and > 1.25 TeV (**Right**) with the source position (blue X), the PSR J1907+0602 position (green cross), and our best fitting 2D-Gaussian circle (light blue circle, centered on the Gaussian's centroid and the radius set to the Gaussian's σ). The radius of the search windows, from which the ON counts are taken, was set to be 0.2° . The left side of this figure shows that the low energy emission (0.5-1.25 TeV) is concentrated on the small area around the pulsar. The centroid of the Gaussian is closer to the position of PSR J1907+0602, compared with the > 1.25 TeV map on the right side. On the other hand, the Gaussian centroid for the > 1.25 TeV map (**Right**) is close to the SNR, shifted away from the pulsar.

Also the extent of the emission is larger than than the low energy map, but are consistent within errors.

Table 6.15 shows the fitting results for the excess map of 0.2° window radius for the energy range of > 1.25 TeV. Because the fitting is centered on the target position of the analysis, when the fitting size is smaller than a certain value, the 2D-Gaussian might not fully cover the region of the highest significance, which might result in an inaccurate fitting. In this case, when the fitting range is $2.6^\circ \times 2.6^\circ$ or larger, the Gaussian size stays constant, and when the fitting range is $2.8^\circ \times 2.8^\circ$ or larger, the centroid position is almost constant. In case of the excess map for the energy range of < 1.25 TeV with the same of window radius (Table 6.16), for all the

fitting region sizes in the table, the Gaussian size stays almost constant but there is a tendency that the error is getting slightly smaller as the fitting region increases. The Centroid position is almost constant, when the fitting range is $2.2^\circ \times 2.2^\circ$ and larger. In case of the excess map for the energy range of < 1.25 TeV (Table 6.17), the centroid position is almost constant. The Gaussian size has some fluctuations with the window size smaller than $2.8^\circ \times 2.8^\circ$.

Fitting Region (RA×Dec)	Gaussian Size (σ)	Centroid (RA, Dec)
Fitting Region (RA×Dec)	Gaussian Size (σ)	Centroid (RA, Dec)
$2.0^\circ \times 2.0^\circ$	$0.42^\circ \pm 0.03^\circ$	$(286.965^\circ \pm 0.017^\circ, 6.231^\circ \pm 0.019^\circ)$
$2.2^\circ \times 2.2^\circ$	$0.44^\circ \pm 0.02^\circ$	$(286.968^\circ \pm 0.017^\circ, 6.239^\circ \pm 0.019^\circ)$
$2.4^\circ \times 2.4^\circ$	$0.45^\circ \pm 0.02^\circ$	$(286.966^\circ \pm 0.017^\circ, 6.243^\circ \pm 0.019^\circ)$
$2.6^\circ \times 2.6^\circ$	$0.43^\circ \pm 0.02^\circ$	$(286.966^\circ \pm 0.017^\circ, 6.248^\circ \pm 0.019^\circ)$
$2.8^\circ \times 2.8^\circ$	$0.43^\circ \pm 0.02^\circ$	$(286.966^\circ \pm 0.017^\circ, 6.247^\circ \pm 0.019^\circ)$
$3.0^\circ \times 3.0^\circ$	$0.43^\circ \pm 0.02^\circ$	$(286.966^\circ \pm 0.017^\circ, 6.246^\circ \pm 0.019^\circ)$
$3.2^\circ \times 3.2^\circ$	$0.43^\circ \pm 0.02^\circ$	$(286.966^\circ \pm 0.017^\circ, 6.246^\circ \pm 0.019^\circ)$
$3.4^\circ \times 3.4^\circ$	$0.43^\circ \pm 0.02^\circ$	$(286.966^\circ \pm 0.017^\circ, 6.245^\circ \pm 0.019^\circ)$
$3.6^\circ \times 3.6^\circ$	$0.43^\circ \pm 0.02^\circ$	$(286.966^\circ \pm 0.017^\circ, 6.245^\circ \pm 0.019^\circ)$
$3.8^\circ \times 3.8^\circ$	$0.43^\circ \pm 0.02^\circ$	$(286.966^\circ \pm 0.017^\circ, 6.245^\circ \pm 0.019^\circ)$
$4.0^\circ \times 4.0^\circ$	$0.43^\circ \pm 0.02^\circ$	$(286.966^\circ \pm 0.017^\circ, 6.245^\circ \pm 0.019^\circ)$

Table 6.15: The results of the 2D-Gaussian fittings the excess map of 0.2° window radius for the full energy range. The fitting regions are the squares with different sizes centered on the source position we had at analysis 2.

Fitting Region (RA×Dec)	Gaussian Size (σ)	Centroid (RA, Dec)
$2.0^\circ \times 2.0^\circ$	$0.40^\circ \pm 0.5^\circ$	$(286.934^\circ \pm 0.035^\circ, 6.168^\circ \pm 0.042^\circ)$
$2.2^\circ \times 2.2^\circ$	$0.40^\circ \pm 0.04^\circ$	$(286.941^\circ \pm 0.034^\circ, 6.173^\circ \pm 0.042^\circ)$
$2.4^\circ \times 2.4^\circ$	$0.40^\circ \pm 0.04^\circ$	$(286.940^\circ \pm 0.034^\circ, 6.176^\circ \pm 0.042^\circ)$
$2.6^\circ \times 2.6^\circ$	$0.38^\circ \pm 0.04^\circ$	$(286.941^\circ \pm 0.034^\circ, 6.168^\circ \pm 0.043^\circ)$
$2.8^\circ \times 2.8^\circ$	$0.40^\circ \pm 0.04^\circ$	$(286.940^\circ \pm 0.034^\circ, 6.176^\circ \pm 0.043^\circ)$
$3.0^\circ \times 3.0^\circ$	$0.40^\circ \pm 0.04^\circ$	$(286.940^\circ \pm 0.034^\circ, 6.177^\circ \pm 0.043^\circ)$
$3.2^\circ \times 3.2^\circ$	$0.40^\circ \pm 0.03^\circ$	$(286.940^\circ \pm 0.034^\circ, 6.177^\circ \pm 0.043^\circ)$
$3.4^\circ \times 3.4^\circ$	$0.39^\circ \pm 0.03^\circ$	$(286.941^\circ \pm 0.033^\circ, 6.173^\circ \pm 0.041^\circ)$
$3.6^\circ \times 3.6^\circ$	$0.39^\circ \pm 0.03^\circ$	$(286.941^\circ \pm 0.034^\circ, 6.174^\circ \pm 0.042^\circ)$
$3.8^\circ \times 3.8^\circ$	$0.40^\circ \pm 0.03^\circ$	$(286.941^\circ \pm 0.033^\circ, 6.174^\circ \pm 0.041^\circ)$
$4.0^\circ \times 4.0^\circ$	$0.40^\circ \pm 0.03^\circ$	$(286.940^\circ \pm 0.034^\circ, 6.176^\circ \pm 0.043^\circ)$

Table 6.16: The results of the 2D-Gaussian fittings the excess map of 0.2° window radius for 0.5-1.25 TeV. The fitting regions are the squares with different sizes centered on the source position we had at analysis 2.

Fitting Region (RA×Dec)	Gaussian Size (σ)	Centroid (RA, Dec)
$2.0^\circ \times 2.0^\circ$	$0.42^\circ \pm 0.04^\circ$	$(287.000^\circ \pm 0.033^\circ, 6.280^\circ \pm 0.034^\circ)$
$2.2^\circ \times 2.2^\circ$	$0.46^\circ \pm 0.05^\circ$	$(287.000^\circ \pm 0.033^\circ, 6.280^\circ \pm 0.035^\circ)$
$2.4^\circ \times 2.4^\circ$	$0.48^\circ \pm 0.05^\circ$	$(287.000^\circ \pm 0.032^\circ, 6.290^\circ \pm 0.033^\circ)$
$2.6^\circ \times 2.6^\circ$	$0.47^\circ \pm 0.04^\circ$	$(287.000^\circ \pm 0.032^\circ, 6.300^\circ \pm 0.035^\circ)$
$2.8^\circ \times 2.8^\circ$	$0.45^\circ \pm 0.04^\circ$	$(287.000^\circ \pm 0.033^\circ, 6.290^\circ \pm 0.035^\circ)$
$3.0^\circ \times 3.0^\circ$	$0.45^\circ \pm 0.04^\circ$	$(287.000^\circ \pm 0.033^\circ, 6.290^\circ \pm 0.035^\circ)$
$3.2^\circ \times 3.2^\circ$	$0.44^\circ \pm 0.03^\circ$	$(287.000^\circ \pm 0.033^\circ, 6.290^\circ \pm 0.034^\circ)$
$3.4^\circ \times 3.4^\circ$	$0.44^\circ \pm 0.03^\circ$	$(287.000^\circ \pm 0.033^\circ, 6.290^\circ \pm 0.033^\circ)$
$3.6^\circ \times 3.6^\circ$	$0.44^\circ \pm 0.03^\circ$	$(287.000^\circ \pm 0.033^\circ, 6.290^\circ \pm 0.034^\circ)$
$3.8^\circ \times 3.8^\circ$	$0.44^\circ \pm 0.03^\circ$	$(287.000^\circ \pm 0.033^\circ, 6.290^\circ \pm 0.034^\circ)$
$4.0^\circ \times 4.0^\circ$	$0.44^\circ \pm 0.03^\circ$	$(287.000^\circ \pm 0.032^\circ, 6.290^\circ \pm 0.034^\circ)$

Table 6.17: The results of the 2D-Gaussian fittings the excess map of 0.2° window radius for > 1.25 TeV. The fitting regions are the squares with different sizes centered on the source position we had at analysis 2.

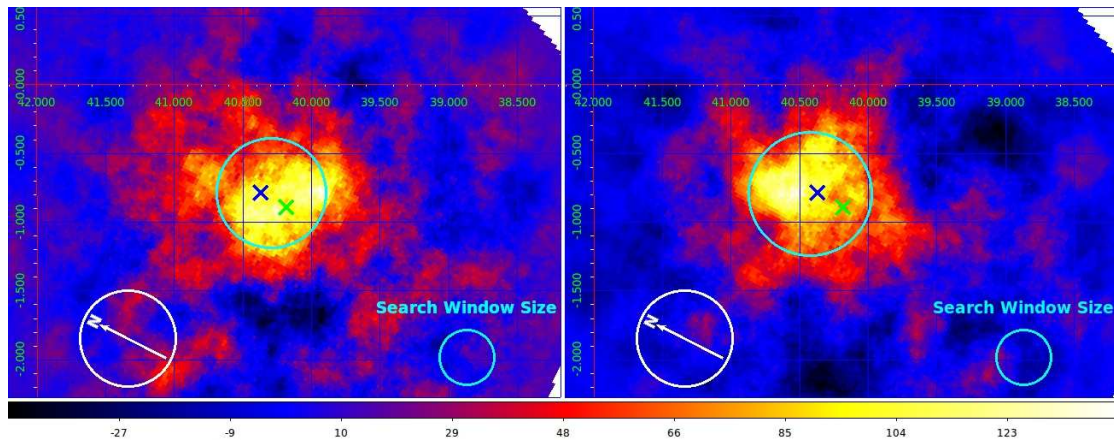


Figure 6.22: **(Left)** Excess map of MGRO J1908+06 for the energy range of 0-1.25 TeV. The blue X mark specifies our source position given at analysis 2, and the green cross is the position of PSR J1907+0602. The light blue circle is centered on the centroid of the best fitting 2D-Gaussian for this map, and its radius is equivalent to the σ value, 0.40° (the size of the fitting region is $3.0^\circ \times 3.0^\circ$). **(Right)** Excess map of MGRO J1908+06 for the energy range of > 1.25 TeV. The blue X mark specifies our source position given at analysis 2, and the green cross is the position of PSR J1907+0602. The light blue circle is centered on the centroid of the best fitting 2D-Gaussian for this map, and its radius is equivalent to the σ value, 0.45° (the size of the fitting region is $3.0^\circ \times 3.0^\circ$).

6.8 Discussion

MGRO J1908+06 is an extended TeV source that lies between the supernova remnant SNR G40.5-0.5 and the pulsar PSR J1907+06. What we are looking for is the mechanism of the TeV gamma-ray emission from J1908. It is possibly related to these objects in the vicinity, and the candidates for the origin of the emission are the SNR, the PWN, and the combination of these two objects.

6.8.1 Energy dependent morphology

As we have seen, MGRO J1908+06 is an extended source with some structures inside it. For a morphological study, we need to examine the source in different energy ranges. Fig. 6.24 is the two color Excess map of different energy ranges, 0.5-1.25TeV (red) and > 1.25 TeV (blue), and its integral window size is 0.2° .

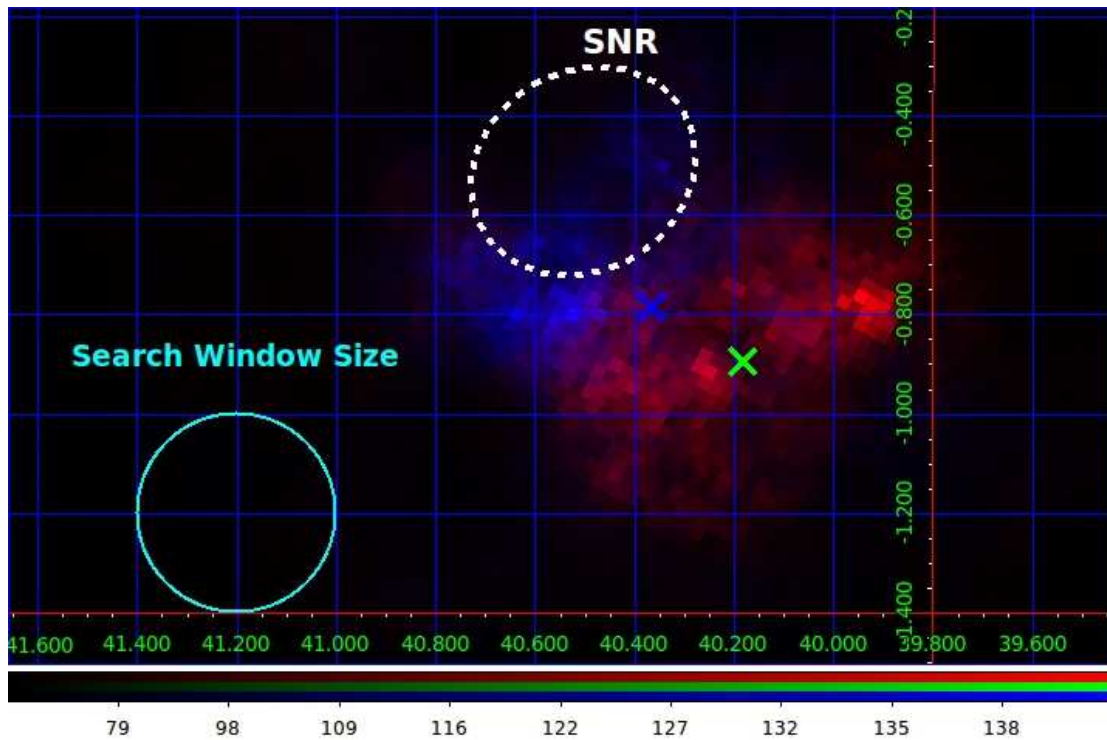


Figure 6.23: Two color VERITAS Excess map for the energy ranges of 0.5-1.25TeV (red), 1.25-3TeV (green), and > 3 TeV (blue). The search window radius is 0.2° . The blue cross near the center is the J1908 source position we found in analysis 2, and the green cross is the PSR.

From this map, we can see that the low energy emission (red: 0.5-1.25 TeV) is centered around the PSR and the high energy emission (blue: > 1.25 TeV) is on the rim of the SNR facing the side of the PSR.

6.8.2 Shock acceleration by SNR G40.5-0.5

SNR G40.5-0.5 is a supernova remnant where particles are still being accelerated at the shock front. So, this is a possible source of the TeV emission from MGRO J1908+06.

However, as we see at Fig. 6.24, only the emission of the high energy (> 1.25 TeV) is observed at the edge of the G40.5-0.5, and it is only on the side facing the PSR. Also, from Fig. 6.8, the radio continuum shows the strongest emission in G40.5-0.5 away from the part where TeV emission exists. Further, from Fig. 6.11, there is CO emission only at the edge of the TeV emission range, not covering the full TeV emitting region. These facts exclude the possibility that the TeV emissions from MGRO J1908+06 arises only from shock acceleration due to SNR G40.5-0.5.

6.8.3 Pulsar wind nebula

Fig. 6.25 plots Age vs Size of the currently known TeV PWNe, using the data from Kargaltsev & Pavlov (2010)¹. From this plot, a trend can be seen that as PWNe get older, their size increases, which matches our intuitive image of electrons diffusing into the ISM. We can exploit this trend to address the question of whether the TeV emission can be a PWN. On this plot, the dotted line specifies the log

¹Some PWNe in Table 1 of Kargaltsev & Pavlov (2010), #11, #28 and #33, were originally discovered in the HESS Galactic survey (Aharonian et al., 2006b). The names of these PWNe given by HESS are J1825-137, J1616-508 and J1804-216 respectively. Using the angular sizes (in σ) noted in the original HESS paper (Aharonian et al., 2006b), we estimated the sizes of these PWNe, using a formula, $\text{size} = 2 \times \sigma \times (180/\pi) \times \text{distance}$. The distances of each PWNe used for this calculation were from Kargaltsev & Pavlov (2010). Then, the two different sizes of the three PWNe above were: [Kargaltsev & Pavlov (2010), ours]=[60 pc, 31 pc], [70 pc, 22 pc] and [58 pc, 28 pc] respectively. For this study, we adopted the sizes we calculated here as the true value.

age of PSR J1907+0602, and one red error bar on it shows the range of the size of J1908 for the full energy range. This size was calculated by simply multiplying the distance to the PSR, 3.2 kpc, times the angular sizes in Table 6.15, $0.42^\circ \pm 0.03^\circ$ to $0.45^\circ \pm 0.02^\circ$, resulting in the allowed range 0.39° to 0.47° . The possible size of J1908 is thus calculated to be 43.6 pc to 52.5 pc. This range is above the cluster of the data points at the log age (yrs) of PSR J1907+0602, 4.28, but still close to it. So, this does not immediately exclude the possibility that MGRO J1908+06 is a PWN. Also, we did this for the energy range of 0.5-1.25 TeV. The angular sizes we chose from Table 6.16 are $0.38^\circ \pm 0.04^\circ$ and $0.40^\circ \pm 0.05^\circ$, which result in the allowed angular size range of 0.34° to 0.45° and the possible size of the emission range of 0.5-1.25 TeV is 38.0 pc to 50.3 pc. The blue error bar in the plot shows this, and a part of it is included in the data point cluster.

We note that no X-ray/radio counter part has been observed that corresponds to MGRO J1908+06. However, it is not uncommon that a PWN has only gamma-ray emission, and is not detected in other energy ranges. So this does not exclude the possibility that MGRO J1908+06 is a PWN.

6.8.3.1 Morphology of the emissions

HESS studied the energy dependent gamma-ray morphology of the PWN HESS J1825-137 (Aharonian et al., 2006a). They measured spectra at various distances from the pulsar PSR J1826-1334, which powers the PWN. They observed a softening of the energy spectrum at larger distances from the pulsar, or equivalently a decrease in source size with increasing energy of gamma-rays (See Fig. 6.26). This matches our physical intuition that higher energy particles should be found closer to the pulsar. The possible explanations they suggested are: (i) the electrons lose energy during propagation via loss mechanisms such as adiabatic expansion, ionization loss, bremsstrahlung, synchrotron radiation and inverse Compton scattering.

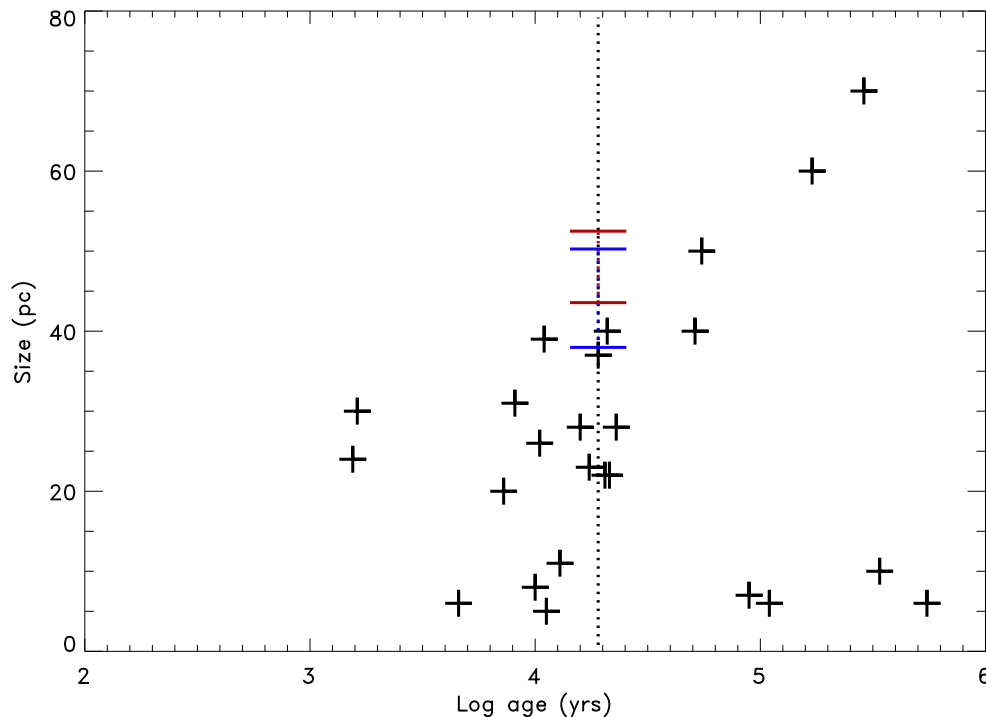


Figure 6.24: The relation between the sizes and the ages of some 40 TeV PWNe, using the data of Kargaltsev & Pavlov (2010). There is some correlation between these two parameters. The dotted line is the age of PSR J1907+0602 (Log age is 4.28). The red error bar specifies the size (σ) of the 2D-Gaussian functions fitted to the full energy map allowing for the systematic errors discussed in the text. The blue error bar is that for 0.5-1.25 TeV map.

(ii) Energy dependent speeds of diffusion or convection. (iii) The pulsar's injection spectrum varies with age, which, after propagation, results in a spatial variation of spectra (Aharonian et al., 2006a). So, how does MGRO J1908+06 compare?

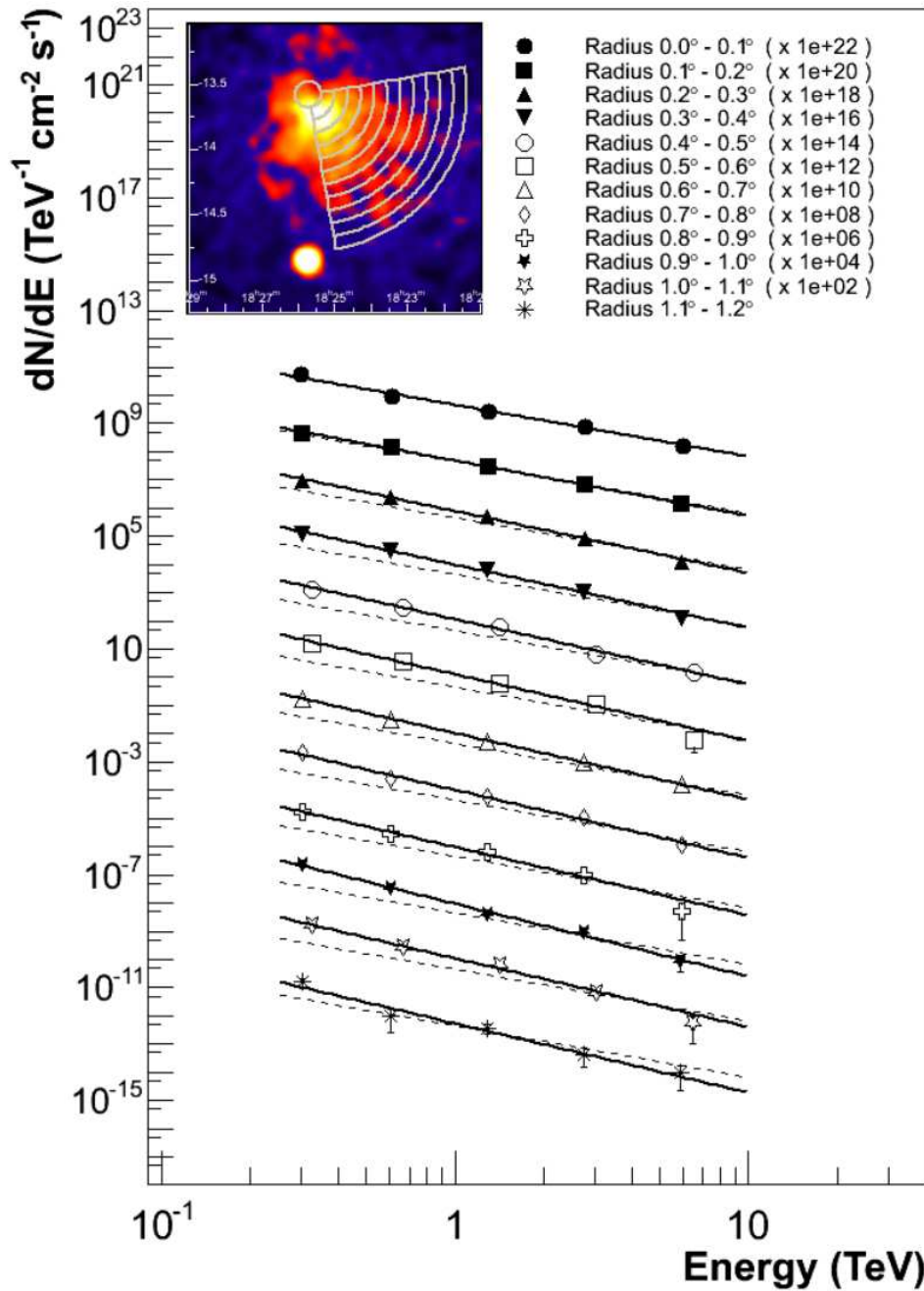


Figure 6.25: The energy spectra of the PWN HESS J1825-137 for different regions. The wedges in the upper left image are the radial regions with different distances in steps of 0.1° from the pulsar PSR J1826-1334. The broken lines are parallel (equal power law index) with the uppermost spectrum, that of the innermost (closest to the PSR) region. The softening of the spectrum occurs for regions more distant from the PSR. Taken from Aharonian et al. (2006a).

To see the morphology of the TeV emission, let's have a closer look at the energy dependent maps. The first row of Fig. 6.22 is the Excess and the Significance maps with the search window radius of 0.2° for the energy range of 0.5-1.25 TeV, the second row is maps for > 1.25 TeV, and the third row is the maps for the full energy range. In these maps, the red X marks the J1908 position that we had at analysis 2, and the blue X marks the position of PSR J1907+0602.

Comparing these images, the low energy emissions below 1.25 TeV is predominantly from the vicinity of the pulsar, while the emission of above 1.25 TeV most intensively occurs at the side of the SNR facing the PSR direction. Regarding this, it seems that the morphology of HESS J1825-137 we saw above does not apply to our case. Indeed, we observe roughly the opposite morphology: the lowest energy photons are concentrated near the pulsar.

Now there are two mechanisms for the high energy emission that we can suggest.

6.8.3.2 Model A: Shock Acceleration

One possible physical model for the TeV emission is the acceleration of particles at the shock front formed by high density gas and the pulsar wind. PSR J1907+0602 is an energetic pulsar, and so it must produce a pulsar wind. If this wind interacts with dense gas, particles in the wind could be re-accelerated via the Fermi acceleration mechanism (See Chap. 4). We have seen that there is CO gas near the region of the higher energy TeV (See Sec. 6.4), and the interaction of this gas and the pulsar wind can create a shock where Fermi acceleration occurs. The distance to the CO gas, 3.4 kpc (See Sec. 6.4), and the distance to the pulsar, 3.2 kpc (See Sec. 6.5), are compatible within the uncertainties, which complies with this model. The size of MGRO J1908+06 estimated in Sec. 6.8.3 is reasonable, or maybe a bit larger than the observed size range for PWN of the same age, but it is

still reasonable if we think that the re-acceleration of particles and the subsequent gamma ray emissions from them would result in an expanded PWN size.

We can test this model, for example, by looking for signs of interaction in molecular lines known to be produced by shocks (Hollenbach et al., 1989).

6.8.3.3 Model B: Moving pulsar

Another possible case is that the pulsar is moving and the high energy emission is caused by the old electrons emitted by the pulsar in its earlier phases. We assume that the pulsar was born in the supernova explosion. The pulsar loses its rotational energy by the spin-down as it gets older, so the electrons emitted earlier by the pulsar could be more energetic than the younger electrons, which are in the current vicinity of the pulsar. If the softening of the energy spectrum of freshly accelerated electrons due to spin-down of the pulsar is more rapid than the softening of the energy spectrum of old electrons due to radiative (or other) losses, then there would be higher energy TeV emissions closer to the SNR and lower energy emission closer to the pulsar, as observed. Fig. 6.7 shows the relation between the spectral index and the age of the observed PWNe, but it shows no clear correlation between these two parameters, so we cannot exclude this model immediately. Also, the PWN size is expected to be larger than the typical size due to the pulsar's high velocity, which matches our estimated PWN size.

The basic ideas for testing this model would primarily be measuring the proper motion of the pulsar. For SNR G40.5-0.5, we know when the supernova occurred and the separation between PSR J1907+0602 and SNR G40.5-0.5. By measuring the velocity of the pulsar, we would be able to know if the PSR was born in the supernova, the remnant of which is SNR G40.5-0.5. This velocity measurement can be accomplished by simply measuring the position of the PSR some years later via

radio imaging or pulse timing.

6.9 Conclusion

We analyzed the unidentified galactic TeV gamma-ray source MGRO J1908+06 with the VERITAS data which amounts to 54 hours in length. The calculated position and spectrum were compatible with the past analytical results of Milagro and HESS. Our energy dependent analysis revealed that the low energy emission in the energy range 0.5-1.25 TeV is concentrated around the pulsar PSR J1907+0602, and the medium energy emission in the energy range of > 1.25 TeV is mainly on the side of the supernova remnant SNR G40.5-0.5, facing toward MGRO J1908+06. Comparison with CO, HI, and continuous radio maps excluded the SNR as the solo origin of the emission. One possibility is that the TeV emission originates from the shock formed by the pulsar wind from PSR J1907+0602 and SNR G40.5-0.5, and the other possibility is that the TeV emissions are from the old electrons emitted by the PSR J1907+0602 in its earlier phases with higher rotational energy. These models can be tested by future observations.

CHAPTER 7 CONCLUSION

VERITAS compliments the coverage provided by spaced-based instruments such as the Fermi-LAT (30 MeV-300 GeV) with its large effective area at higher energy (100 GeV-50 TeV). With this strength, VERITAS can contribute to revealing the physical nature of astronomical objects and study the particle acceleration mechanisms within them.

The first topic of my thesis was the nova explosion in a symbiotic binary star system, V407 Cygni, that occurred in March 2012. Fermi-LAT detected gamma-rays from this event in the 0.1-10 GeV energy range and measured their spectrum. At the nova shock, particles are accelerated via the Fermi acceleration mechanism. The likely origin of the gamma-ray emission is these accelerated charged particles, either protons (hadronic model) or electrons (leptonic model). The Fermi-LAT team modeled the particle energy spectra with cutoff power law models. The cutoff energy for the leptonic model is sufficiently low that no TeV emission is predicted. In contrast, the hadronic model can produce significant TeV emission depending on the model parameters. No TeV emission was detected with VERITAS. The TeV flux upper limit was used to place constraints on the maximum energy of particles accelerated in the nova shock and the high energy extension of the particle spectra.

The V407 Cygni observations were taken at large zenith angles (LZA). Most targets are observed with VERITAS near the zenith, where the performance is better, so the analysis procedures for LZA observations are less well developed. Also making use of LZA observations of the Crab nebula, two different event reconstruction methods for VERITAS were compared: the standard method and the “displacement method”. The latter gives better sensitivity when the zenith angle is large.

The main subject of my thesis is the unknown galactic TeV gamma-ray source MGRO J1908+06, whose discovery was reported by Milagro in 2007. HESS later showed that one of their new TeV sources, HESS J1908+063, is identical to this Milagro source. A total of 54 hours of VERITAS data on this target were analyzed. The VERITAS data show a source position and spectrum consistent with those from Milagro and HESS. The source is located between the supernova remnant SNR G40.5-0.5 and the pulsar PSR J1907+0602. The separation of these two objects (on the sky) is 28 pc. The TeV emission likely originates from either the SNR, the PWN, or a combination of the two.

Energy dependent maps were created for a morphological study. The emission in different energy ranges is different spatially. Low energy (<1.25 TeV) emission is concentrated around the pulsar PSR J1907+0602. The high energy (>1.25 TeV) emission is strongest at the edge of the SNR on the side towards the PSR.

An origin of the TeV emission as solely due to shock acceleration in the SNR is ruled out by the facts that the radio continuum emission is strongest emission on the side of the SNR away from the pulsar and CO emission is seen only at the edges of the TeV emitting region. The properties of the TeV emission are generally consistent with those of PWN, although the spatial extent of the emission is somewhat larger than other PWN of similar age. However, our intuitive understanding suggests that the spectra of PWN should soften with increasing distance from the parent pulsar, as is observed for the PWN HESS J1825-137. The morphology of MGRO J1908+06 contradicts this. Two possible interpretations were proposed to explain the morphological results. One is that the pulsar wind is colliding with dense gas, seen in CO, at the edge of the SNR. Shocks created by the collision could then accelerate particles at the shock front creating the observed harder emission near the SNR. This can be tested by seeing whether there is a shock at that location,

which can be done by searching for molecular emission lines produced by shocks. The other model is a moving pulsar: if the pulsar was born at the center of SNR G40.5-0.5 then it is moving with high velocity. The pulsar spins down with age, thus, particles accelerated in the young pulsar wind may be more energetic than those currently being accelerated. So the higher energy emission near the SNR may be due to relic electrons. This hypothesis can be tested by measuring the pulsar velocity via high resolution pulsar position measurements.

Bibliography

- Abdo, A. A., et al. 2007, *ApJ*, 664:L91-L94
- Abdo, A. A., et al. 2009, *Science*, 325, 840
- Abdo, A. A., et al. 2010, *Science*, 329, 817
- Abdo, A. A., et al. 2010, *ApJ*, 711, 64
- Acciari, V. A., et al. (VERITAS Collaboration), 2008, *ApJ*, 679, 1427
- Aharonian, F., et al. 2006, *A&A*, 460, 365
- Aharonian, F., et al. 2006, *ApJ*, 636, 777
- Aharonian, F., et al. 2009, *A&A*, 499, 723
- Allen, C. W., 1976, *Astrophysical Quantities*, Athlone Press, London
- Axford, W. I., Leer, E., & Skadron, G. 1978, in *Proc. of 15th mt. Cosmic Ray Conf.*,
Plovd iv 11, p. 132
- Bassani, L. et al. 2010, *ATel.* #2498
- Bassani, L. et al. 2010, *ATel.* #2506
- Bell, A. R. 1978, *Mon. Not. R. Astron. Soc.* 182, 147
- Berge, D., Funk, S., Hinton, J. 2007, *A&A*, 466, 1219 230/111/)
- Blandford, R. D. & Ostriker, J. P. 1978, *ApJ*, 221, L29
- Bode, M. F. & Kahn, F. D. 1985, *Mon. Not. R. astr. Soc.*, 217, 205-215

- Çelik, Ö. 2008, “Observations of Crab Nebula and Pulsar with VERITAS.” PhD dis., University of California, Los Angeles
- Chaty, S. 2010, arxiv:1005.0100
- Cheung, C. C. et al. 2010, *ATel.* #2487
- Clark, D. H., Caswell, J. L. 1976, *Monthly Notices Roy. Astron. Soc.*, 174, 267
- Cogan, P. 2006, “Nanosecond Sampling of Atmospheric Cherenkov Radiation Applied to TeV Gamma-Ray Observations of Blazars with VERITAS.” PhD diss., University College Dublin
- Cogan, P., et al., 2007, *Proc. the 30th International Cosmic Ray Conference*, Merida, Mexico [arXiv:0709.4233]
- Cogan, P. 2008, *ICRC Proceedings*, 3, 1385.
- Daum, A. et al. 1997, *ApJ*, 8, 1
- Downes, A. J. B., Salter, C. J., & Pauls, T. 1980, *A&A*, 92, 47
- Domingo-Santamaría, E. et al. 2005, *ICRC Proceedings*, 5, 363-366
- Eichler, D. & Beskin, G. 2001, arXiv: astro-ph/0111081
- Fermi, E. 1949, *Phys. Rev.* 75, 11691174
- Fomin, V. P., et al., 1994, *Astropart. Phys.*, 2, 137
- Fuchs, Y., Miramond, L. K. & Ábráham, P., 2006, *A&A*, 445, 1041
- Gall, D. D. 2010, “Multi-Wavelength Studies of VHE Gamma-Ray Blazars.” PhD diss., Purdue University
- Gould, R. J. & Schröder, G. P. 1966, *Phys. Rev. Letters* 16, 252

- Guen ette, R. 2010, "VERITAS observations of galactic compact objects" PhD diss., McGill University
- Hays, E. A., & Fermi LAT Collaboration 2010, *Bulletin of the American Astronomical Society*, 41, 670
- Helene, O. 1983 *Nucl. Instr. and Meth.* 212, 319
- Helene, O. 1990 *Nucl. Instr. and Meth.* 300, 132
- Hewish, A., Bell, S. J., Pilkington, J. D. H., Scott, P. F. and Collins, R. A. 1968 *Nature* 217, 709
- Hillas, A. M. 1985 *19th Int. Cosmic Ray Conf., La Jolla* 3, 445
- Hillas, A. M. 1996 *Space Science Rev* 75, 17
- Hofmann, W. et al. 1999, *Astropart. Phys.* 122, 135-143
- Hoffmeister, C. 1949, *Ver off. Sternw. Sonneberg.* 1, 295
- Holder, J. et al. (VERITAS collaboration) 2006, *Astropart. Phys.*, 25, 361
- Holder, J. et al. (VERITAS collaboration) 2008, *Proc. of 4th Int. Meeting on High Energy Gamma-Ray Astronomy*, 657
- Hollenbach, D. J., Chernoff, D. J. & Mckee, C. F. Aharonian, F. A. 1989, *In ESA, Infrared Spectroscopy in Astronomy* p. 245-258
- Horns, D. & Aharonian, F. A. 2010, arXiv:astro-ph/0407119
- Kargaltsev, O., Pavlov, G. 2010, arXiv:astro-ph/1002.0885
- Kamae, T., Karlsson, N., Mizuno, T., Abe, T. & Koi, T. 2006, *ApJ*, 647, 692
- Kertzman, M., Sembroski, G. M. 1994 *Nucl. Instr. and Meth.* 343, 629

- Kieda, D. B. 2011, *ICRC Proceedings*, 0343
- Kifune, T. 2004, *Uchuū Kō Enerugi Ryūshi no Butsurigaku* (Physics of High Energy Astroparticles), Tokyo, Japan: Baifukan
- Knapp, G. R., Morris, M. 1985 *ApJ*, 707, 1168
- Koyama, K. et al. 1995, *Nature*, 378, 255
- Krymsky, G. F. 1977, *Dokl. Akad. Nauk SSSR*, 234, 1306.
- Kubota, K. et al. 2010, *ApJ* 709 1374
- Landau, L. D., Lifshitz, E. M. 1987, *Fluid Mechanics, Second Edition: Volume 6* (*Course of Theoretical Physics*), Oxford, UK: Pergamon Press
- Lessard, R. W. et al. 2001, *Astropart. Phys.* 15, 1
- Longair, M. S. 1992, *High Energy Astrophysics: Volume 1, Particles, Photons and their Detection (Second Edition)*, Cambridge, Cambridge, UK: Cambridge University Press
- Longair, M. S. 1992, *High Energy Astrophysics: Volume 2, Stars, the Galaxy and the interstellar medium (Second Edition)*, Cambridge, Cambridge, UK: Cambridge University Press
- Longair, M. S. 2011, *High Energy Astrophysics (Third Edition)*, Cambridge, Cambridge, UK: Cambridge University Press
- Li, T.-P., Ma, Y.-Q. 1983, *ApJ*, 272, L317
- Meinunger, L. 1966, V407 Cygni. *Mitt. Veranderl. Sterne.* 87, 111
- Melia, F. 2009, *High-Energy Astrophysics (Princeton Series in Astrophysics)*, Princeton, NJ: Princeton University Press

- Mayer, M., Brucker, J., Jung, I., Valerius, K. & Stegmann, C., 2012, arXiv:1202.1455v2
- Morang, M. 2008, talk “Shower Reconstruction Algorithms for the VERITAS Gamma Ray Telescopes” given at the *3rd Annual Conference for Undergraduate Women in Physics*
- Munari, U., Margoni, R. & Stagni, R. 1990, *Mon. Not. R. Astron. Soc.* (1990) 242, 653-659
- Munari, U. et al. 2010, *Mon. Not. R. Astron. Soc.* (2010) 000, 17
- Nagai, T. et al. (VERITAS collaboration) 2007, In *Proc. of the 30th International Cosmic Ray Conf.* Merida, Mexico
- Nishiyama, K. & Kabashima, K. 2010, *International Astronomical Union Central Bureau for Astronomical Telegrams*, reported by H. Maehara, no. 2199
- Ñunez, P. D. et al. 2011, *ApJ*, 731, 105
- Orlando, S. & Drake, J. J. 2011, *Mon. Not. R. Astron. Soc.* 000, 1-10
- Osaki, Y. 1996, *Uchū Kagaku Nyūmon* (Introduction to the Space Science), Tokyo, Japan: The University of Tokyo Press
- Pauliny-Toth, I. J. & Kellermann, K. I. 1966, *ApJ*, 146, 634
- Reynolds, P. T., et al. 2005, *ApJ*, 404, 206
- Rolke, W. A., Lopez, A. M., & Conrad, J. 2005, *Nuclear Instruments and Methods in Physics Research A*, 551, 493
- Sabatini, S., et al. 2010, *ApJ* 712, L10

- Shore, S. N., Wahlgren, G. M., Augusteijn, T., Liimets, T., Page, K. L., Osborne, J. P., Beardmore, A. P., Koubsky, P., Slechta, M., Votruba, V. 2011, *Astron. Astrophys.*, 527, A98+
- Sokoloski, J. L., et al. 2006, *Nature* 442, 276
- Stil, J. M., Taylor, A. R., Dickey, J. M., Kavars, D. W., Martin, P. G., Rothwell, T. A., Boothroyd, A. I., Lockman, F. J., McClure-Griffiths, N. M. 2006, *AJ*, 132, 1158 astro-ph/0605422
- Takahara, F. 2002, *Tentai Kō Enerugi Genshou* (Astro High Energy Phenomena), Tokyo, Japan: Iwanami Shoten
- Tanaka, S. J., Takahara, F. 2010, *ApJ* 715, 1248-1257
- Tavani, M., Mukherjee, R., et al. 1997, *ApJ* 479, L109
- Vandenbrouke, J., et al. 2010, *ApJ*, 718, L166
- Ward, J. E. 2008, *High Energy Gamma-Ray Astronomy* (AIP Conf. Proc. 1085), ed. F. A. Aharonian, W. Hofmann, F. Rieger (Melville, NY:AIP), 301
- Weekes, T. C. 2003, *Very High Energy Gamma-ray Astronomy (Series in Astronomy Astrophysics)*, Philadelphia, PA: Institute of Physics Publishing
- Yang, J., Zhang, J., Cai, Z. et al. 2006, *Chin. J. Astron. Astrophys.* Vol. 6, No. 2, 210-216